Photoacoustic imaging beyond the acoustic diffraction limit

Sergey Vilov

Communauté UNIVERSITÉ Grenoble Alpes

THÈSE

Pour obtenir le grade de

DOCTEUR DE LA COMMUNAUTÉ UNIVERSITÉ GRENOBLE ALPES

Spécialité : PHYSIQUE APPLIQUEE

Arrêté ministériel : 25 mai 2016

Présentée par

SERGEY VILOV

Thèse dirigée par **Emmanuel BOSSY**, UGA

préparée au sein du **Laboratoire Interdisciplinaire de Physique (LiPhy)**
dans **l'École Doctorale de Physique**

Imagerie photoacoustique au-delà de la limite de diffraction acoustique

Thèse soutenue publiquement le **1 octobre 2019**, devant le jury composé de :

Monsieur Olivier Couture
Directeur de Recherche au CNRS, Institut Langevin, Paris,
Examinateur, Président du jury

Monsieur Ben Cox
Professeur, University College London, London,
Rapporteur

Monsieur Eric Lacot
Professeur des Universités, LiPhy, Université Grenoble - Alpes,
Examinateur

Madame Anne Sentenac
Directrice de Recherche au CNRS, Institut Fresnel, Marseille,
Rapportrice

ABSTRACT

Wave imaging remained diffraction-limited for centuries, until methods, such as PALM, STORM and STED were proposed in optics. Thanks to such methods, imaging with a resolution much better than the wavelength became possible. Inspired by these super-resolution methods, the present PhD study is focused on beating the diffraction limit in acoustic-resolution photoacoustics. In the frames of this study, super-resolution is demonstrated experimentally in vitro with such techniques as super-localisation, fluctuation-based analysis and model-based reconstruction. For each method, the resolution limit is identified, strong and weak points are analysed, prospects are discussed. In addition, super-resolution by sparsity-based reconstruction is demonstrated in relation to sparse-array imaging. At the end, all studied super-resolution methods are compared. An extra chapter is devoted to overcoming visibility problems in photoacoustic imaging by means of fluctuation analysis.

Keywords: *Photoacoustics*, *Super-resolution*, *Diffraction limit*, *Localization*, *Sparsity*, *Sparse array*, *Visibility*.

REMERCIEMENTS

Tout d'abord je tiens à remercier mon directeur de thèse, Emmanuel Bossy, de m'avoir confié un projet très intéressant et de m'avoir guidé soigneusement pendant les trois années de ma thèse. Je lui suis très reconnaissant d'avoir toujours été a l'écoute, d'avoir toujours eu la volonté de discuter avec moi quel que soit le moment. Je remercie aussi Bastien Arnal de m'avoir mis le pied à l'étrier au début de ma thèse et de m'avoir beaucoup aidé dans la suite. Sans son aide, sa patience et son soutien les résultats présentés dans cette thèse seraient bien plus modestes.

Je remercie les membres du jury M. Olivier Couture, M. Ben Cox, M. Eric Lacot et Mme. Anne Sentenac d'avoir examiné soigneusement ma thèse et d'avoir pu venir à la soutenance. Certes, les questions suivant la présentation constituent le moment le plus stressant de la soutenance mais dans mon cas c'était un grand plaisir de répondre aux question bien pensées, donnant des pistes pour de futures recherches. Je remercie vivement les rapporteurs Ben Cox et Anne Sentenac d'avoir préparé leurs rapports très détaillés.

Pendant la thèse on vit des périodes difficiles soit parce qu'une piste explorée depuis longtemps a amené nulle part soit parce qu'il pleut trop en novembre. Pour traverser de telles périodes il est important de ne pas rester emmêlé dans ses pensées. Les thésards perdus ont besoin d'être écoutés et réconfortés pour recouvrer la confiance en soi. Cela dit, je remercie ma mère Larisa, mon ami Nikita et surtout ma fiancée Natasha de leur soutien infini qui m'a toujours donné la force de persévérer.

Outre E. Bossy et B. Arnal, je remercie les autres membres de l'équipe: Antonio Caravaca, Guillaume Godefroy, Sylvain Mezil, Sylvie Costrele, Philippe Moreau, Irène Wang et Bathilde Rivière de tout le temps qu'on a passé ensemble, de toutes nos sorties et de toutes nos discussions qui animaient la pause café. L'ambiance dans notre bureau me donnait une raison supplémentaire pour venir le matin au travail et cette ambiance va certainement me manquer.

Enfin, et ce n'est pas le moins important, je remercie tous les personnels du Laboratoire Interdisciplinaire de Physique qui m'ont donné un coup de main à un moment ou l'autre. Les conseils de Philippe Marmottant, Danièle Centanni, Mehdi Inglebert, Sylvain Losserand et Olivier Stephan m'ont permis d'avancer plus rapidement et d'avoir des résultats publiables dès la première année de ma thèse.

TABLE OF CONTENTS

ABSTRACT i

ACKNOWLEDGEMENT ii

1 Introduction **1**

1.1 Optical imaging and its limitations 1

1.2 Principles of conventional optical imaging 1

1.2.1 Optical imaging beyond the diffraction limit 5

1.2.2 Optical imaging in the scattering regime 5

1.3 Photoacoustic imaging 6

1.3.1 Introduction 6

1.3.2 Photoacoustic generation 7

1.3.3 Principles of acoustic-resolution photoacoustic imaging 9

1.3.4 Linear array imaging 12

1.4 State-of-the-art and objectives of this thesis 15

2 Experimental equipment, materials and methods **19**

2.1 Experimental setup 19

2.2 Light source 20

2.3 Ultrasound electronics 21

2.4 Synchronization 24

2.5 Ultrasound probes 25

2.6 Microfluidic circuits 30

3 Localization-based super-resolution imaging **32**

3.1 Principles of localization-based super-resolution imaging 32

3.1.1 Localization-based super-resolution in optics 32

3.1.2 Localization-based super-resolution in ultrasound imaging 33

3.1.3 Motivation for localization-based photoacoustic imaging 34
3.2 From photoacoustic RF signals to localization images 35
3.2.1 Localization in the RF-space vs localization in the BF-space . . . 35
3.2.2 Choice of the localization method in the BF-space 38
3.2.3 Expected localization precision 38
3.3 Experimental demonstration 39
3.3.1 Samples 39
3.3.2 Measurement protocol 41
3.3.3 Typical RF signals from a single bead 42
3.4 Results 43
3.5 Conclusion 45

4 Super-resolution photoacoustic imaging based on flow-induced fluctuations 48
4.1 Principle of fluctuation-based super-resolution imaging 48
4.1.1 Super-resolution optical fluctuation imaging (SOFI) 48
4.1.2 Fluctuation-based photoacoustic imaging 49
4.1.3 The proposed approach based on flow-induced fluctuations 50
4.2 Materials and methods 52
4.2.1 Samples 52
4.2.2 Measurement protocol 53
4.2.3 Signal processing 53
4.3 Results 55
4.3.1 Bead samples 55
4.3.2 Blood samples 59
4.4 Conclusion 62

5 Super-resolution by model-based reconstruction 64
5.1 Introduction 64
5.2 Model-based reconstruction approach 65
5.2.1 Forward measurement model 65
5.2.2 Ill-posed linear inverse problems 65
5.2.3 Regularization-based solution 66

5.3 Photoacoustic forward model 68
5.3.1 Physical model 68
5.3.2 Discretization of the problem 69
5.3.3 Construction of the RF-space propagation matrix $\boldsymbol{A}_{RF}$ 70
5.3.4 Construction of the BF-space propagation matrix $\boldsymbol{A}_{BF}$ 71
5.3.5 Resolution and ill-posedness of the reconstruction problem 72
5.4 State-of-the-art and objectives of this chapter 73
5.5 A proof-of-principle experiment 75
5.5.1 Materials and methods 75
5.6 Two-channel case to further investigate the resolution limit 82
5.6.1 Simulations of RF data : method 82
5.6.2 Single shot/mean image 83
5.6.3 Fluctuation-based+model-based imaging 86
5.6.4 Some insights into performance and mechanism of model-based reconstruction 89
5.6.5 Mechanism and performance of sparsity-based reconstruction . . . 90
5.6.6 Influence of the non-negativity constraint 95
5.6.7 Reliability 97
5.6.8 Positivity-based reconstruction 97
5.7 Conclusion 99

6 Photoacoustic and ultrasound imaging with a sparse array 101
6.1 Introduction 101
6.1.1 2D imaging vs 3D imaging 101
6.1.2 State-of-the-art 102
6.1.3 Objectives of this chapter 102
6.2 Experimental demonstration 103
6.2.1 Materials and methods 103
6.2.2 Results 105
6.3 Theoretical investigation 107
6.3.1 Simulation methods 108
6.3.2 Results 108
6.4 Conclusion 110

7 Flow-based visibility enhancement in photoacoustic imaging 112
7.1 Introduction . . . 112
7.1.1 Origin of visibility problems in photoacoustic imaging . . . 112
7.1.2 State-of-the-art . . . 113
7.1.3 Principles of the proposed approach . . . 114
7.2 Proof-of-principle experimental demonstration . . . 114
7.2.1 Materials and methods . . . 114
7.2.2 Results . . . 116
7.3 Theoretical analysis . . . 119
7.3.1 Theoretical model . . . 119
7.3.2 Validation in numerical simulations . . . 120
7.4 Conclusion . . . 125

8 Conclusion 126
8.1 Main results . . . 126
8.2 Discussion and perspectives . . . 128
REFERENCES . . . 130
LIST OF PUBLICATIONS . . . 139

Appendices

Appendix A Delay-and-sum beamforming 141

Appendix B Remarks on the numerical norm-based reconstruction 145

Appendix C Singular value decomposition filtering 148

CHAPTER 1

Introduction

1.1 Optical imaging and its limitations

1.2 Principles of conventional optical imaging

Optical imaging includes a number of techniques that use light to obtain images from inside the body, tissues or cells. Optical images can provide structural information about the object or information about particular properties, such as chemical composition or absorption. Optical instruments are widely used to magnify and resolve objects that are too small to be seen with the bare eye.

One of the simplest optical instruments that serve to magnify small objects is a 4f microscope. A schematic of such a microscope is shown in Fig. 1.1. The microscope consists of two converging lenses: the objective lens with focal length f_1 and the tube lens with focal length f_2. The distance between the lenses is equal to the sum $f_1 + f_2$. The imaged object is placed at the distance f_1 from the objective lens whereas the camera is placed at the distance f_2 from the tube lens. When light propagates from the object to the camera, a magnified image is formed on the camera.

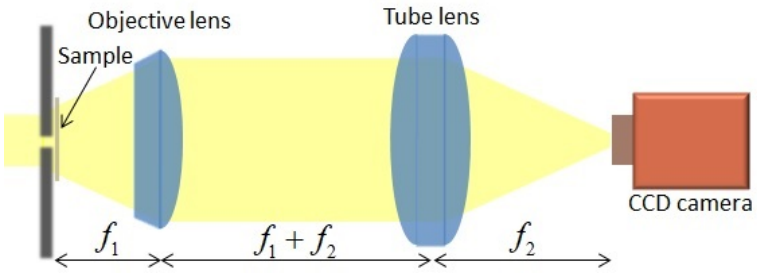

Fig. 1.1 Simplest optical microscope. When the object to the left of the objective re-emits light, a magnified image appears on the camera to the right of the tube lens.

The ability to distinguish different parts of the imaged object is characterized by the resolution of the imaging system. In most conventional applications, imaging is made possible by focusing light. In the optical microscope shown in Fig. 1.1 the entire object is illuminated and focusing is achieved in reception. Some other optical instruments exploit focusing in transmission or in both transmission and reception of light.

For instance, focusing in transmission is used in scanning fluorescence microscopy [Lichtman and Conchello, 2005]. This technique relies on fluorophore molecules that emit light at a specific visible wavelength when exposed to light at a different wavelength. When fluorophores are bound to the structure of interest, this structure can be imaged with high contrast as the photons originating from the fluorophores can be easily separated from those coming from the background. As excitation of fluorophores requires high energies, wide illumination can not be used and focusing in transmission is preferred.

Another example of focusing in transmission is provided by optical-resolution photoacoustic imaging (OR-PAI). This kind of photoacoustic (PA) imaging is based on detection of acoustic waves resulting from absorption of light focused in a chosen region of the object [Wang and Hu, 2012; Beard, 2011; Yao and Wang, 2013]. Thanks to light focusing, objects features comparable to the optical wavelength can be resolved in OR-PAI.

Confocal microscopy [Pawley, 2010] exploits focusing in transmission as well as in reception. Confocal microscopes reconstruct 3D objects by capturing multiple 2D images at different depths and at each depth the photons that do not originate from the selected slice of the object are discarded. This is achieved by placing a pinhole in the objective confocal plane in front of the detector. As a result, only light produced by fluorophores very close to the imaged plane can be detected, leading to an improved resolution, especially in the sample depth direction.

Whatever focusing technique is used, the in-plane (lateral) resolution of any conventional imaging system is restrained by diffraction effects, usually conditioned by the finite aperture and finite bandwidth of the system. Due to diffraction, a single point source results in a finite-size spot on the observation plane. This spot is called the point spread function (PSF) of the imaging system. For instance, imaging a point source with a system having a circular aperture (for example, the microscope shown in Fig. 1.1) produces the PSF shown in Fig. 1.2. The central bright region of this PSF is called the Airy disc.

It should be emphasized that in optical microscopy one usually considers *intensity* images while in acoustic/photoacoustic microscopy *amplitude* images are usually used. So, in this PhD study, we will always consider *amplitude* images.

The resolution of an imaging system can be characterized by the full width at half maximum (FWHM) of the PSF (Fig. 1.2b). In this PhD study we shall consider different sources resolvable if they are separated by more than a FWHM of the PSF. Fig. 1.3 provides examples of completely resolved sources, sources separated by a FWHM of the PSF and unresolved sources.

In conventional optical microscopy resolution is limited by diffraction only in the

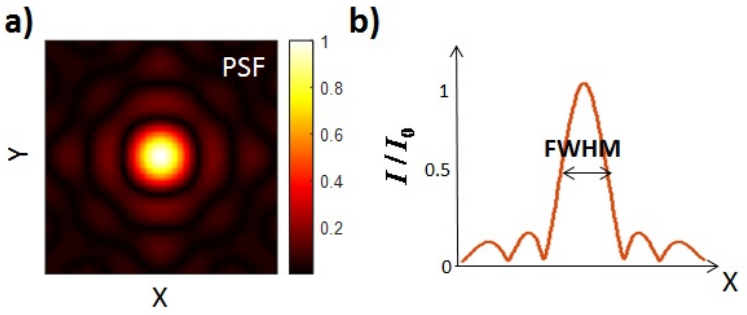

Fig. 1.2 (a) PSF of an imaging system with a circular aperture. The colormap corresponds to the normalized intensity I/I_0. (b) Lateral profile of the PSF shown in (a).

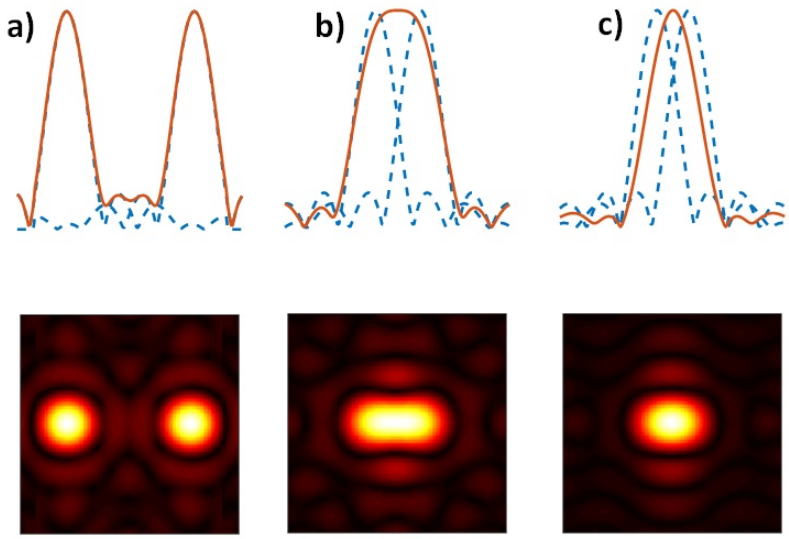

Fig. 1.3 (a) Completely resolved sources. (b) Sources separated by a FWHM of the PSF. (c) Sources separated by less than a FWHM of the PSF.

weak scattering regime, for example close to the surface of the imaged organs. When photons travel deeper into biological tissue they undergo scattering and even diffraction-limited focusing is no longer possible. The greater the imaging depth, the more scattering events occur and the more difficult it is to provide a tight focusing.

There are two characteristic lengths to estimate the degree of scattering: the scattering mean free path (scattering MFP) and the transport mean free path (transport MFP). At the depths smaller than the scattering MFP most photons preserve their initial direction. Such photons are called ballistic photons. When light propagates in a scattering and absorbing medium, its ballistic intensity decays according to the Beer-Lambert law:

$$I = I_0 e^{-\mu_e z}, \tag{1.1}$$

where μ_e is the extinction coefficient which is the sum of the absorption coefficient μ_a and the scattering coefficient μ_s. It should be noted that all these three coefficients are wavelength-dependent. The scattering MFP $l_s = 1/\mu_s$ can be viewed as the distance between two consecutive scattering events. The transport MFP is given by $l^* = \frac{l_s}{1-g}$, where g is the anisotropy factor which is defined by the direction of the scattered light. For biological tissues, where light is mostly scattered in the forward direction, the anisotropy factor g will be between 0.8 and 1. There are few ballistic photons between the scattering MFP and the transport MFP. The transport MFP l^* can be considered as the propagation distance at which the photons lose the memory of their initial incident direction and light propagation becomes isotropic.

With the notion of the scattering and transport MFP two regimes of light propagation can be defined: the weak scattering regime (below scattering MFP), and the scattering regime which includes intermediate scattering (between the scattering MFP and the transport MFP) and strong scattering (beyond transport MFP). In tissues in the near-infrared the scattering MFP is $\sim 100\ \mu m$ and the transport mean free path is around 1 mm [Ntziachristos, 2010].

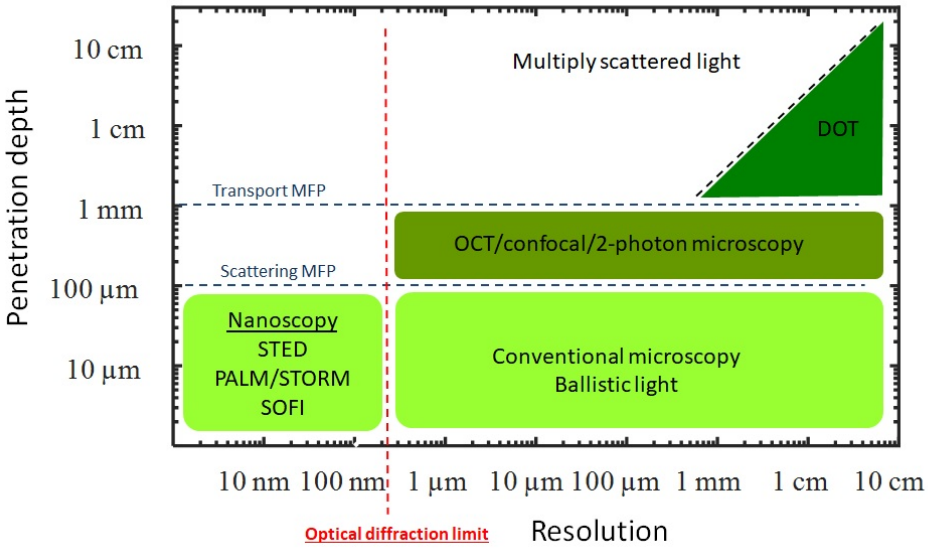

Fig. 1.4 Resolution limits and penetration depth for pure optical imaging techniques.

So, in the general case resolution is affected by both diffraction and scattering. Various techniques have been developed to perform imaging beyond the diffraction limit or in a highly scattering environment. Fig. 1.4 schematically summarizes the position of the most typical optical imaging techniques in the depth vs. resolution space, along with their scattering and diffraction limits.

1.2.1 Optical imaging beyond the diffraction limit

To overcome the diffraction limit in the weak scattering regime, a number of methods have been proposed, including Photo-activated Localization Microscopy (PALM) [Betzig et al., 2006], Stochastic Optical Reconstruction Microscopy (STORM) [Rust et al., 2006], Stimulated Emission Depletion (STED) [Hell and Wichmann, 1994] microscopy and Super-resolution Optical Fluctuation Imaging (SOFI) [Dertinger et al., 2009]. With the advent of these methods, imaging far beyond the optical diffraction limit became possible for the first time. Eric Betzig, Stefan W. Hell and William E. Moerner were awarded the Nobel Prize in Chemistry 2014 for the development of PALM and STED microscopy.

PALM and STORM rely on random activation of different sparse subsets of fluorescent molecules. By accumulating the positions of distinguishable sources on each acquired diffraction-limited image, a super-resolved image is obtained. The STED technique functions by depleting fluorescence in specific regions of the sample while leaving the center focal spot active to emit fluorescence. This is achieved by exploiting the non-linear response of fluorescent particles to the incident illumination. As a result, only the photons emitted by fluorescent particles residing in a doughnut-shape region of the focal spot are detected leading to the resolution improvement determined by the size of the active zone.

SOFI is based on independent fluorescence fluctuations from different fluorophores. By applying high order statistical analysis to a series of acquired diffraction-limited images, closely spaced emitters can be resolved.

More detailed description of optical super-resolution methods relevant to this work will be given in the corresponding chapters of this PhD manuscript.

1.2.2 Optical imaging in the scattering regime

Several optical techniques have been developed to reach diffraction-limited resolution in imaging beyond the scattering MFP. In general, these techniques exploit light in the near-infrared region 600-900 nm as this region offers the greatest penetration depth (extending to several centimetres) in biological tissues. Among the most popular techniques for imaging between the scattering MFP and the transport MFP are confocal microscopy [Pawley, 2010], two-photon microscopy [Helmchen and Denk, 2005] and Optical Coherence Tomography (OCT) [Huang et al., 1991]. These methods are based on optical sectioning, i.e. the 3D object is imaged slice by slice. The central idea of these methods is to prevent photons that do not originate from the imaged slice from reaching the detector. In confocal microscopy, this is achieved by using a pinhole in front of the detector. In two-photon microscopy, two-photon excitation of fluorophores is used to reduce the PSF size in the axial direction. In OCT photons originating from

the imaged plane are selected by interferometry.

Imaging beyond the transport mean free path can be done with Diffuse Optical Tomography (DOT) [Hoshi and Yamada, 2016]. In DOT, the imaged object is illuminated in the near-infrared spectral region and the light scattered while propagating in tissue is detected at many positions. Image reconstruction in DOT is based on modelling propagation of photons in highly scattering media. Due to the complexity of the reconstruction inverse problem, the depth-to-resolution ratio in DOT turns out to be of the order of 1.

1.3 Photoacoustic imaging

1.3.1 Introduction

Resolution similar to that of pulse-echo imaging can be achieved in acoustic-resolution photoacoustic imaging (AR-PAI) which permit imaging up to several centimeters beyond the transport MFP [Wang and Hu, 2012; Beard, 2011; Yao and Wang, 2013]. While light is highly scattered at such depths, it is also absorbed and through this absorption acoustic waves can be generated. As ultrasonic scattering in tissues ($\sim 1.2 \times 10^{-3}\ mm^{-1}$ in human skin at 5 MHz [Sehgal and Greenleaf, 1984]) is much weaker than optical scattering ($\sim 10\ mm^{-1}$ in human skin at 700 nm), it is possible to perform imaging with acoustic diffraction-limited resolution by collecting the generated acoustic waves. As a result, a depth-to-resolution ratio of the order of 100 can be achieved in conventional AR-PAI. At depths of the orders of ten centimeters the light intensity becomes too weak for the generated PA waves to be detected.

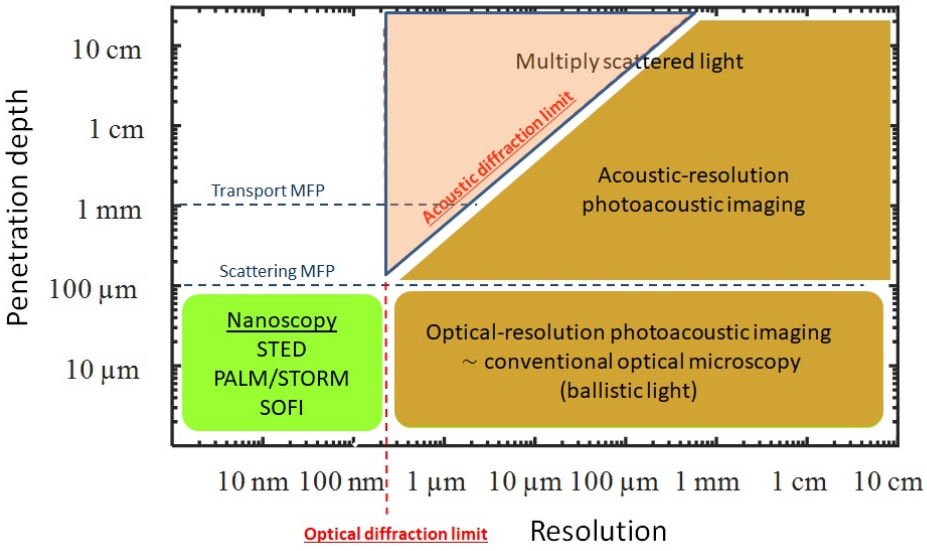

Fig. 1.5 Position of acoustic-resolution and optical-resolution photoacoustic imaging in the depth vs resolution space.

Fig. 1.5 shows how PA imaging deals with the resolution problem. Although AR-PAI permits imaging beyond the limit of conventional optical techniques and beyond the transport MFP, its resolution remains modest at high depths. In this PhD study we will fill this gap by developing methods to improve resolution in deep-tissue PA imaging.

1.3.2 Photoacoustic generation

The PA effect consists of emission of ultrasound (US) waves caused by light absorption. Absorption of light typically leads to a small temperature rise (less than 0.1 K) that induces a pressure rise [Beard, 2011]. This pressure rise relaxes in the form of a broadband (approx. tens of megahertz) low-amplitude (less than 10 kPa) acoustic wave which propagates in the medium until it is detected by an US probe.

1.3.2.1 Principle

In the context of AR-PAI relevant to this PhD study, PA imaging is performed in the heat confinement regime. This means that there is no significant heat diffusion over the sample volume during light absorption. Mathematically, this condition is formulated as

$$\tau_p << \tau_{th} = \frac{D_a^2}{\chi}, \tag{1.2}$$

where τ_p is the laser pulse duration, D_a is the characteristic size of the absorber, and χ is the heat diffusion coefficient ($\chi \approx 1.4 \times 10^{-7}\ m^2/s$ in water at 20°C). For a typical pulse duration of $\tau_p = 5\ ns$ condition (1.2) is fulfilled when $D_a >> 27\ nm$. In this PhD study, the minimal size of absorbers is $D_a = 10\ \mu m$, so in the following, we will always assume that condition (1.2) is satisfied.

The PA effect is then described by the following equation [Wang and Wu, 2012]:

$$\Big[\frac{\partial^2}{\partial t^2} - v_s^2\Delta\Big]p(\overrightarrow{r},t) = \Gamma\mu_a(\overrightarrow{r})\frac{\partial\phi_r(\overrightarrow{r},t)}{\partial t}, \tag{1.3}$$

where $p(\overrightarrow{r},t)$ is the PA pressure wave, $\phi_r(\overrightarrow{r},t)$ is the fluence rate , v_s is the speed of sound ($\approx 1500\ m/s$ in water at 20°C), $\mu_a(\overrightarrow{r})$ is the distribution of optical absorption, Γ is the constant called the Gruneisen parameter ($\Gamma \approx 0.1$ in water at 20°C).

1.3.2.2 PA point source

The PA point source is an absorber small enough that PA generation only depends on its absorption cross-section. For $\tau_p = 5$ ns light pulses, an absorber can be considered [Calasso et al., 2001] as a point source when its size is much smaller than typically 7.5 μm. For the PA point source, it can be shown that the pressure field $p(\overrightarrow{r},t)$ is

a spherical wave whose amplitude is proportional to the time derivative of the light intensity I:

$$p(\overrightarrow{r},t) \sim \frac{dI(\hat{\tau})}{d\hat{\tau}}, \text{ where } \hat{\tau} = \frac{t - ||\overrightarrow{r}||/v_s}{\tau_p}. \tag{1.4}$$

Fig. 1.6 shows a typical PA signal and its spectrum corresponding to a point-like absorber illuminated by a $\tau_p = 5$ ns light pulse.

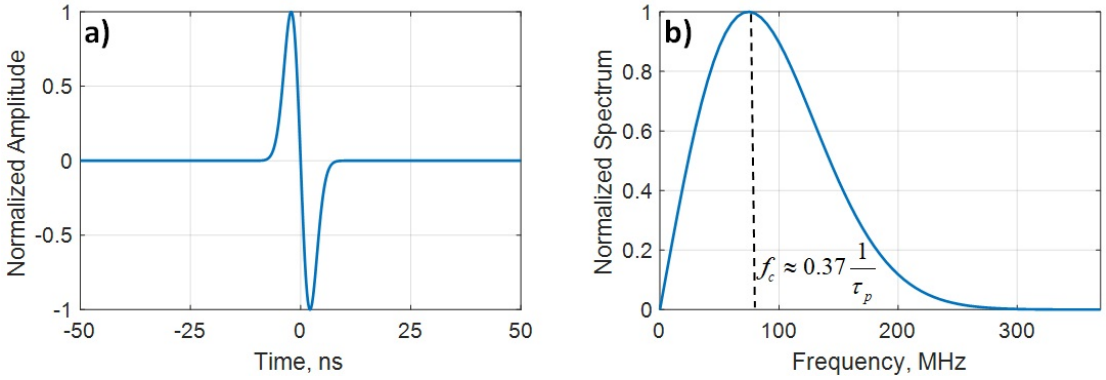

Fig. 1.6 (a) PA signal from a point-like absorber illuminated by a $\tau_p = 5$ ns light pulse. (b) Spectrum of the signal in (a).

1.3.2.3 Stress confinement regime

The stress confinement regime means that propagation of acoustic waves across the absorber during the illumination can be neglected. This condition can be formulated as

$$\tau_p << \tau_{ac} = \frac{D_a^2}{v_s}, \tag{1.5}$$

For a typical pulse duration of $\tau_p = 5\ ns$ condition (1.5) is satisfied when $D_a > 7.5\ \mu m$ [Calasso et al., 2001].

In the heat and stress confinement regime, light absorption can be considered instantaneous:

$$\phi_r(\overrightarrow{r},t) = \phi(\overrightarrow{r})\delta(t). \tag{1.6}$$

Then, the source term in (1.3) can be replaced by initial conditions as follows:

$$\begin{aligned} &\left[\frac{\partial^2}{\partial t^2} - v_s^2\Delta\right]p(\overrightarrow{r},t) = 0, t > 0 \\ &p(\overrightarrow{r},t=0) = p_0(\overrightarrow{r}) = \Gamma\mu_a(\overrightarrow{r})\phi(\overrightarrow{r}) \\ &\frac{\partial p}{\partial t}(\overrightarrow{r},t) = 0 \end{aligned} \tag{1.7}$$

In the heat and stress confinement regime, the duration of a PA signal is determined

by the size of the absorber and the speed of sound. The spectrum of such signal will have a characteristic frequency which is inversely proportional to the absorber size. An example is provided in Fig. 1.7 which shows PA signals emitted by a $D_a = 100\ \mu m$ cylinder and a $D_a = 100\ \mu m$ sphere [Diebold and Sun, 1994] as well as the spectra of these signals.

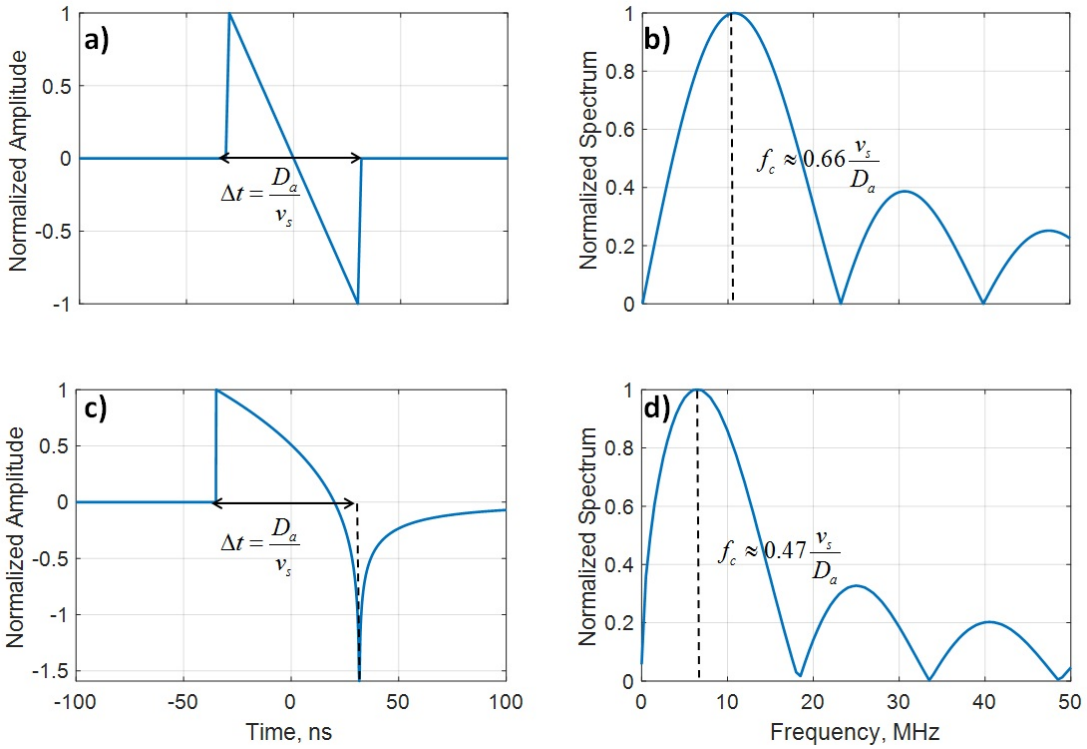

Fig. 1.7 (a,b) PA signal emitted by a $D_a = 100\ \mu m$ sphere and its spectrum. (c,d) PA signal emitted by a $D_a = 100\ \mu m$ cylinder and its spectrum.

1.3.3 Principles of acoustic-resolution photoacoustic imaging

In this section, we describe general principles of conventional AR-PAI. In particular, we consider image reconstruction, classical resolution limits and compare the frequency content of PA signals corresponding to different absorbers.

1.3.3.1 Conventional image reconstruction in AR-PAI

PA reconstruction consists of finding the initial pressure distribution $p(\overrightarrow{r}, t = 0)$ from measurement of $p(\overrightarrow{r}, t)$ at the surface of the probe. The solution $p_0 = p(\overrightarrow{r}, t = 0)$ to Eq. (1.7) can be obtained using the following equation [Xu and Wang, 2005]:

$$p_0(\overrightarrow{r}) = \int_{S_0} \left[2p(\overrightarrow{r_0}, t) - 2t \frac{\partial p(\overrightarrow{r_0}, t)}{\partial t} \right]_{t = \frac{|\overrightarrow{r} - \overrightarrow{r_0}|}{v_s}} \frac{d\Omega_0}{\Omega_0}, \tag{1.8}$$

where $\overrightarrow{r_0}$ is the positions on the transducer surface, S_0 is the reception aperture corresponding to the solid angle $\Omega_0 = 2\pi$ in a planar geometry. In the following, we will use the discretized version of $p(\overrightarrow{r_0}, t)$ which is the pressure $p(\overrightarrow{r_k}, t_i)$ on transducer element k at time t_i.

Eq. (1.8) can be considered equivalent to delay-and-sum beamforming involving two terms. The reader is referred to Appendix 1 for more information on the beamforming algorithm.

It should be mentioned that in the far-field approximation it is the second term in the right hand side of Eq. (1.8) that is dominant [Xu and Wang, 2005]. However, in real imaging conditions taking the derivative of received pressure signals is challenging due to the presence of noise.

Quantitative estimation of the pressure field $p_0(\overrightarrow{r})$ using Eq. (1.8) also entails other difficulties. Via the linear response of the transducer, the pressure $p(t_i, \overrightarrow{r_k})$ is related to the signal $S(t_i, k)$ available at the output of the acquisition machine. However, this response is a non-trivial function that depends on the transducer properties and the positioning of PA sources. In addition, Eq. (1.8) does not include effects related to propagation in the viscous medium, such as acoustic wave attenuation. The transducer response and effects related to propagation in the medium can both be taken into account in model-based reconstruction based on the signals $S(t_i, k)$ corresponding to a PA point source are measured experimentally or predicted theoretically. We will employ the model-based approach to demonstrate super-resolution in Chapters 5 and 6.

On the other hand, Eq. (1.8) is effectively used in conventional PA imaging to perform qualitative reconstruction. In particular, a qualitative estimate of absorbed energy is obtained by applying delay-and-sum beamforming to the signals $S(t_i, k)$ which are related in a complex manner to the pressure $p(\overrightarrow{r_0}, t)$ in the right hand side of Eq. (1.8). We will use this approach to demonstrate the result of standard PA reconstruction in all Chapters of this PhD manuscript.

1.3.3.2 Resolution in AR-PAI

In AR-PAI resolution is determined by acoustic diffraction. Thus, for a spherically focused ultrasound transducer of diameter D, central frequency f_c and bandwidth Δf the lateral resolution defined as the lateral FWHM of the amplitude PSF at distance R from the transducer surface is:

$$\Delta X = \Delta Y \sim \lambda_{ac} \frac{R}{D}, \tag{1.9}$$

where $\lambda_{ac} = \frac{v_s}{f_c}$ is the wavelength corresponding to the central frequency of the transducer.

The axial resolution is given by

$$\Delta Z = v_s \Delta\tau \sim \frac{v_s}{\Delta f} = \lambda_{ac} \frac{f_c}{\Delta f}, \tag{1.10}$$

with $\Delta\tau$ being the duration of the imaging pulse.

For wideband resonance transducers, the ratio $f_c/\Delta f$ is usually of the order of 1. So, in AR-PAI, classical resolution in the lateral and axial directions is limited by the acoustic wavelength.

1.3.3.3 Frequency content of detected PA signals

In this PhD study, imaging is always performed with wideband resonant transducers, which only detect signals within their frequency bandwidth.

Fig. 1.8 shows a typical transducer transfer function in the time domain and in the frequency domain. The frequency response is symmetric with respect to the central frequency f_c and has a certain full width at half maximum (FWHM) denoted Δf.

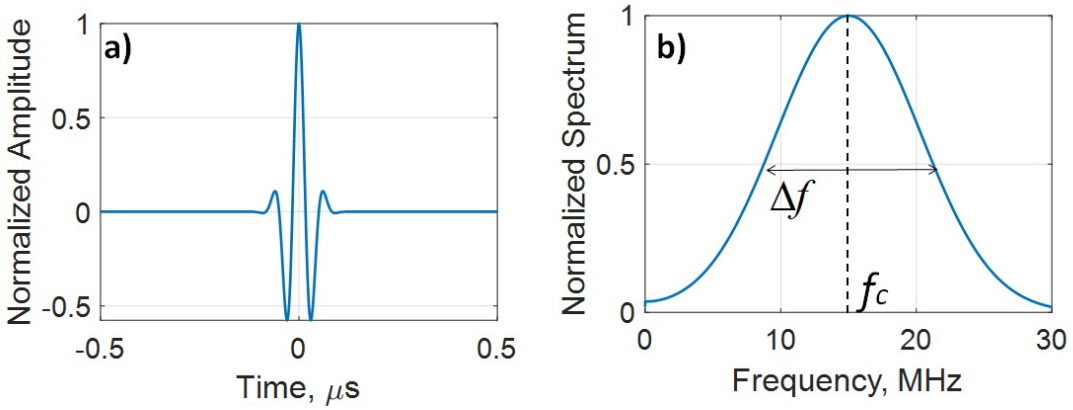

Fig. 1.8 Typical transducer response (a) and its spectrum (b). Central frequency $f_c = 15$ MHz, bandwidth $\Delta f = 13$ MHz.

When a PA signal is detected, the transducer transfer function shown in Fig. 1.8 acts as a band-pass filter. Fig. 1.9 illustrates typical signals detected by a transducer with the characteristics shown in Fig. 1.8 for the case of a point source (a), a 100-um diameter sphere (b), and a 100-um diameter cylinder (c).

It can be observed that the shape of the output signal is determined by the transducer response rather than the imaged object (Fig. 1.6 and 1.7). In the present work, different types of absorbers are considered, including red blood cells and beads (both about 10 μm in diameter) as well as microfluidic channels with typical dimensions of a few tens of micrometers. A given transducer will in principle detect the waves emitted by all these types of absorbers, but with a SNR strongly dependent on the position of the input PA spectrum with respect to the spectral response of the transducer.

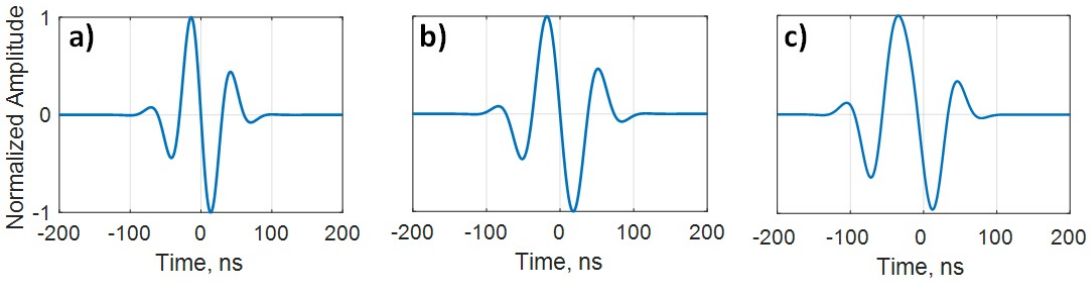

Fig. 1.9 Normalized PA signals detected by a transducer with the characteristics shown in Fig. 1.8 for the case of a point source (a), a 100-μm diameter sphere (b), and a 100-μm diameter cylinder (c).

1.3.4 Linear array imaging

1.3.4.1 Transducer geometry

In this PhD study, multielement linear arrays are used for detection of acoustic waves (Fig. 1.10). Such arrays permit obtaining two-dimensional (2D) PA images in a single acquisition as detection is performed in parallel by a number of quasi-identical transducer elements. By translating or rotating the array in space, volumetric reconstruction can be achieved.

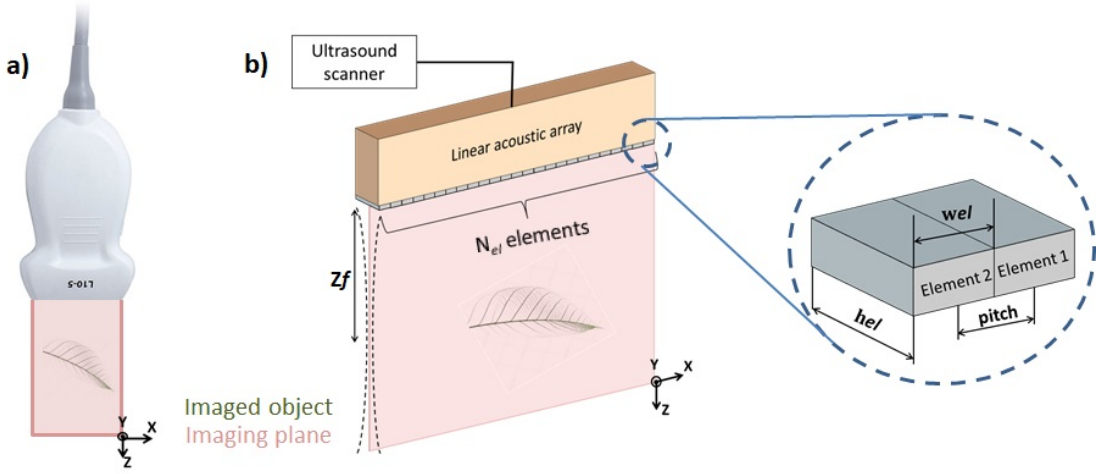

Fig. 1.10 (a) Imaging geometry with a linear transducer array. (b) Detailed scheme of imaging geometry with a linear transducer array. Inset: two neighbouring transducer elements with relevant dimensions: element width w_{el}, element height h_{el}, and element pitch.

The transducer elements usually have a rectangular shape and are arranged in a single row. The width w_{el} and the height h_{el} of each element are chosen to provide the required properties of the probe, including sensitivity and resolution. On the one hand, the area of each element should be large to provide a good sensitivity. On the other hand, the spacing between neighbouring elements should not exceed $\lambda_{ac}/2$ ($\lambda_{ac} = v_s/f_c$ is

the wavelength at the central frequency f_c of the transducer) to avoid artifacts due to spatial undersampling. So, in practice there is virtually no space between neighbouring transducer elements and the center-to-center distance between the elements, called the *element pitch*, is very close to the element width w_{el}. The element height h_{el} usually determines elevational focusing in the Y direction at a certain distance z_f from the transducer surface. This mechanical focusing is achieved by using an acoustic lens at the transducer surface and permits suppressing signals from sources outside the imaging plane XZ.

1.3.4.2 Point Spread Function

Fig. 1.11 illustrates a typical PA acquisition corresponding to a single point source in the imaging plane XZ. Fig. 1.11b shows the data which is available at the output of the acquisition machine after recording PA signals. This data is usually called a radio-frequency frame or an *RF frame*. Each value of the RF frame corresponds to the signal $S(t_i, k)$ which is equal to the quantized value of voltage on transducer element k registered at time t_i. The interval between successive time values t_i and t_{i+1} is equal to $\Delta t_s = 1/f_s$, where f_s is the sampling frequency of the acquisition machine. As can be clearly seen, a PA acquisition results in a curved trajectory on the RF frame. The shape of this trajectory is determined by the arrival time of the PA signal on different transducer elements. It can be noticed that some background noise is also present in Fig. 1.11b. This noise results from thermal noise of the acquisition equipment and usually determines the signal-to-noise ratio (SNR) in PA imaging.

Fig. 1.11c illustrates the bipolar PSF derived by applying delay-and-sum beamforming to the RF data shown in Fig. 1.11b. This PSF contains axial oscillations resulting from the finite transducer bandwidth. These oscillations can be removed (see Appendix 1) to obtain what can be called the envelope PSF, which is shown in Fig. 1.11d. Note that any linear operation should involve the PSF and not its envelope, as taking the envelope is not a linear operation. The full width at half maximum of the envelope PSF is determined by the diffraction-limited resolution in the lateral direction X:

$$\Delta X \sim \lambda_{ac} \frac{R}{D} \tag{1.11}$$

and in the axial direction Z:

$$\Delta Z \sim \lambda_{ac} \frac{f_c}{\Delta f}. \tag{1.12}$$

In Eq. (1.11) and (1.12) R is the distance from the transducer surface to the source, f_c is the central frequency of the transducer, Δf is the transducer bandwidth, and $D = pitch * N_{el}$ is the length of the linear array. Imaging is usually performed at the depth

corresponding to the elevational focal distance of the transducer, i.e. at $R \sim z_f$.

The size of the elevational focal zone determines the diffraction-limited resolution in the direction Y perpendicular to the imaging plane XZ:

$$\Delta Y \sim \lambda_{ac} \frac{z_f}{h_{el}}, \tag{1.13}$$

where h_{el} is the height of a transducer element.

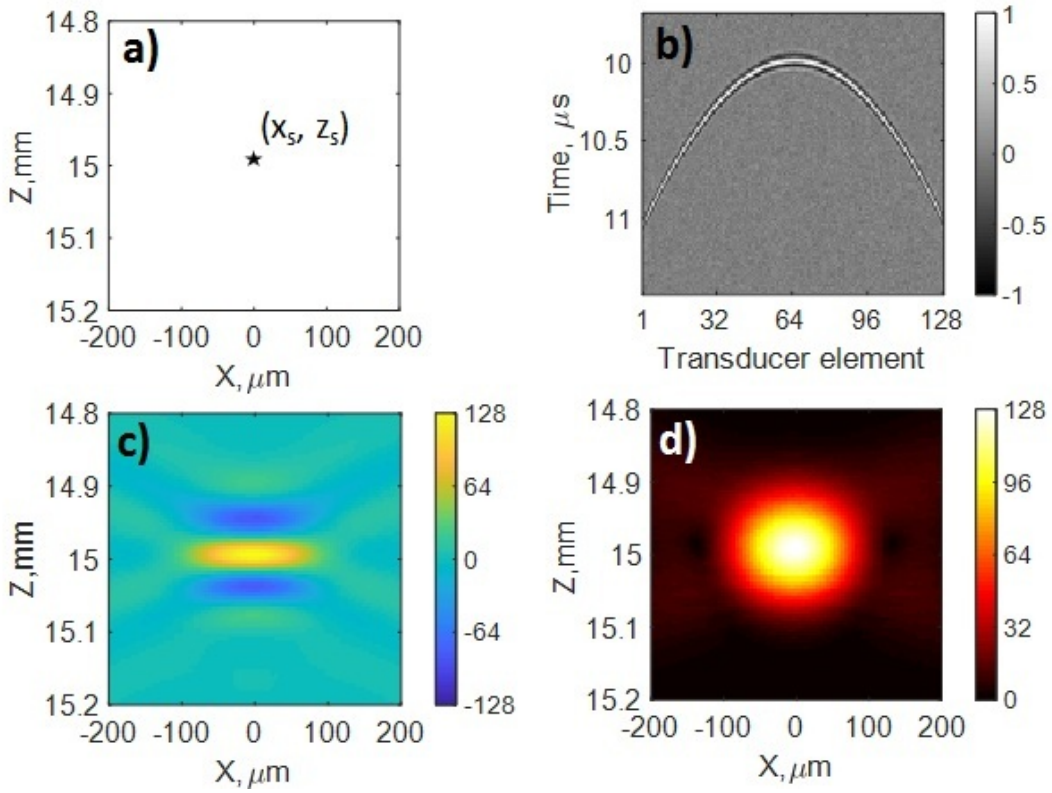

Fig. 1.11 (a) Single point source in the imaging zone. (b) RF frame corresponding to PA imaging of the point source in (a). (c) Bipolar PSF corresponding to the RF data in (b). (d) Envelope PSF corresponding to the RF data in (b).

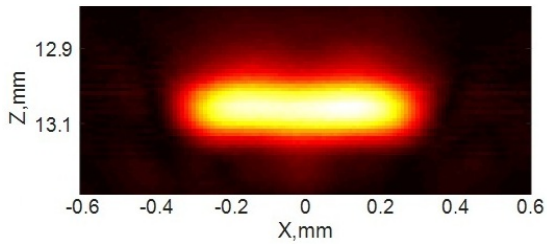

Fig. 1.12 Five point-like absorbers too close from each other appear as a continuous unresolved distribution due to a finite size of the PSF.

Based on the PSF shown in Fig. 1.11, Fig. 1.12 illustrates how five point-like absorbers very close from each other appear as a continuous unresolved distribution.

The main objective of this PhD thesis is to propose and investigate methods to overcome the acoustic diffraction limit observed in Fig. 1.12.

1.4 State-of-the-art and objectives of this thesis

Photoacoustic (PA) imaging is the cross-sectional or three-dimensional (3D) imaging of a material using the photoacoustic effect [Wang and Wu, 2012; Beard, 2011; Yao and Wang, 2013]. A PA image can be viewed as an ultrasound image in which the contrast depends not on the mechanical and elastic properties of the tissue, but on its optical properties, most specifically optical absorption [Beard, 2011]. PA imaging may provide better tissue differentiation and specificity than ultrasound (US) because differences in optical absorption between different tissues can be more significant than those in acoustic impedance. For example, due to the strong optical absorption of haemoglobin PA imaging is used to visualize the microvasculature that can be hard to image in pulse-echo ultrasound imaging because of the weak echogenicity (although recently developed ultrasound Doppler imaging techniques [Mace et al., 2013] may now provide visualization quality comparable to that of PA imaging). In addition to visualizing anatomical structures, PA imaging can also provide functional information on blood oxygenation, blood flow and temperature. All of this can be achieved over a wide range of length scales from micrometres to centimetres with scalable spatial resolution. These attributes lend PA imaging to a wide variety of applications in clinical medicine, preclinical research and basic biology for studying cancer, cardiovascular disease, abnormalities of the microcirculation and other conditions [Beard, 2011]. In PA imaging, pulsed illumination in the visible and near-infrared part of the spectrum between 550 and 900 nm is usually used. Signal acquisition can be performed by a single element transducer or a multielement array. Such probes are usually those that are used in US imaging, where they are employed not only for reception but also for transmission of acoustic waves. The frequency of PA signals typically ranges from 1 to 100 MHz [Beard, 2011]. Optical-resolution photoacoustic imaging (OR-PAI) and acoustic-resolution photoacoustic imaging (AR-PAI) have been briefly presented in section 1.2. In OR-PAI optical resolution is achievable, but the penetration depth of this technique is limited to about 100 μm in biological tissues, as for other optical microscopy techniques. Although AR-PAI allows a greater penetration depth (up to several centimeters), its resolution remain restrained by acoustic diffraction, leading to a depth-to-resolution ratio of about 100 (Fig. 1.5).

The main goal of the actual PhD study is to propose methods to overcome the diffraction limit in acoustic-resolution PA imaging. Besides the acoustic diffraction barrier, we will also try to overcome one other important limitation in AR-PAI. The

issue is that some parts of the imaged objects may be invisible after PA reconstruction. Such artifacts usually arise due to the coherent simultaneous generation of PA waves by all parts of the object. As a result, the limited bandwidth or the limited detection aperture of the US transducer may lead to what can be called visibility problems.

There have already been some attempts to achieve super-resolution in AR-PAI. These attempts were based on random optical speckle illuminations, each illumination leading to a random distribution of PA sources inside the imaged object. By processing PA images acquired for different illumination patterns, super-resolution can be achieved. For example, Chaigne et al. [Chaigne et al., 2016] showed that by calculating the variance PA image a $\sqrt{2}$ resolution improvement can be achieved. Some other works suggested using the so-called model-based approach to obtain super-resolved images [Hojman et al., 2017; Murray et al., 2017]. Briefly speaking, model-based reconstruction involves a forward linear model expressed as $R = AT$, where R is the acquired PA images, T is the object to reconstruct, A is a PSF-encoding matrix. Model-based reconstruction usually exploits some additional assumptions on the object, such as *sparsity* [Murray et al., 2017]. It was shown that in terms of resolution model-based reconstruction outperforms the variance-based approach [Murray et al., 2017] and Richardson-Lucy deconvolution [Hojman et al., 2017; Murray et al., 2017]. In addition, it was proposed to use speckle illuminations to overcome the limited-view and limited-bandwidth problems in AR-PAI [Gateau et al., 2013].

However, a great disadvantage of using optical speckle illuminations, whether to achieve super-resolution or to palliate visibility problems, is that in deep-lying tissues the size of the optical speckle grain is several orders of magnitude smaller than that of the acoustic PSF [Gateau et al., 2013]. This difference in dimensions leads to a very small amplitude of fluctuations since the PA signal at each image pixel is the sum of PA signals from a large number of speckles fluctuating within the acoustic PSF [Goodman, 2007; Gateau et al., 2013]. For example, for speckles of size $\lambda_{laser}/2$ $\sim$0.3 μm (reached at $\sim$1 mm depth in biological tissues under near infrared [Ntziachristos, 2010]) and a typical acoustic wavelength λ_{ac} = 100 μm, the number of optical speckles inside the acoustic PSF is about $N = 10^6$ which makes it virtually impossible to extract the fluctuations of interest from the noise fluctuations. So, using optical speckle illuminations would be challenging in clinical applications of AR-PAI.

In this PhD study we propose and investigate super-resolution methods for deep-tissue PA imaging. These methods do not rely on optical speckle illuminations and can be implemented on a standard PA imaging system. We will consider methods based on

response from contrast agents as well as methods for contrast-free imaging, that may rely on fluctuations of red blood cells (RBCs) or just on a PA signal from the imaged microvasculature. Most of the proposed methods are developed based on the principles of super-resolution techniques introduced in optics and then partially adopted for US imaging. In the last chapter, we show that visibility problems in PA imaging can be successfully overcome by using PA signal fluctuations caused by a blood flow. After this general introductory chapter, the PhD manuscript is organized with the following structure:

Chapter 2. The experimental equipment is described, including the illumination source and the US acquisition equipment. A schematic of the experimental setup is illustrated. The fabrication of the microfluidic samples, used in most of the experiments, is briefly described.

Chapter 3. The principles of US super-localization imaging are used to form the basis of PA localization imaging, and the results of a proof-of-principle experiment are reported. Three methods of detecting localization sources are proposed. The limitations of the approach are discussed.

Chapter 4. The principles of super-resolution optical fluctuation imaging (SOFI) imaging are used to form the grounds of PA super-resolution imaging based on fluctuations of moving optical absorbers. The method is first illustrated with numerical simulations, and demonstrated experimentally with two proof-of-principle experiments, one relying on the fluctuations induced by flowing absorbing microbeads, the other relying on blood flow fluctuations. The limitations of the method are discussed.

Chapter 5. Model-based super-resolution is introduced and demonstrated experimentally. L1-norm-based reconstruction applied to mean and variance data are compared with both experimental and simulation results. Using simulations, model-based reconstruction applied to either raw RF data or beamformed images are also compared. The mechanism of L1-based reconstruction and the role of the non-negativity constraint is investigated theoretically. The limitations of model-based reconstruction are discussed.

Chapter 6. The model-based approach introduced in the previous chapter is applied to demonstrate super-resolution in both PA and US imaging with a small number of transducer elements (sparse array). Additional simulations are performed to investigate how the reconstruction quality depends on the number of transducer elements and the

signal-to-noise level.

Chapter 7. Fluctuations of moving optical absorbers are exploited to suppress visibility artifacts in PA imaging. The effect of the absorber size and the concentration of absorbers are studied theoretically.

Chapter 8. All the studied super-resolution methods are compared. The most recent advances in super-resolution PA imaging are discussed and an outlook for super-resolution PA imaging is provided.

CHAPTER 2

Experimental equipment, materials and methods

This chapter provides a description of the experimental equipment that was used in the course of this PhD study. First, an overview of the setup used in all experiments is presented, then a more detailed description of various instruments (light source, ultrasound acquisition electronics, etc.) along with their relevant specifications is provided. In the last section, microfluidic samples used in most experiments are described.

2.1 Experimental setup

A schematic of the experimental setup used in all the experiments is shown in Fig. 2.1. The sample is placed in a water tank perpendicularly to the imaging plane of a linear transducer array (type L7-4/L22-8, see section 2.5) such that the distance between the sample and the ultrasound probe is approximately equal to the elevational focus distance of the transducer. The pulsed laser ($\tau_p = 5\,ns$, $\lambda_{laser} = 532/670\,nm$, PRR=100 Hz, see section 2.2) illuminates the sample and at each laser shot photoacoustic (PA) signals are recorded by the multichannel acquisition electronics (Verasonics Vantage system, see section 2.3). In experiments with microbeads or human blood, the liquid is flown into the circuit with a syringe pump (KDS Legato 100, KD Scientific, Holliston, MA, USA) providing a controlled flow rate.

The voltage divider and the signal generator (BNC 575, Berkeley Nucleonics Corp., San Rafael, CA, USA) in Fig. 2.1 provide synchronization between the trigger signal levels of the acquisition electronics and the laser (see section 2.4). The bypass circuit is used to reduce the laser jitter (see section 2.2).

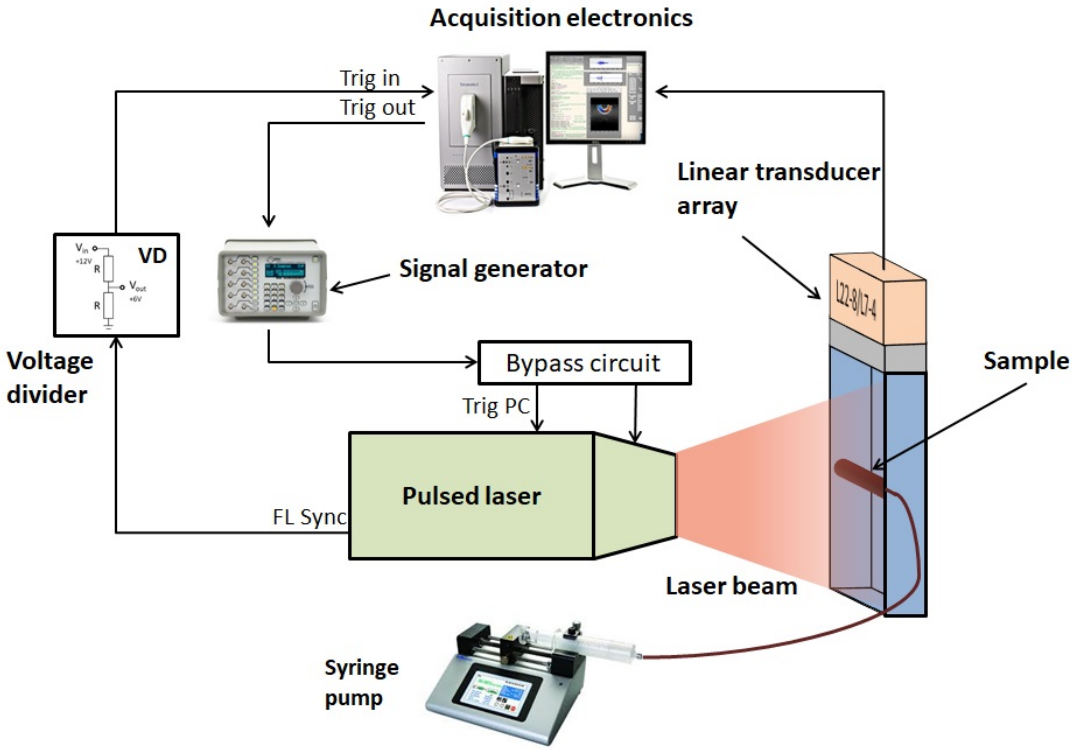

Fig. 2.1 Schematic of the experimental setup common to all the experiments. The sample placed in a water tank is illuminated by the pulsed laser and the acquired signals are registered by the acquisition electronics. The syringe pump provides a constant flow rate in the experiments with microbeads or human blood. The voltage divider and the signal generator provide synchronization between the trigger signals of the light source and the acquisition machine.

2.2 Light source

The light source is a diode-pumped Nd:YAG laser (Spitlight DPSS 250, Innolas Laser GmbH, Krailling, Germany) providing high-energy $\tau_p = 5$ ns light pulses with the maximal pulse repetition rate PRR=100 Hz. The laser wavelength 1064 nm permits obtaining light at 532 nm via the second harmonic generator (SGH) unit or light in the infraraed range 680-980 nm via the optical parametric oscillator (OPO) unit. In Chapters 3-6 light at 532 nm is used while in Chapter 7, illumination at 680 nm is exploited. A photo of the laser is shown in Fig. 2.2.

An important property of the laser is the laser jitter. The jitter indicates how well the emission of a laser pulse is synchronized with the trigger signal. For the laser used in this study, the default value of jitter is ± 20 ns meaning that the light pulse is emitted within a 40 ns time window. As in PA imaging a good synchronization between the beginning of PA acquisition and the moment of light emission is important, we reduced the default jitter down to ± 1 ns using a special bypass circuit (Fig. 2.1) ordered from the laser manufacturer.

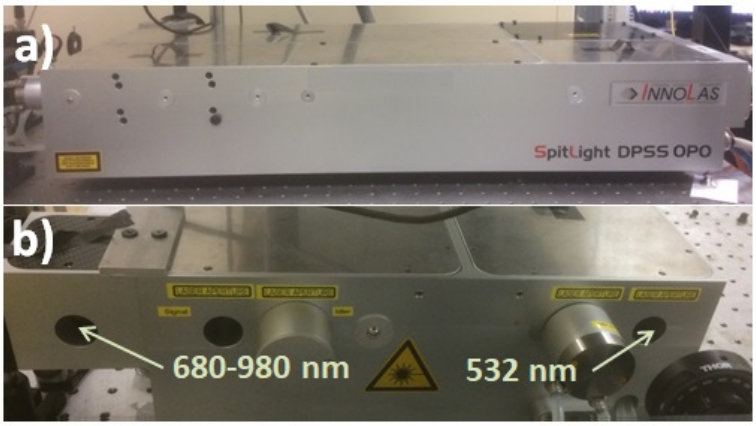

Fig. 2.2 (a) The laser head unit (side view). (b) The front view of the laser, with the output windows for 532 nm and 680-980 nm .

During acquisition of PA signals, the laser electronics produce noise that is captured by all elements of the US probe and appear as horizontal lines on the acquired radio-frequency (RF) frame (Fig. 2.3a). To remove this noise, we subtract the mean value for each line of the RF frame. This permits reducing the laser noise substantially (Fig. 2.3b). The position and amplitude of noise slightly fluctuate from one PA acquisition to the next. So, averaging over a certain number of frames can further reduce the noise. This can be done when the fluctuations of the relevant signal from one acquisition to the next can be neglected.

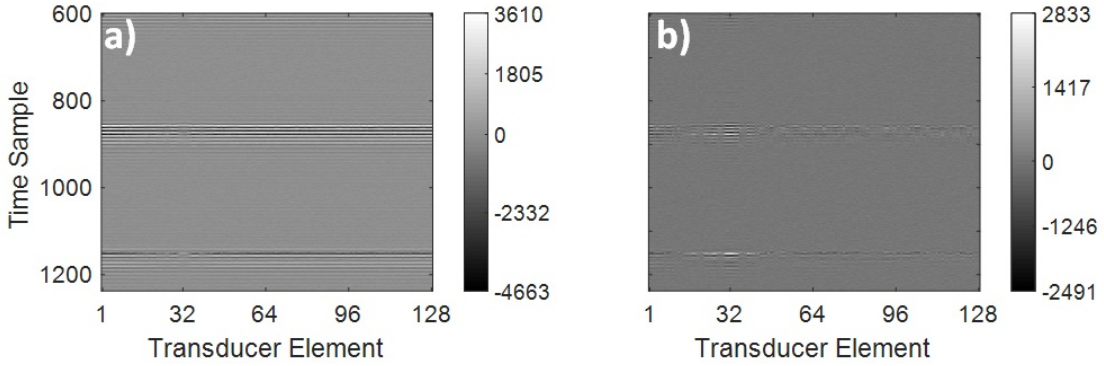

Fig. 2.3 (a) The laser noise appears as horizontal lines on the acquired RF frame. (b) This noise can be considerably reduced by subtracting the mean value over each line of the RF frame.

2.3 Ultrasound electronics

The acoustic part of the imaging equipment consists of US probes (section 2.5) connected to a High Frequency Vantage 256 system (Verasonics, Kirkland, WA, USA). In all our PA experiments the Vantage system is used for reception of acoustic waves, and in the only US experiment (Chapter 6), the machine is also used to transmit a plane

wave from the elements of a transducer array. The machine controls 256 independent transmit channels and 256 independent receive channels to connect multielement transducer arrays. Two Cannon HDI-format ZIF connectors are provided at the front of the system, each providing access to 128 channels (Fig. 2.4a).

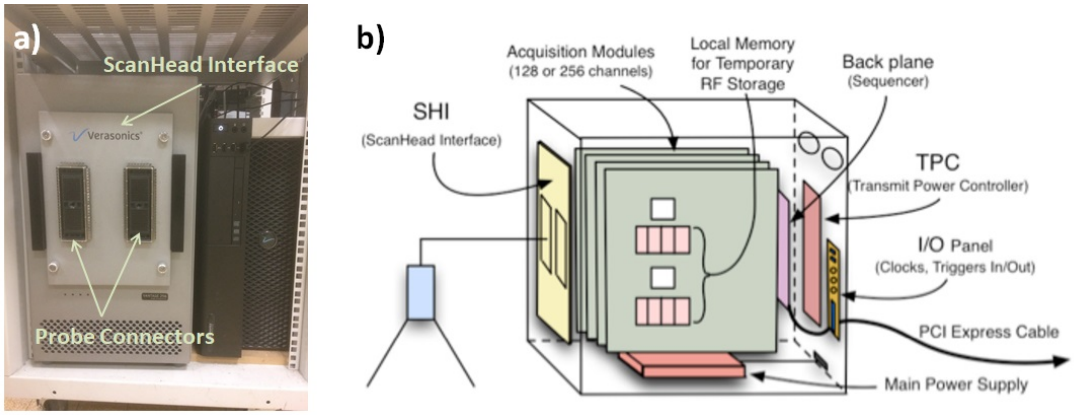

Fig. 2.4 High Frequency Vantage 256 system. (a) Probe connectors. (b) Main components of the Vantage system, including Scanhead Interface (SHI), Back Plane Module, Transmit Power Controller (TPC), I/O Panel .

A schematic of the main components of the Vantage system is shown in Fig. 2.4b. These components include:

- Scanhead Interface (SHI) - This is the module that contains the transducer connectors.
- Acquisition Modules (AM) - These electronic boards contain the circuitry for transmitting and receiving ultrasound signals for multiple channels. Each module supports up to 64 transmitters and 64 receive channels. The received US signals are digitized and stored in local memory on the AM prior to transfer to the host computer. The AM also provide the per channel digital filtering and and signal conditioning that can be applied after A/D conversion.
- Back Plane Module - This module contains the hardware sequencer that controls the operation of the Acquisition Modules.
- Transmit Power Controller (TPC) - The TPC module provides the high voltage power supply for the transmitters, as well as several other power supply levels used by the system.
- I/O Panel - The I/O Panel provides the PCI express cable connection for connecting to the host computer. It also provides the BNC connections for two input triggers and one output trigger, as well as clock outputs for synchronization with external devices.

The Vantage system provides several adjustable parameters to control reception of US waves and pre-processing of the acquired data.

To provide the best compatibility with the US probes, the imput impedance of the Vantage system can be tuned. We chose the highest value of the input impedance of approximately 8 Ohm (*RcvProfile.LnaZinSel = 31*).

The Vantage system has two controllable amplifiers that also provide high-pass filtering. For the preamplifier prior to the A/D (PGA) we chose the maximal gain of 30 dB (*RcvProfile.PgaGain = 30*) and the filter breakpoint at approximately 80 kHz (*RcvProfile.PgaHPF = 80*). For the low noise amplifier (LNA) we chose the maximal gain of 24 dB (*RcvProfile.LnaGain = 24*) and the filter breakpoint at approximately 200 kHz (*RcvProfile.LnaHPF = 200*).

The sampling frequency of the Vantage system can also be tuned. Specifically, we chose the sampling mode corresponding to the mode where the sampling frequency is set as close as possible to $f_s = 4 \times f_c$, where f_c is the central frequency of the ultrasound (US) probe (*Receive.samplesPerWave=4*). The frequency f_s is picked up from the discrete set of available sampling frequencies: on the high frequency version of the Vantage system used here, the maximum available sampling frequency is 62.5 MHz. This frequency is at least two times greater than the maximal frequency in the impulse response of each US probe that we used. In practice, the sampling frequency was 20.83 MHz and 62.5 MHz in the experiments with the L7-4 probe (f_s = 5 MHz) and the L22-8 probe (f_s = 15 MHz) correspondingly.

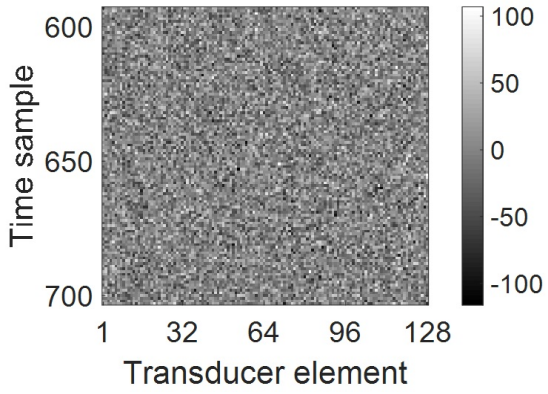

Fig. 2.5 Typical RF frame acquired in the absence of the imaged object and the laser noise.

The acquisition data is transferred to the host computer as a radio-frequency (RF) frame. The RF frame contains the quantized and pre-processed signals received by each transducer element at every time sample. Each value is a 15bit signal ranging from -16384 to +16384. An example of the RF frame acquired in the absence of imaged object and laser noise is shown in Fig. 2.5. This frame contains only the noise produced

by the acquisition pipeline (US probe and Vantage system). The rms of this noise is about $\sigma_n = 30$ for both US probes used in this study (see section 2.5).

2.4 Synchronization

In all the experiments, acquisition of PA signals is performed after illuminating the sample. To synchronize the beginning of the acquisition with the moment of illumination measures have been taken. To provide the minimal jitter, we compared three synchronization schemes:

1) The output trigger signal FL Sync from the laser pump source is sent to the US acquisition electronics (AE). The AE waits for a *fixed* time (until the light pulse is supposed to be emitted) and registration of PA signals begins. This scheme was rejected due to the large jitter between the FL Sync signal and the light emission (about 1 μs).

2) The output trigger signal from the laser Pockels cell is sent to the AE at the moment of light emission. On receiving this signal, AE begins registration of PA signals. This scheme was rejected due to the large jitter at the Trig In port of the AE (about 0.5 μs).

3) The adopted synchronization sequence providing the jitter of about 2 ns is schematically shown in Fig. 2.6. First the output trigger signal FL Sync from the laser pump source is sent to the AE. Then, the AE makes a pause of 230 μs to wait until the energy stored in the laser reaches its maximum. At this moment the AE generates the Trig Out signal that is sent to the input trigger of the Pockels cell of the laser. The state of the Pockels cell changes and the intracavity laser light is allowed to exit. This creates a high intensity laser pulse. The maximum of the output light intensity is reached approximately 400 ns after the Trig Out signal is sent. The maximal laser PRR being 100 Hz, the next pulse is generated 10 ms after the previous one.

As the input/output trigger levels of the laser and the AE are different, a voltage divider and a signal generator were used to provide the compatibility between the trigger signals. Fig. 2.7 shows the input and output signals of these devices.

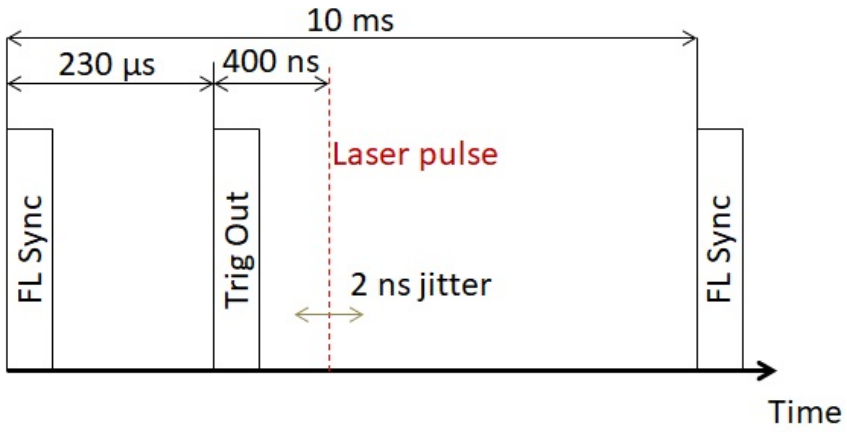

Fig. 2.6 Synchronization sequence for PA acquisition. The laser sends the output trigger signal FL Sync to the acquisition electronics which waits until the energy inside the laser reaches its maximum. Then, the Trig Out signal is sent by the acquisition electronics to the laser and a light pulse is generated. The minimal time between successive pulses is 10 ms.

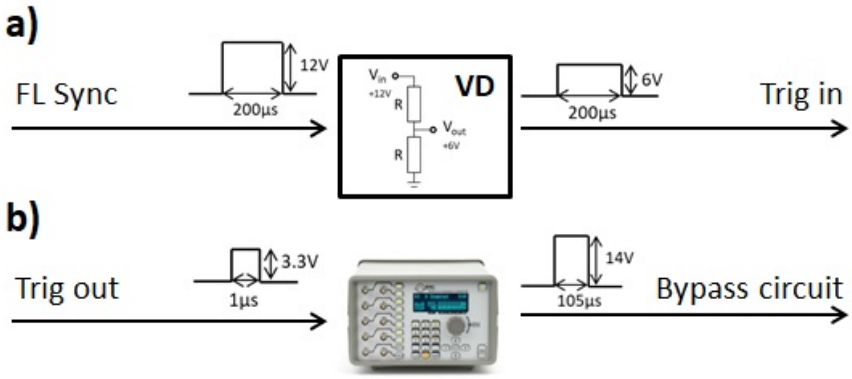

Fig. 2.7 (a) The voltage divider provides the correspondence between the FL Sync signal sent by the laser and the trigger circuit of the acquisition electronics. (b) The signal generator provides the correspondence between the Trig Out signal sent by the acquisition electronics and the trigger circuit of the laser.

2.5 Ultrasound probes

Two bandwidth-limited linear transducer arrays are used as US probes in the experiments: L22-8 (Capacitive Micromachined Ultrasonic Transducer (CMUT) linear array) and L7-4 (piezoelectric linear array), both manufactured by Verasonics Inc., Kirkland, WA, USA. Some characteristics of these probes are reported in Table 2.1. Notably, each probe has only one connector. This means that although the probe L22-8 has 256 elements, only 128 of them can be used simultaneously as each connector of the acquisition system can be used for simultaneous acquisition of at most 128 signals (see section 2.3).

Fig. 2.8 and 2.9 illustrate point spread functions (PSFs) acquired for the probe L22-

Model	Central frequency, MHz	Bandwidth at -3dB, MHz	Number of elements	Element pitch, μm	Element height, mm	Elevation focus, mm
L22-8	15	12	128 used out of 256	100	1.5	15
L7-4	5	5	128	310	7.5	25

Table 2.1 Characteristics of the US probes used in the experiments.

8 in PA and plane-wave US imaging correspondingly. Fig. 2.10 shows a PA PSF for the probe L7-4.

All the PSFs are acquired based on a small microfluidic channel (channel width and height being $w_{ch} = 10\ \mu m$ and $h_{ch} = 50\ \mu m$ correspondingly), placed perpendicularly to the imaging plane XZ at the elevational focus of the US probe. For a linear array transducer with focusing in elevation such a microchannel can be considered as a point source in the imaging plane XZ as the signals originating from the outside of the imaging plane are attenuated by the acoustic lens of the linear array.

In PA imaging, the PSFs were acquired by illuminating the channel filled with an absorbing liquid (Patent Blue V). In US imaging, the PSF was acquired by receiving the backscattered signals after sending a plane wave to the channel filled with air.

Standard delay-and-sum beamforming reconstruction [Xu and Wang, 2005] was then performed to measure the full width of maximum (FWHM) of the central lobe of each PSF in the X and Z directions. The FWHM in the Y direction was estimated using Eq. (1.13). The results are summarized in Table 2.2. It should be kept in mind that we define the conventional resolution of the imaging system based on the FWHM of the PSF (see section 1.2).

Model	Mode	ΔX, μm	ΔZ, μm	ΔY, mm
L22-8	PA	154	139	1
L7-4	PA	389	418	1
L22-8	US	154	80	1

Table 2.2 FWHM of the PSFs shown in Fig. 2.8-2.10.

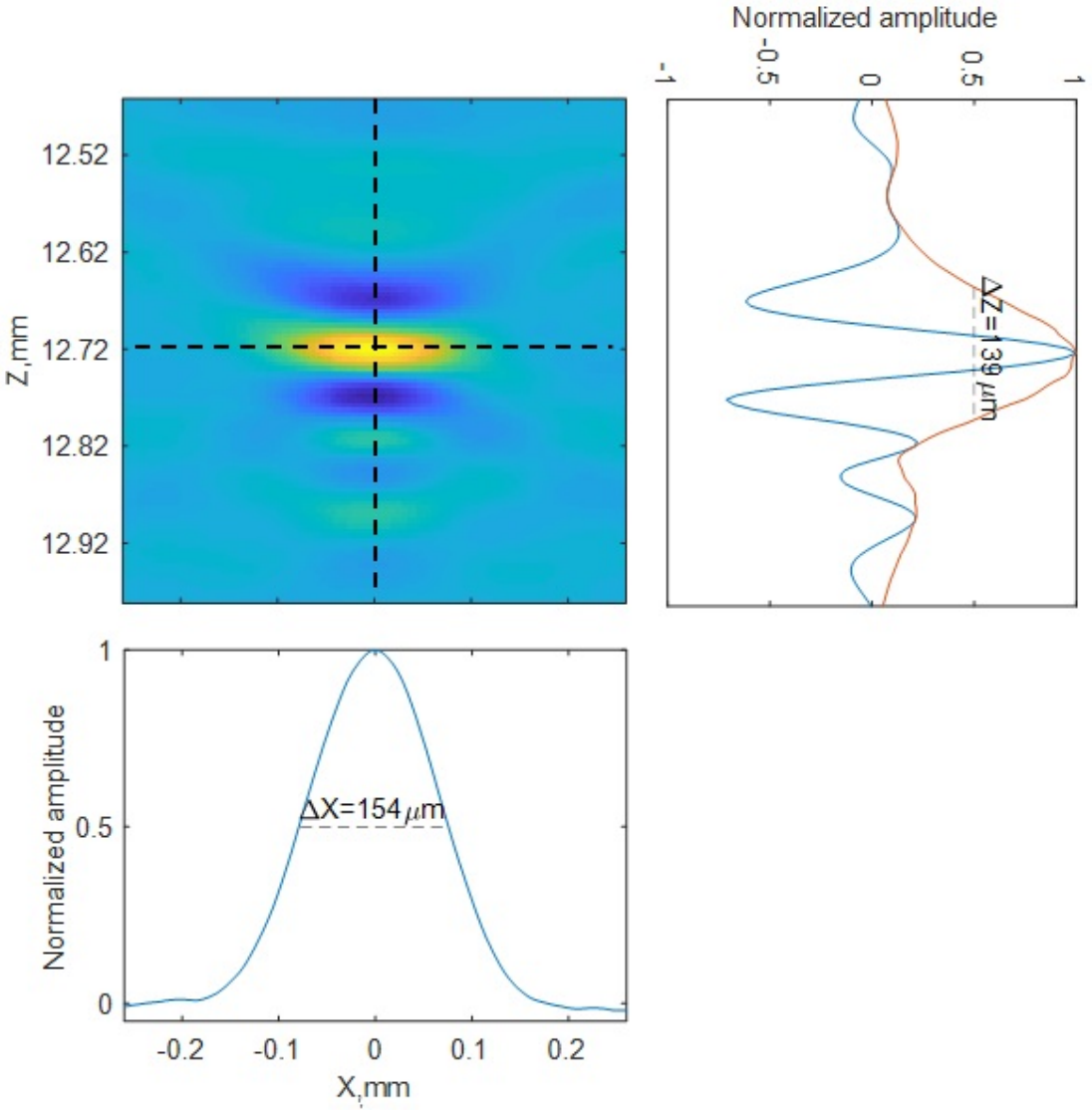

Fig. 2.8 PA PSF acquired with the L22-8 probe. The lateral dimension of the PSF, defined as the lateral FWHM of the central lobe, is about 154 μm. The axial dimension of the PSF, defined as the FWHM of the PSF envelope along the Z axis, is about 139 μm.

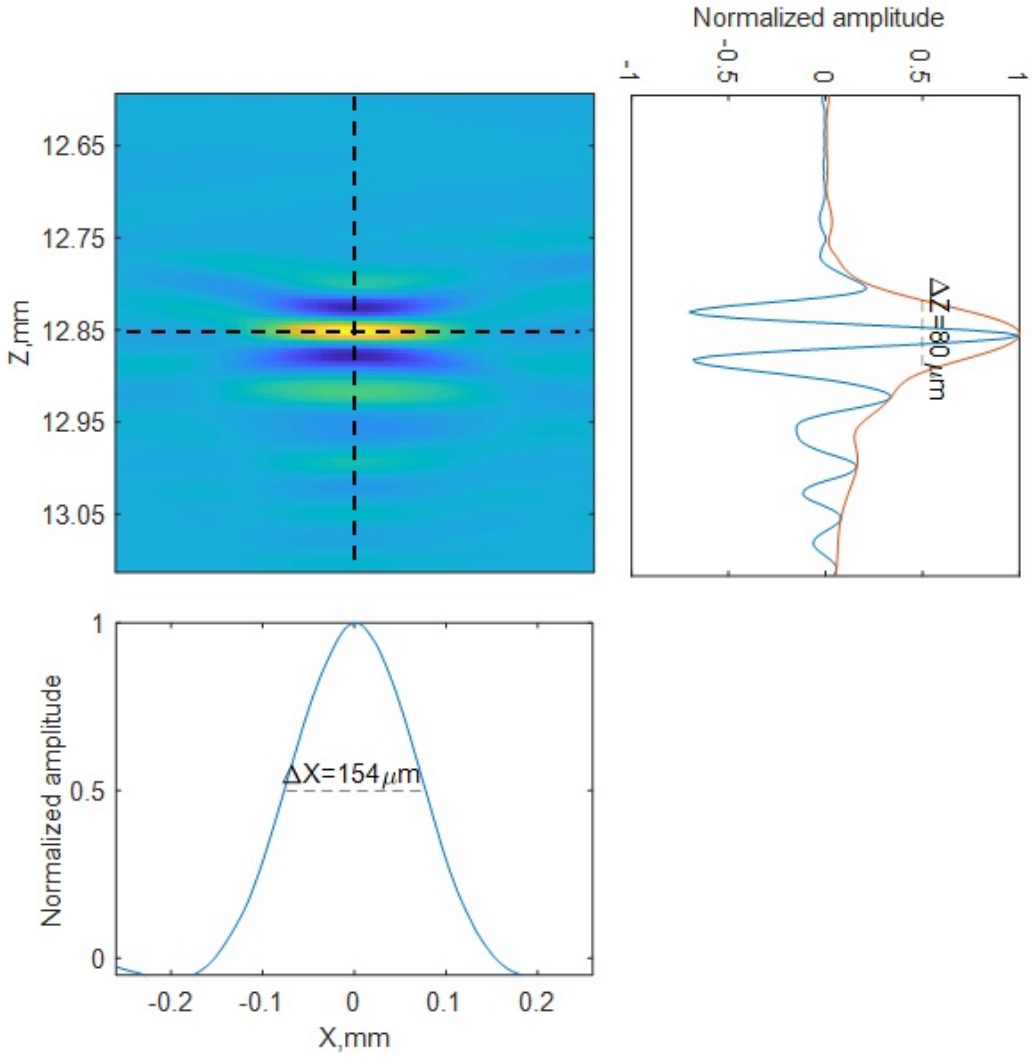

Fig. 2.9 US PSF acquired with the L22-8 US probe. The lateral dimension of the PSF, defined as the lateral FWHM of the central lobe, is about 154 μm. The axial dimension of the PSF, defined as the FWHM of the PSF envelope along the Z axis, is about 80 μm.

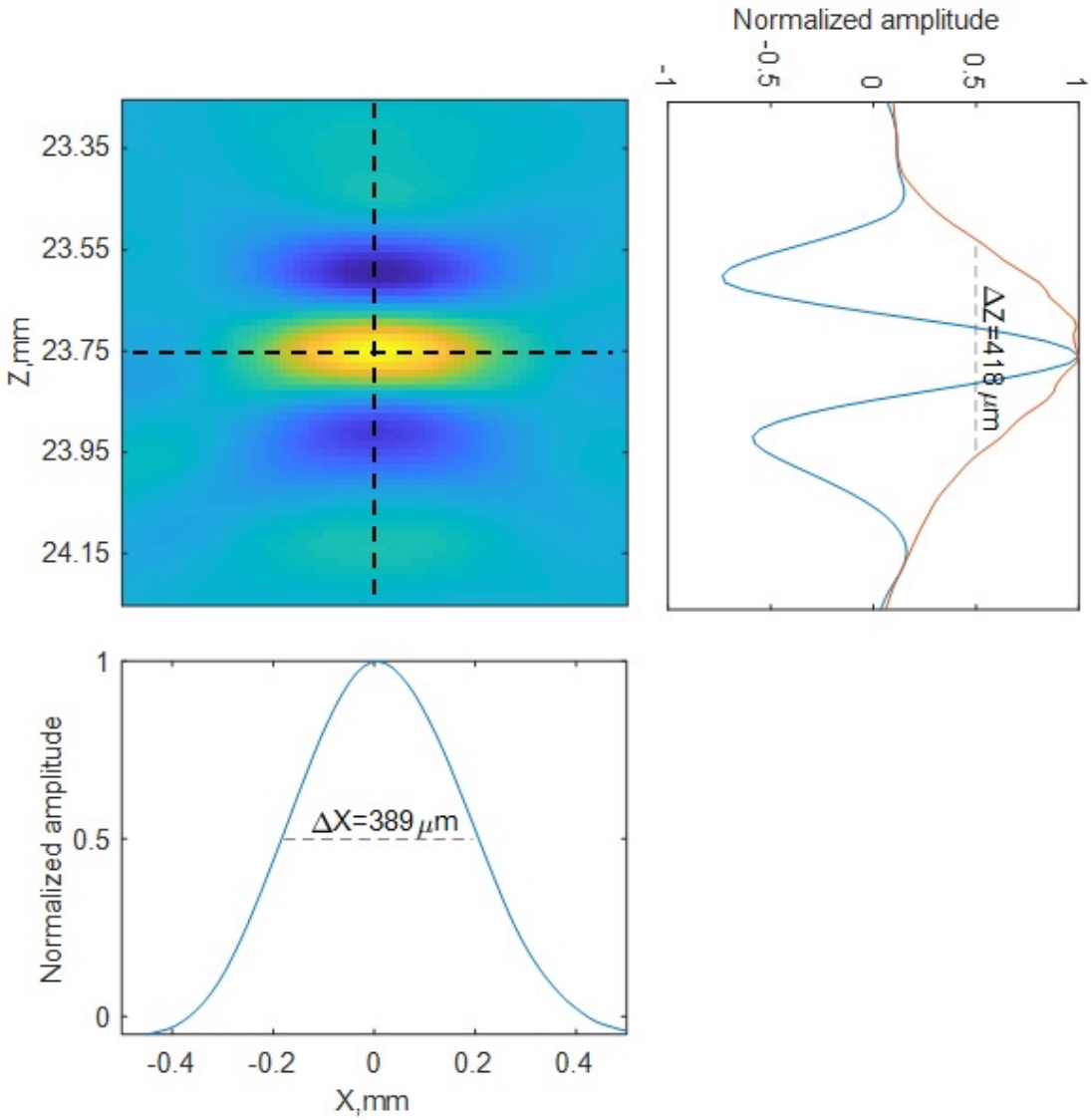

Fig. 2.10 PA PSF acquired with the L7-4 US probe. The lateral dimension of the PSF, defined as the lateral FWHM of the central lobe, is about 389 μm. The axial dimension of the PSF, defined as the FWHM of the PSF envelope along the Z axis, is about 418 μm.

2.6 Microfluidic circuits

In Chapters 3-6 our experiments are based on microfluidic samples. These samples are prepared using polydimethylsiloxane (PDMS) with a standard soft-lithography manufacturing technology [Tang and Whitesides, 2010]. Each sample has a structure to image sandwiched between two layers of PDMS. The thickness of the upper layer (the layer to be placed closer to the US probe) is around 180 μm.

The geometry of the samples is detailed in Fig. 2.11a,c. A photo of one of the samples filled with absorbing liquid is shown in Fig. 2.11b. For cross-sectional imaging, we use the central part of the circuit, containing either five parallel microchannels (Fig. 2.11a,b) or two approaching channels (Fig. 2.11c). Apart from the structure to image, the microfluidic circuit contains other important elements, such as randomizers and dust filters. These elements play a great role in experiments with 10 μm microbeads or red blood cells. The randomizers are loops with a short branch and a long one. A microbead going into one branch or the other, the microbeads flow is scrambled. As a result, the distribution of microbeads in different channels is not correlated in time. The dust filters are stacks of pillars separated by 30 μm. These pillars are necessary to avoid large pieces of dust blocking the flow inside the circuit.

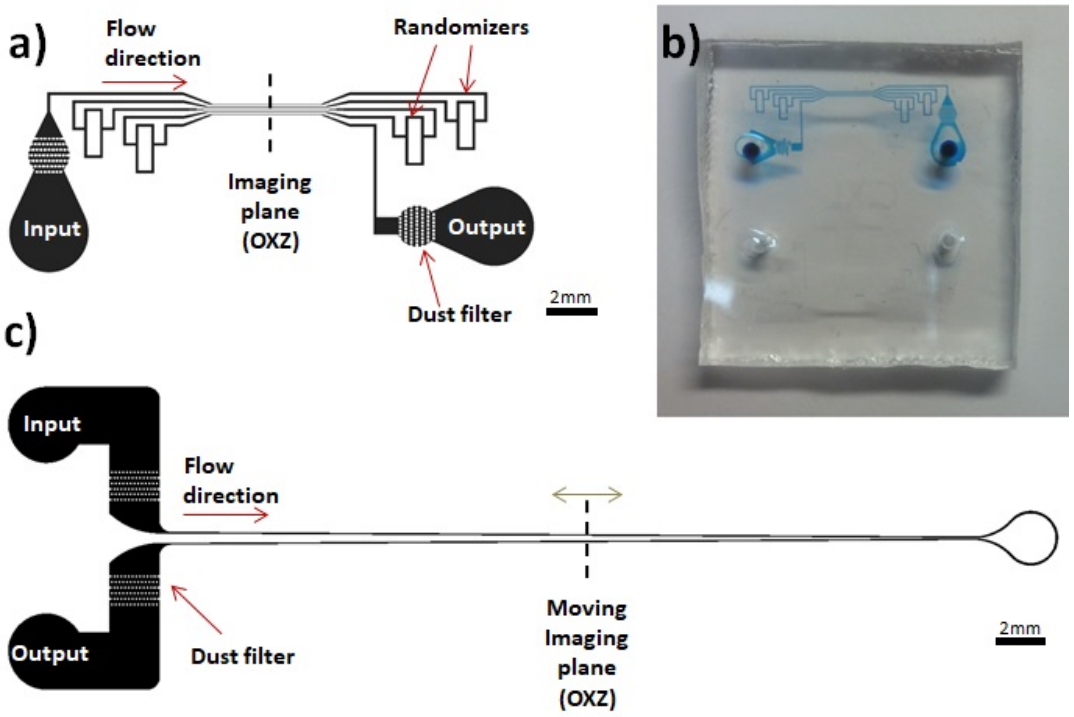

Fig. 2.11 (a,c) Overview of the microfluidic circuit, showing various circuit elements (input and output ports, dust filters, and randomizers). The imaging plane crosses five parallel channels (a) or two approaching channels (c). (b) Photo of a sample with the pattern shown in (a).

For the pattern with five parallel microchannels (Fig. 2.11a), numerous samples

have been fabricated with different center-to-center interchannel distances L_{cc} = 180 μm, 125 μm, 75 μm. The channel width is $w_{ch} = 20\ \mu m$ for $L_{cc} = 75\ \mu m$ and $w_{ch} = 40\ \mu m$ in all other cases. For the pattern with two approaching microchannels (Fig. 2.11c), the interchannel distance varies between and 180 μm and 80 μm. The channel width is $w_{ch} = 40\ \mu m$. For both patterns, the channel height is $h_{ch} = 50\ \mu m$. Notably, the minimum interchannel distance $L_{cc} = 75\ \mu m$ and the minimum channel width $w_{ch} = 20\ \mu m$ are determined by technological limitations.

When microfluidic samples are used in US or PA experiments, the imaged structure built in a PDMS block is usually covered by a glass plate through which imaging is done. However, in our experiments imaging was performed through a 180 μm-thick PDMS layer glued to the PDMS block carrying the imaged structure. The reason is that only a small portion of the incident acoustic energy penetrates the glass plate as the physical properties of glass (mass density $\rho \approx 5000\ kg/m^3$, speed of sound $v_s \approx$ 4540 m/s) are far from those of water (mass density $\rho \approx 1053\ kg/m^3$, speed of sound $v_s \approx 1500$ m/s). However, the physical properties of PDMS are closer (mass density $\rho \approx 969\ kg/m^3$, speed of sound $v_s \approx 1000$ m/s [Rahman et al., 2012]) to those of water. As a result, reflections at the PDMS/water interface can almost be avoided. The disadvantages of imaging through PDMS include significant acoustic attenuation and abberations when the PDMS layer is thick.

In this PhD study, whatever reconstruction method is used, we neglect presence of the 180 μm-thick PDMS layer covering the channels. In particular, we assume the homogeneous speed of sound v_s = 1500 m/s (corresponding to the speed of sound in water at 20°C) everywhere in the propagation medium.

CHAPTER 3

Localization-based super-resolution imaging

3.1 Principles of localization-based super-resolution imaging

Localization-based imaging techniques rely on the possibility with a diffraction-limited imaging system to determine the position of a point source with a precision much better than the size of the point spread function (PSF) provided that PSFs corresponding to different sources are separated in some parameter space [Betzig, 1995]. In this Chapter, we describe principles of optical super-resolution localization-based imaging, that were also used to obtain super-resolution in ultrasound imaging, and then apply these principles to demonstrate super-resolution in photoacoustics.

3.1.1 Localization-based super-resolution in optics

Localization-based techniques were first proposed to overcome the diffraction limit in optical imaging. In particular, in the methods named PALM [Betzig et al., 2006], FPALM [Hess et al., 2006] and STORM [Rust et al., 2006] super-resolution is achieved by detecting distinguishable sources on different sparse subsets of fluorescent molecules. Fig. 3.1 illustrates the resolution improvement provided by PALM. If conventional fluorescence imaging provides resolution of several hundred nanometers, localization-based methods lead to resolution ranging from a few to tens of nanometers.

The idea of localization-based fluorescence imaging is to separate the photons emitted by one fluorophore from those emitted by the others. Contrary to standard fluorescence imaging, in localization-based methods all the fluorescent particles do not emit at the same time. Conversely, random sparse subsets of fluorophores are activated at different time moments by a specific illumination wavelength. Each subset leads to a diffraction-limited image, but the concentration of sources in the subset is weak enough for the centers of individual PSFs to be detected. The super-resolved image is then obtained as a histogram of the fluorophore positions detected for each subset. To avoid accumulation of active fluorophores in the sample, which would eventually lead to a diffraction-limited resolution, spontaneously occurring photobleaching (a phenomenon that makes fluorophores irreversibly inactive) is used in PALM, while reversible switch-

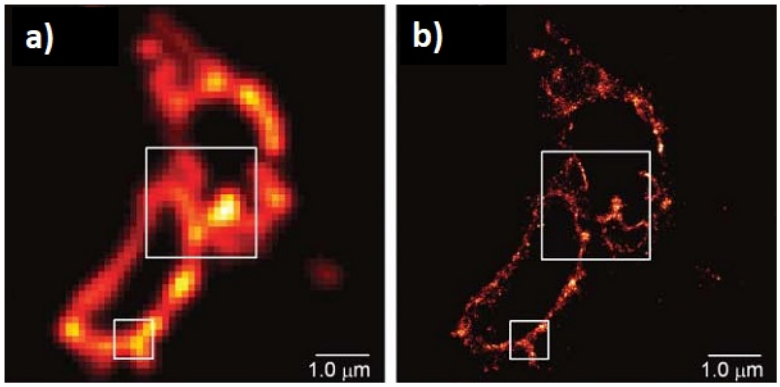

Fig. 3.1 (a) Comparative summed-molecule total internal reflection fluorescence (TIRF) (a) and PALM (b) images of the same region within acryoprepared thin section from a COS-7 cell expressing the lysosomal transmembrane protein CD63 tagged with the PA-FP Kaede [Betzig et al., 2006].

ing between active and inactive fluorescent states is exploited in STORM.

In every diffraction-limited image the coordinates of each isolated PSF are determined by fitting the measured emission profile to a known function, which is usually a Gaussian function in two dimensions. It can be shown [Betzig et al., 2006] that the fitting error σ_f depends on the number of collected photons N_p as $\sigma_f \sim 1/\sqrt{N_p}$. Super-resolution can be achieved if this error is much smaller than the size of the PSF. So, a certain number of photons from each fluorophore should be detected. In addition, to reconstruct the entire imaged structure, many fluorophores residing in different parts of the sample should be localized. Thus, localization-based imaging consists in many cycles involving activation and deactivation of different fluorescence molecules. In PALM, at typical frame rates of 0.5 s to 1.0 s, between 2 and 12 hours are required to get a single super-resolved image based on $\sim 10^5$ localized molecules [Betzig et al., 2006].

3.1.2 Localization-based super-resolution in ultrasound imaging

Underlying ideas of optical localization methods were subsequently applied to demonstrate super-resolution in ultrasound (US) imaging [Desailly et al., 2013; Viessmann et al., 2013; OReilly and Hynynen, 2013; Errico et al., 2015; Christensen-Jeffries et al., 2015; Luke et al., 2016]. As in optics, having sparse distribution of active sources is crucial for US super-localization imaging. In ultrasound, such individual sources are based on microbubbles flowing inside the imaged structure. This flow results in a random distribution of microbubbles in the imaging zone at any given moment. By accumulating the positions of microbubbles detected at each acquisition, a super-resolved image can be constructed.

In first proof-of-concept US experiments, tube-like phantoms were reconstructed

by localizing microbubbles flowing through the samples [Viessmann et al., 2013; OReilly and Hynynen, 2013]. However, to achieve the required sparsity of sources, the microbubbles had to be induced at a very low concentration. To overcome this limitation, Desailly and colleagues suggested sono-activated contrast agents and used them to reconstruct the sub-wavelength structure of a microfluidic circuit [Desailly et al., 2013]. The width of the microfluidic channels reconstructed using localization was 13 times smaller compared to conventional US imaging (Fig. 3.2b,c). In sono-activated localization microscopy contrast agents do not have to be present at an extremely low concentration as they can be randomly and sparsely activated at appropriate transmit US pressure. As a result, there is always at least one microbubble in the imaging zone and fewer US acquisitions are needed to reconstruct the object. This pioneering study triggered many subsequent works [Errico et al., 2015; Christensen-Jeffries et al., 2015; Luke et al., 2016], including the *in vivo* demonstration of US localization microscopy for super-resolution vascular imaging in rodent brain [Errico et al., 2015] with the thinnest reconstructed blood vessel being 10 times smaller than the acoustic wavelength.

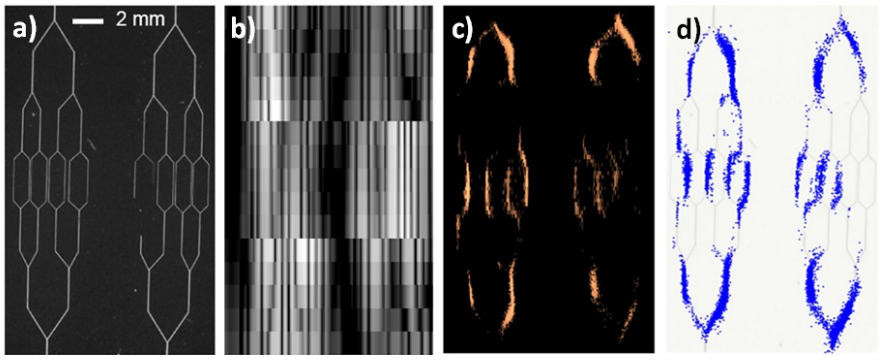

Fig. 3.2 Comparison between fluorescence microscopy (a), standard US imaging (b), US super-localization (c), and the localization imaged superimposed with optical image (d). The width of the microfluidic channels reconstructed using localization is 13 times smaller compared to conventional US imaging [Desailly et al., 2013].

3.1.3 Motivation for localization-based photoacoustic imaging

In photoacoustic (PA) imaging, overcoming the acoustic diffraction limit by localization was first proposed by Iskander-Rizk and colleagues [Iskander-Rizk et al., 2017] who used the difference between the absorption spectra of two unresolved absorbers to separate and then localize the targets. Although sources separated by 1/20 of the PSF width were resolved, this approach was limited to imaging only two spectrally distinct absorbers within each PSF.

Here, in a PA proof-of-principle experiment, we demonstrate that localizating optical absorbers (small microbeads) flowing through a microfluidic sample permits recon-

structing the sub-diffraction structure of the object in 2D cross-sectional imaging. In our demonstration, PA localization makes use of a low concentration of sources which permits distinguishing signals from different absorbers at any particular moment. At any time the distribution of absorbers inside the imaged structure is different, so with multiple PA acquisitions signals from all parts of the object can be obtained. By constructing a histogram of the positions localized on many PA images, we can build the eventual super-resolved image of the whole object.

Although we performed localization-based imaging of samples with different interchannel distances (L_{cc} = 180 μm, 125 μm, 75 μm), here we provide the results for the smallest interchannel separation L_{cc} = 75 μm as the finest structure that could be manufactured using the adopted microfluidic technology (see section 2.6).

3.2 From photoacoustic RF signals to localization images

3.2.1 Localization in the RF-space vs localization in the BF-space

Localization-based imaging relies on the possibility to determine the coordinates of an isolated source with a precision much better than the size of its PSF. We shall now propose two methods to localize PA sources under the assumption that there is only one source in the imaging zone at the moment of the PA acquisition.

As stated in section 1.3.4.2, the data available at the output of the acquisition machine is a radio-frequency (RF) frame, containing the signals acquired by all transducer elements. The detected PA response results in a curved space-time trajectory on this frame, determined by the arrival times of the PA signal on different transducer elements. The coordinates of the source can then be found by using this curve. Alternatively, the RF frame can be beamformed to obtain the PSF in the beamforming space (object space, or BF-space) XZ. In this case, the coordinates of the source can be determined based on this PSF.

Fig. 3.3 illustrates localization of a single source in the RF- and the BF-space. To localize the source in the RF-space, the theoretical model based on time delays is fitted to the experimental trajectory, derived from measuring time delays. The experimental curve is built by looking for the maxima of the signals received by each transducer element. For each column k, ($k = 1..N_{el}$) of the RF frame, the position of the detected maximum is associated with the arrival time t_k corresponding to the transducer element placed at $\{x_k, z_k\}$. Here, we consider a linear transducer array, for which all N_{el} elements are arranged in a single row and $z_k = 0$, $k = 1..N_{el}$. Outliers on the experimental curve $t_k(x_k)$, that may appear due to the presence of noise, are excluded using a three point median filter. Then, the source coordinates $\{x_s, z_s\}$ are established with the least squares 2nd order polynomial fitting based on the theoretical model predicted by time

delay laws:

$$(t_k(x_k) + t_0)^2 = \frac{1}{v_s^2}[(x_k - x_s)^2 + (z_k - z_s)^2]. \tag{3.1}$$

As stated above, we impose $z_k = 0$ in Eq. (3.1).

To apply model (3.1) we suppose v_s = 1500 m/s for the speed of sound in water and we take the value of t_0 that provides the maximal intensity on the conventional reconstruction image for one microbead.

It follows from Eq. (3.1) that $y_k = (t_k(x_k) + t_0)^2 v_s^2$ is a 2nd order polynomial of x_k: $y_k = p_1 x_k^2 + p_2 x_k + p_3$, where the coefficients p_1, p_2, p_3 depend on the source position $\{x_s, z_s\}$. We measure the coefficients p_1, p_2, p_3 by fitting the experimental curve $y_k(x_k)$ to the theoretical one predicted by model (3.1). Then, the source coordinates $\{x_s, z_s\}$ are estimated as $x_s = -0.5p_2$, $z_s = \sqrt{p_3 - x_s^2}$.

To localize the source in the BF-space, the maximum of the beamforming PSF is identified. Then, the position of this maximum is refined by applying the 2nd order polynomial fitting to a number of neighbouring points on the beamforming grid. The source coordinates $\{x_s, z_s\}$ are then associated with the refined position of the maximum.

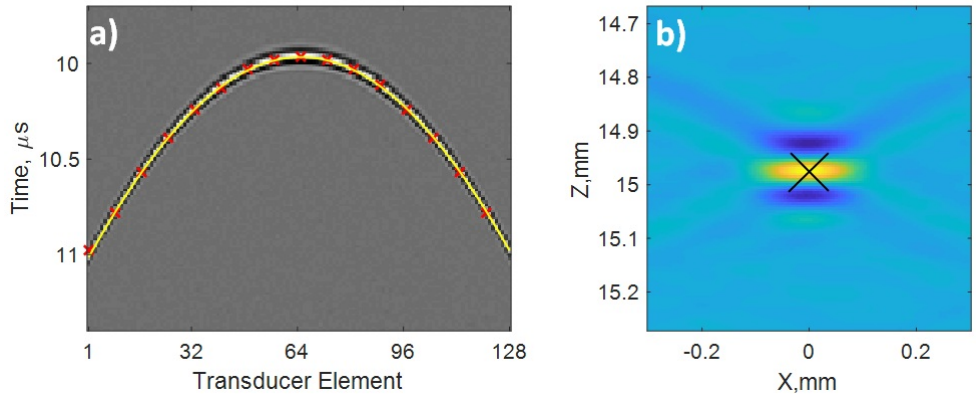

Fig. 3.3 (a) Localization in the RF space (t_0 = 9.67 μs). The coordinates of the source are determined by fitting the theoretical curve (yellow) to the experimental one (red crosses). (b) Localization in the BF-space. The coordinates of the source are associated with the maximum of the PSF (the black cross).

To determine whether localization is more precise in the BF-space or RF-space, we carried out numerical simulations. In simulations, the same source was localized many times at different levels of the signal to noise ratio (SNR). The SNR was defined in the RF-space as the ratio between the maximum of the modelled RF signal from the source and the standard deviation of the added gaussian noise.

Fig. 3.4 shows the standard deviation for localization in the lateral X and the axial Z directions computed for different SNR. It can be clearly seen that for a small SNR

detecting the maximum in the BF-space provides a better precision than fitting the curve in the RF-space. The reason is that beamforming increases the SNR thanks to coherent summation of signals and incoherent summation of noise. So, the single maximum in the beamformed image can be detected more precisely than the N_{el} maxima on the RF frame. For a large SNR localization can provide an acceptable precision (significantly below the full width at half maximum (FWHM) of the PSF) whichever approach is used.

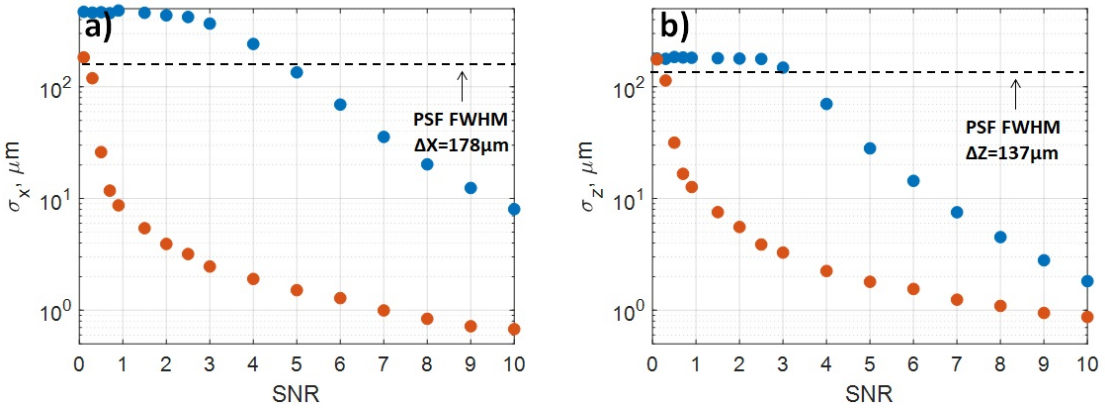

Fig. 3.4 Standard deviation of localized positions in the lateral (a) and axial (b) directions, estimated for different SNR in the BF-space (red dots) and the RF-space (blue dots). The dashed line denotes the PSF FWHM in the lateral (a) and axial (b) directions.

3.2.2 Choice of the localization method in the BF-space

As follows from Fig. 3.4, the localization error increases significantly for low values of the SNR. To improve the detection precision when the SNR is small, the matched filter approach can be used. The principle of this approach is illustrated in Fig. 3.5. While the initial beamformed image appears noisy, correlation with the PSF lifts up microbead signals that are different from those produced by electronic noise. The 2D correlation image X_C is obtained with the following equation:

$$X_C(n,l) = \frac{\sum_{i=1}^{N}\sum_{j=1}^{M} X_{BF}(i,j)\cdot X_{ref}(i-n,j-l)}{\sum_{i=1}^{N}\sum_{j=1}^{M} X_{ref}^2(i,j)}, \tag{3.2}$$

where X_{BF} is the beamformed image and X_{ref} is the reference PSF.

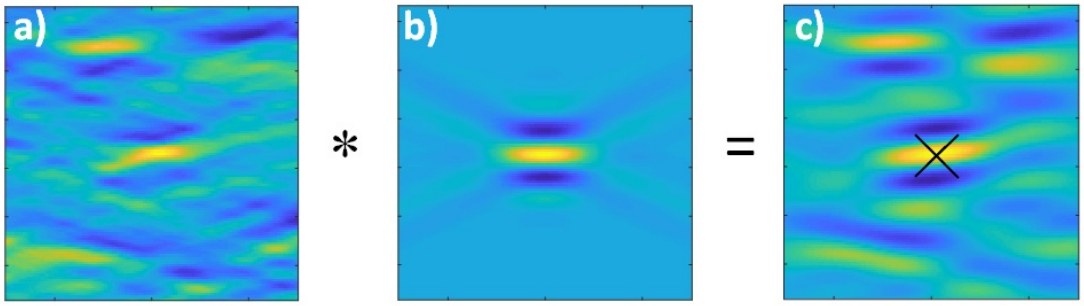

Fig. 3.5 Matched filter approach for denoising. Correlation of the initial beamformed image (a) with the known PSF (b) improves the apparent SNR (c). The black cross in (c) shows the position of the detected maximum.

To study the effect of the matched filtered approach on the localization error, we carried out numerical simulations. As follows from Fig. 3.6 the matched filter approach indeed leads to a certain improvement in the localization precision.

3.2.3 Expected localization precision

The experimental SNR calculated for a single microbead was SNR≈1. As follows from our simulations (Fig. 3.6), when microbeads are localized in the BF-space, the expected uncertainty in the lateral direction is $\sigma_x = 5.6\ \mu m$ and $\sigma_x = 10.5\ \mu m$ with and without the matched filter correspondingly.

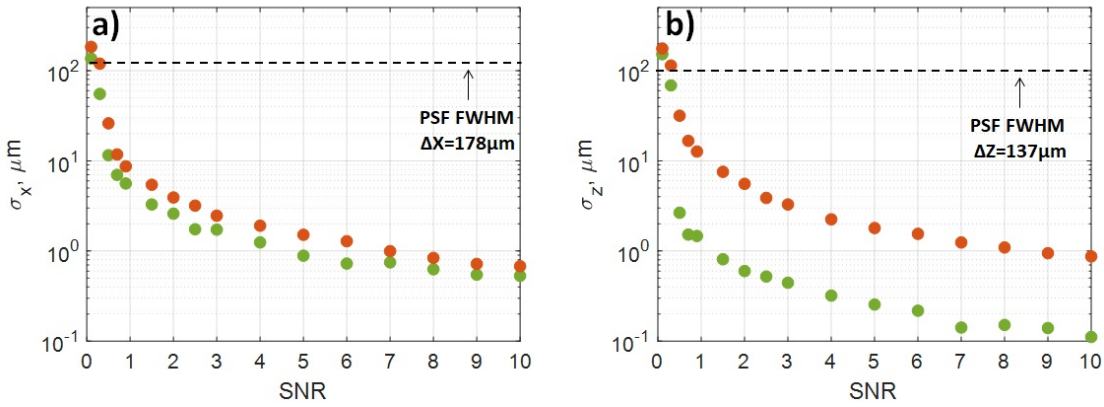

Fig. 3.6 Localization precision in the lateral (a) and axial (b) directions, estimated for different SNR in the BF-space with (green dots) and without (red dots) the matched filter method. The dashed line denotes the PSF FWHM in the lateral (a) and axial (b) directions.

3.3 Experimental demonstration

3.3.1 Samples

3.3.1.1 Microfluidic circuits

The sample to image consists of five identical parallel microfluidic channels with a rectangular cross-section (Fig. 3.7). To perform cross-sectional imaging, the microchannels are placed perpendicularly to the imaging plane XZ of a linear transducer array (type L22-8, see Chapter 2) at the US probe elevational focus distance z_f = 15 mm. In this plane, each channel is h_{ch} = 50 μm high and w_{ch} = 20 μm wide, the center-to-center distance between neighbouring channels being L_{cc} = 75 μm. For more details on fabrication of the microfluidic sample the reader is referred to Chapter 2.

Fig. 3.8 shows a schematic view of the imaged cross-section and the result of standard PA imaging of the channels filled with absorbing liquid. Importantly, Fig. 3.8b confirms that the resolution of conventional PA imaging is too coarse to recover the structure of the circuit.

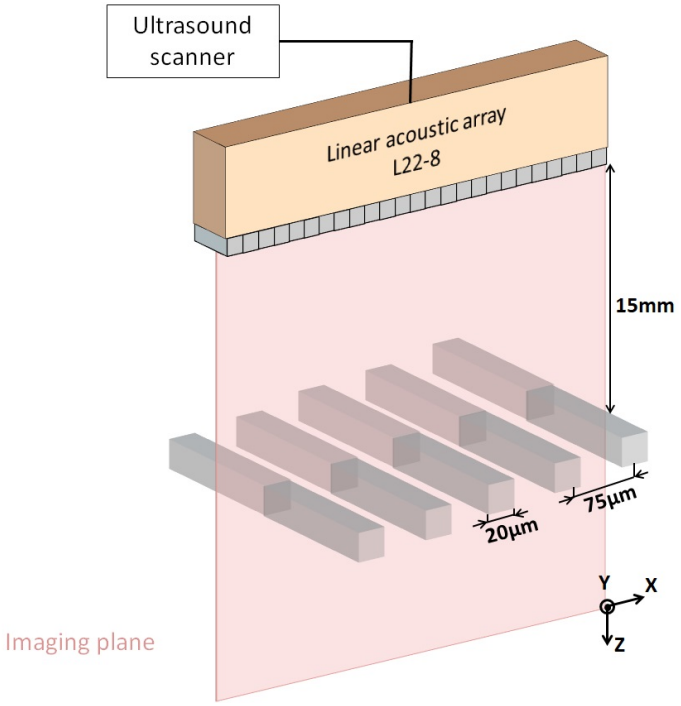

Fig. 3.7 A microfluidic sample consisting of five parallel microchannels is placed perpendicularly to the imaging plane XZ of the linear transducer array at the US probe elevation focus distance z_f = 15 mm. In this plane, each channel is h_{ch} = 50 μm high and w_{ch} = 20 μm wide, the center-to-center distance between neighbouring channels being L_{cc} = 75 μm.

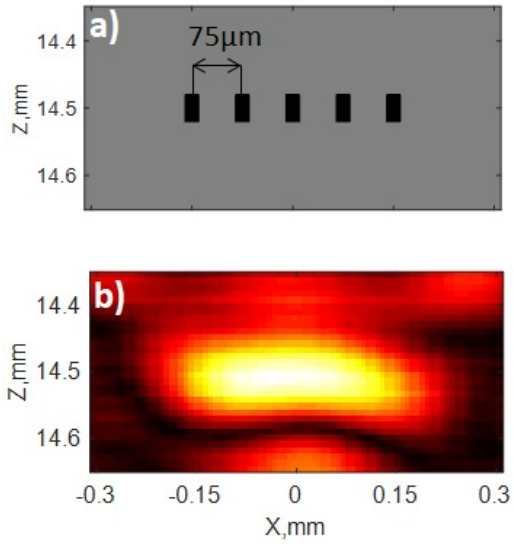

Fig. 3.8 A schematic view of the imaged cross-sections (a) and the standard PA reconstruction image (b).

3.3.1.2 Absorbers

The super-resolved image was obtained by localizing $D_a = 10$ μm diameter spherical microbeads flowing through the microfluidic sample. The concentration of microbeads

in the circuit was set such that there was statistically $< N >$ = 1 microbead in the imaging plane at each laser shot. The average number of microbeads in the imaging plane is given by $< N >= \eta V/V_0$, with η being the volume fraction of microbeads in the suspension, V the volume of the intersection between the sample and the imaging zone, V_0 the volume of a single microbead. The volume of the imaged part of the object is $V = w_{ch} \times h_{ch} \times \Delta Y \times N_{channels}$, where w_{ch} is the channel width, h_{ch} is the channel height, $\Delta Y \approx 1$ mm is the size of the elevational focus of the US probe (see section 2.5). So, to get $< N >$ = 1 microbead in the imaging plane the volume fraction of microbeads in the suspension was set to be $\eta = 6 \times 10^{-5}$.

The suspension of microbeads was prepared according to the following recipe: 0.1% of the initial 5% w/v microbeads water suspension (Microparticles GmbH, Berlin, Germany), 0.025% of a buffer solution (TWEEN20, Sigma-Aldrich Corp., St. Louis, MO, USA), 19.6% of a density gradient medium (OptiPrep, ProteoGenix SAS, Schiltigheim, France), and 80.3% of water. The buffer solution was used to avoid microbeads sticking to each other whereas the density gradient medium was added to prevent microbeads from precipitating and getting stuck inside the pump system.

3.3.2 Measurement protocol

A schematic of the experimental setup is shown in Fig. 2.1. The suspension of microbeads was flown through the microfluidic circuit by use of a syringe pump providing a constant volumetric flow rate, corresponding to about 10 cm/s in the microchannels to image. At each laser shot ($\lambda_{laser} = 532\ nm$, PRR = 100 Hz), PA signals from the microbeads in the imaging plane were recorded by a linear transducer array (type L22-8). For further details about the acquisition equipment the reader is referred to Chapter 2. In total, 20,000 PA frames were acquired, resulting in a total experiment time of T_{exp} = 3 min.

The experimental SNR calculated as the ratio between the maximum of the single-exposure RF signal corresponding to one microbead and the standard deviation of electronic noise calculated over a signal-free region of the RF data was SNR≈1. Among the many factors contributing to this value of the SNR, the most significant are the laser fluence, the absorption spectrum of the bead, and the sensitivity of the transducer array. These parameters affect the amplitude of PA signals while the noise is dictated by the acquisition electronics only. The relatively low laser fluence $3mJ/cm^2$ was chosen as a realistic value for clinical applications. Although according to the safety norms [NE, 2000] for $\lambda_{laser} = 532\ nm$ and $\tau_p = 5\ ns$ the maximal fluence at the skin surface is 20 mJ/cm^2, the real intensity at the imaging depth will be smaller due to blood absorp-

tion. In practice, the SNR could be potentially increased by using sources with a more significant absorption at the laser wavelength λ_{laser}.

In addition to the localization experiment, we obtained the PSF of the imaging system. This PSF was necessary to localize microbeads with the matched filter approach. To do so, a sample with only one microfluidic channel was perfused with the suspension of microbeads at a very slow flow rate. When a microbead appeared in the channel, the corresponding PA signal was acquired and used to obtain the beamforming PSF. The measured PSF FWHM was about ΔX = 178 μm and ΔZ = 137 μm.

To perform localization-based reconstruction we first had to identify microbead signatures in the acquired PA data. This was done separately by using beamformed images and correlation images (matched-filter approach). In the beamforming operation, we assumed a homogeneous speed of sound v_s = 1500 m/s, neglecting the thin (180 μm-thick) polydimethylsiloxane (PDMS) layer covering the channels (see section 2.6). The beamforming grid step was 10 μm. To be distinguishable in a diffraction-limited image, sources at the same depth must be separated by at least the lateral FWHM of the PSF ($\Delta X = 178\ \mu m$). As the microfluidic channels were separated by $L_{cc} = 75$ μm, in each image at most two beads could be detected. So, potential microbead traces were identified by looking for the 1st and the 2nd order maxima in each image. When the 1st order maximum was identified, all surrounding pixels with amplitude greater than 50% the amplitude of the detected maximum were cut out from the image. The second order maximum was then localized. The detected position of each maximum was then refined. To do so, we applied 2nd order polynomial fitting to points adjacent to the localized maximum on the coarse beamforming grid. Afterwards, to discard false detection events resulting from noise and images with no microbeads, all detected maxima below an empirically determined threshold were discarded. Finally, the localization image was built as a probability map by computing and smoothing a 2D histogram of the detected maxima positions. The histogram was constructed on a grid with a bin size of $dx \times dz$ = 5 μm x 5 μm. Then, the histogram was smoothed out by a 2D gaussian filter with the kernel size σ_g = 10 μm to compensate for the spatial heterogeneity of the localization events.

3.3.3 Typical RF signals from a single bead

Fig. 3.9 illustrates typical PA signals for a single microbead. As seen from Fig. 3.9a,b the microbead signals are completely masked by noise. This falls in line with the low value of the experimental SNR≈1. However, beamforming makes the microbead visible (Fig. 3.9c,d) as it increases the effective SNR due to coherent summation of signals

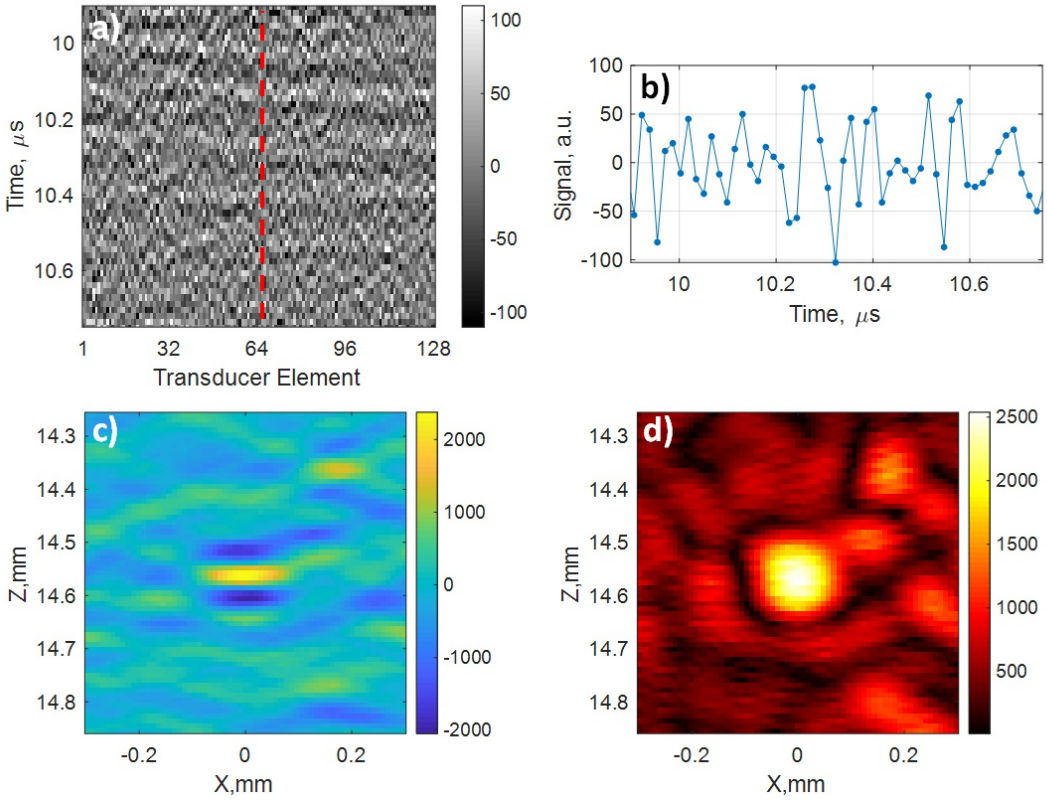

Fig. 3.9 Typical PA signals of one microbead. (a) RF frame. (b) Signal on the 64th transducer element (dashed line in (a)). (c) Bipolar PSF. (d) Envelope PSF.

and incoherent summation of noise in the RF frame.

3.4 Results

The experimental results are summarized in Fig. 3.10. As shown in Fig. 3.10a, after standard beamforming reconstruction the five microchannels appear indistinguishable. In contrast to the conventional reconstruction, the localization approach provides super-resolved images with five well separated regions (Fig. 3.10b-g). These localization images were obtained using the initial set of 20,000 beamformed images. The number of detected microbeads was 695 and 693 for localization applied to the beamformed images and correlation images correspondingly. The five cross-sections corresponding to 100 pixels on the 10 μm beamforming grid, on average about 7 localization events per pixel were detected. As follows from Fig. 3.10h, both source detection methods (on beamforming and correlation images) provide a very similar resolution improvement with the average channel-to-channel distance, estimated from the peaks centers, being close to its true value of 75 μm. Estimating the channel width from the FWHM on the localization images provides values ranging from 18 to 25 μm, close to the expected value of w_{ch} = 20 μm.

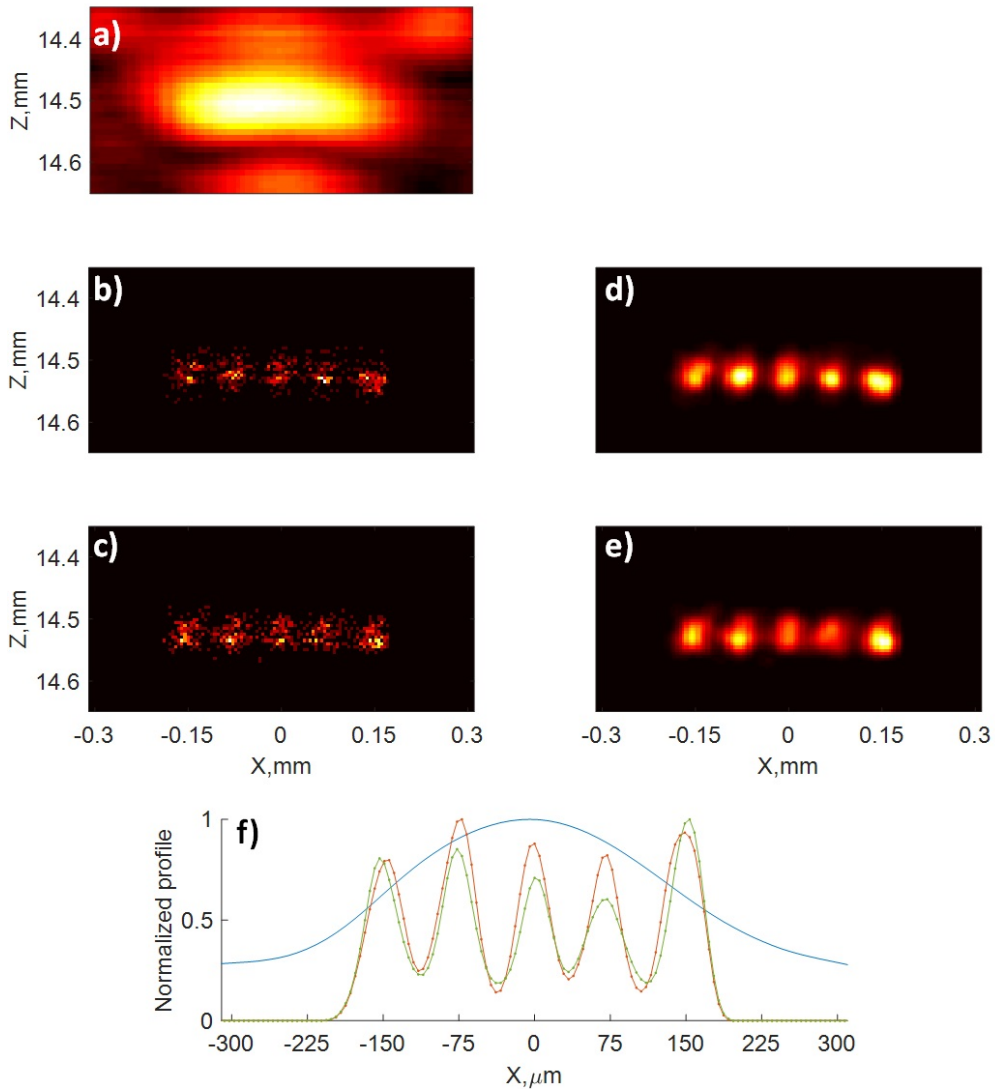

Fig. 3.10 Experimental results, SNR≈1. (a) Conventional cross-sectional PA image of the five channels. (b,c) Raw histograms resulting from localization on: (b) - beamformed images, (c) - correlation images. (d,e) Images obtained by spatially smoothing the raw histograms (b-c) with a σ_g = 10 μm 2D gaussian filter. (f) Transverse profiles at z = 14.55 mm, corresponding to images: (a) - blue, (d) - red, (e) - green.

To test whether the matched filter approach can improve the localization quality when the SNR is even smaller than the experimental value of 1, we artificially reduce the initial SNR by a factor 2.5 by adding gaussian noise to the acquired RF data. The reconstruction images are shown in Fig. 3.11. To obtain an acceptable reconstruction, we had to increase the threshold for each source detection method. As a result, the number of detected microbeads dropped to 318 for localization on beamformed images and correlation images. While the number of localization events is the same for both methods, identifying sources on beamformed images results into reconstruction of a significantly lower quality compared to the matched filter approach.

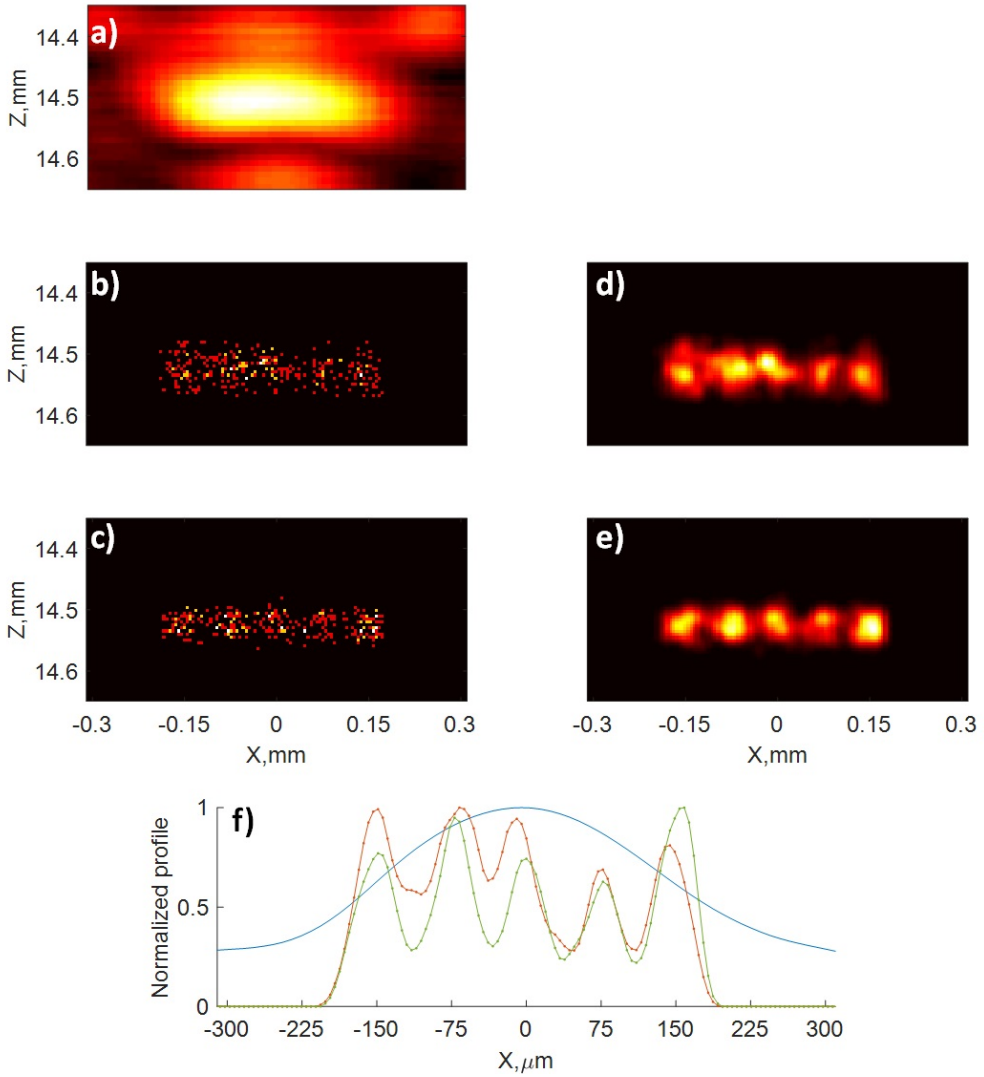

Fig. 3.11 Reconstruction results with added noise, SNR≈0.4. (a) Conventional cross-sectional PA image of the five channels. (b,c) Raw histograms resulting from localization on: (b) - beamformed images, (c) - correlation images. (d,e) Images obtained by spatially smoothing the raw histograms (b-c) with a σ_g = 10 μm 2D gaussian filter. (f) Transverse profiles at z = 14.55 mm, corresponding to images: (a) - blue, (d) - red, (e) - green.

3.5 Conclusion

The inability to reconstruct the object with standard beamforming complies with the diffraction theory as, by construction, the center-to-center distance between neighbouring channels (L_{cc} = 75 μm) is well below the classical resolution limit defined by the lateral FWHM of the PSF which was estimated to be $\Delta X = 178\ \mu m$.

As expected, the localization approach provides a super-resolved image of the object. Not only the center-to-center distance is correctly reproduced but also the channel width. In fact, the presence of noise leads to overestimation of the channel width ($\sigma_x = 5.6\ \mu m$ and $\sigma_x = 10.5\ \mu m$ for localization on beamforming and correlation im-

ages correspondingly, see section 3.2.3). Then, using the gaussian filter with the kernel size of $\sigma_g = 10\ \mu m$ increases the channel width further. However, the finite microbeads diameter ($D_a = 10\ \mu m$) leads to a distribution of particles positions which is 10 μm narrower than the channel width (w_{ch} = 20 μm). In addition, the apparent channel width is also related to the flow structure that dictates the probability of detecting a microbead at a given position. So, the observed good quantitative agreement might well be a matter of coincidence.

As concerns localization on beamformed and correlation images, the two techniques showed very similar performance for the initial dataset because the initial SNR was relatively high. However, when the SNR was reduced by adding noise to the initial data, the matched filter approach outperformed localization on beamformed images. The reason is that the matched filter permits detecting microbeads by enhancing the image features that result from microbead signatures (i.e. PSFs) rather than from electronic noise of the system. When the SNR is small, relevant signals have the same amplitude as noise and the matched filter permits distinguishing them.

In our experiment, the total acquisition time required to reconstruct the 5 channels was about 3 minutes. This indicates that PA localization imaging, like US localization imaging [Couture et al., 2018; Hingot et al., 2019], suffers from a low temporal resolution. A long imaging time in PA and US super-localization results from the requirement for a low concentration of localization sources and a high number of localization events required to reconstruct the imaged structure. Increasing the concentration may reduce the imaging time, but separating different sources on each acquired image will be more challenging. A classical approach consists in detecting sources by identifying them on beamformed images [Viessmann et al., 2013; OReilly and Hynynen, 2013; Siepmann et al., 2011] or RF frames [Desailly et al., 2013]. As has been demonstrated here, when the SNR is small, the matched filter can be efficiently used to distinguish relevant signals from noise. However, to be separable from one another the sources must be by more than a PSF apart since RF data and beamformed images are diffraction-limited. In the case of higher concentrations, sources are closer and single images are to be super-resolved. Such super-resolved images can be obtained, for example, through sparsity-based reconstruction [Shu et al., 2018]. Additionally, a recent study [van Sloun et al., 2018] showed that the deep learning framework can be employed to improve US localization at high microbubble concentrations.

Regarding the number of localization events, in biomedical imaging each blood vessel requires several localization events to be reconstructed, the number of localization events increasing with the amount of super-resolved pixels that the vessel encom-

passes [Couture et al., 2018; Hingot et al., 2019]. It is to be noted that due to a viscous movement, the probability of a localization event is distributed non-uniformly across the vessel, so longer acquisition time is needed to collect enough data to reconstruct the vessel at its borders than to reconstruct the vessel central part. For example, in our experiment, the centers of the microfluidic channels became distinguishable after processing 1/3 of the acquired images. While it can be viewed as an obstacle to localization imaging, the non-uniform probability of localization events carries some additional information. In this regard, it has been pointed out that localization statistics can be used to infer information about the flow, including the flow profile and the flow rate [Hingot et al., 2019].

In this chapter, we showed that localization of flowing optical absorbers can lead to super-resolution in PA imaging. Although here the demonstration of super-resolution was limited by the smallest features that could be fabricated using the adopted technology (channels of $w_{ch} = 20\ \mu m$ separated by $L_{cc} = 75\ \mu m$), much closer objects can in principle be resolved in super-localization. It should be noted, however, that absorbers must physically be able to circulate in the imaged structure.

It is to be noted that in parallel to our work, another group turned out to be also exploring the localization approach in PA imaging [Dean-Ben and Razansky, 2018]. By obtaining a super-resolved image of a 220 μm diameter pipette tip, it was shown that PA super-localization can be performed in three dimensions. Here, by using more elaborate samples we managed to demonstrate that smaller features ($L_{cc} = 75\ \mu m$) can be resolved in cross-sectional imaging. As follows from both studies, localization-based imaging is in principle independent of the acquisition geometry and the discussion conducted in this chapter would also be relevant for 3D super-localization imaging.

Finally, the results of our work [Vilov et al., 2017] and those of Razanski *et al.* [Dean-Ben and Razansky, 2018] formed the basis for the first *in vivo* study based on PA super-localization [Zhang et al., 2019]. In particular, 3D super-resolved images of the cortical layer of the mouse brain were obtained. As contrast agents, biocompatible dyed droplets were used. It was shown that blood vessels separated down to 25 μm can be reconstructed in super-localization, with the conventional resolution limit being 150 μm.

CHAPTER 4

Super-resolution photoacoustic imaging based on flow-induced fluctuations

4.1 Principle of fluctuation-based super-resolution imaging

4.1.1 Super-resolution optical fluctuation imaging (SOFI)

Fluctuation-based super-resolution photoacoustic (PA) imaging, described in this Chapter, is inspired by the principles of super-resolution optical fluctuation imaging (SOFI) [Dertinger et al., 2009]. The SOFI approach is based on independent stochastic fluctuations of fluorescence molecules. In SOFI, a series of N diffraction-limited images is first acquired in traditional camera-based fluorescence microscopy, the pixel size in each image being smaller than the conventional resolution. The n-th order super-resolved image is then obtained as the n-th order cumulant of the original pixel time series. The n-th order cumulant involves convolution between the object structure and only the n-th order point spread function (PSF), other orders of the PSF do not interfere. As the n-th order PSF is narrower than the 1st order PSF, the nth order cumulant provides a $\sqrt{n}$ resolution increase. For n¿1 the n-th order cumulant $C_n(\overrightarrow{r})$ is calculated recursively using the previous order cumulants and moments $\mu_m(\overrightarrow{r}) = 1/N \sum_{k=1}^{N} [A_k(\overrightarrow{r})]^m$:

$$C_n(\overrightarrow{r}) = \mu_n(\overrightarrow{r}) - \sum_{k=1}^{n-1} \binom{n-1}{k-1} C_k(\overrightarrow{r}) \mu_{n-k}(\overrightarrow{r}), \tag{4.1}$$

where $A_k(\overrightarrow{r})$ is a diffraction-limited image obtained at acquisition k. Note that $C_1(\overrightarrow{r}) = \mu_1(\overrightarrow{r})$ is the mean image, and $C_2(\overrightarrow{r})$ is the variance image.

Fig. 4.1a,c shows the standard reconstruction and the second-order SOFI images of the α-tubulin network of a 3T3 fibroblast cell obtained in the first demonstration of this approach [Dertinger et al., 2009]. In addition to the resolution improvement, a certain background suppression is noticeable in the SOFI image. The reason is that the SOFI algorithm intrinsically removes uncorrelated background. The results of deconvolution applied to the standard reconstruction image and the corresponding second order SOFI

image are shown in Fig. 4.1b,d. As can be seen, the standard reconstruction image is deconvolved well, and the quality of the deconvolved image is comparable with the second-order SOFI image. However, deconvolution of the second-order SOFI image provides a better reconstruction compared to deconvolution of the mean image.

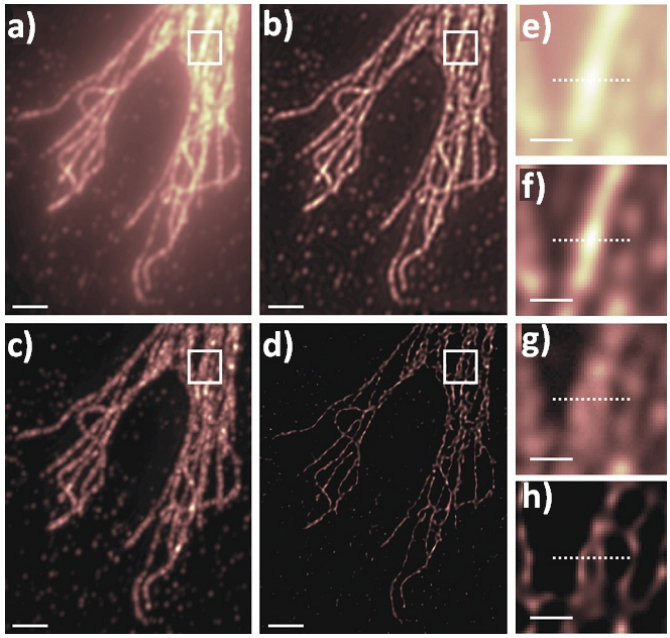

Fig. 4.1 SOFI images of cells. Wide-field image of QD625 labeled 3T3 cells [Dertinger et al., 2009]. (a) Original image generated by time averaging all frames of the acquired movie (3,000 frames, 100ms per frame). (b) The image in (a) deconvolved. (c) Second-order SOFI image. (d) The image in (c) deconvolved. (e–h) Magnified views of the boxed regions in (a)–(d). (Scale bars: (a)–(d), 2 μm; (e)–(h), 500 nm.)

4.1.2 Fluctuation-based photoacoustic imaging

Let us consider acoustic-resolution PA imaging with short pulse illumination, PA signals experiencing pulse-to-pulse fluctuations. Assuming that the PSF does not change within the imaging zone, one can consider the result of standard PA reconstruction as the convolution between the acoustic PSF $h(\overrightarrow{r})$ and the distribution of absorbed optical energy $E_k(\overrightarrow{r}) = I_k(\overrightarrow{r}) \times \alpha_k(\overrightarrow{r})$, where $I_k(\overrightarrow{r})$ is the light intensity distribution and $\alpha_k(\overrightarrow{r})$ is the distribution of optical absorption at laser shot k. As in optics, the PA resolution is limited by the size of the acoustic PSF. To achieve sub-diffractional resolution via a SOFI-like approach, one needs PA sources that would fluctuate stochastically and independently. A first approach consisted in creating intensity fluctuations $I_k(\overrightarrow{r})$ by illuminating the imaged object with a different optical speckle pattern at each laser shot k [Chaigne et al., 2016]. In that study, the 2nd order cumulant (variance) image was calculated and a resolution improvement of about $\sqrt{2}$ was reported. It should be mentioned that the variance PA image is the sum of the signal variance and the noise

variance. A major disadvantage of using optical speckle illuminations is that in deep tissues the variance signal originating from speckle fluctuations can be too weak to distinguish from the noise fluctuations (see section 1.4).

4.1.3 The proposed approach based on flow-induced fluctuations

In this chapter, we experimentally demonstrate a new super-resolution technique using fluctuations originating from moving optical absorbers rather than from optical speckles. Importantly, in our experiments red blood cells (RBCs) play the role of moving absorbers since fluctuations of RBCs are intrinsic to flows in blood vessels. Exploiting these fluctuations would therefore eliminate the need for contrast agents or additional imaging equipment in clinical setting. In the case of absorbers flowing in a static structure, the distribution of optical absorption can be expressed as

$$\alpha_k(\overrightarrow{r}) = \mu_0[f(\overrightarrow{r}) \times g_k(\overrightarrow{r})], \tag{4.2}$$

where μ_0 is the optical absorption of the material of absorbers, $g_k(\overrightarrow{r})$ is the sum of delta functions at every point source at laser shot k, and $f(\overrightarrow{r})$ is the object structure such that $f(\overrightarrow{r})$ = 1 inside the imaged object and $f(\overrightarrow{r})$ = 0 outside. PA reconstruction image A_k corresponding to laser shot k can thus be written as:

$$A_k(\overrightarrow{r}) = I(\overrightarrow{r})[\alpha_k(\overrightarrow{r}) * h(\overrightarrow{r})], \tag{4.3}$$

where $h(\overrightarrow{r})$ is the bipolar PSF in the beamforming space. As our approach is based on flow fluctuations rather that light intensity fluctuations, we shall use homogeneous illumination: $I(\overrightarrow{r}) = I_0$.

By averaging over M PA images, one obtains

$$< A_k(\overrightarrow{r}) > \sim < \alpha_k(\overrightarrow{r}) * h(\overrightarrow{r}) > \xrightarrow{M\to\infty} \mu_0\eta[f(\overrightarrow{r}) * h(\overrightarrow{r})], \tag{4.4}$$

where $\eta = < g_k(\overrightarrow{r}) >_{k,\overrightarrow{r}}$ is the volume fraction of absorbers that are on average homogeneously distributed in the sample.

To investigate the potential of the SOFI approach in PA fluctuation-based imaging, numerical simulations were first carried out by Thomas Chaigne, in the context of the collaboration between our group and Pr. Ori Katz's group. In these FDTD-based 2D simulations, we modelled PA signals generated by optical absorbers distributed randomly inside a flat branching structure mimicking a vascular network. An example of a single random distribution of absorbers $g_k(\overrightarrow{r})$ inside the branching structure $f(\overrightarrow{r})$ is provided in Fig. 4.2a. Some simulation results are illustrated in Fig. 4.2b-g. In particular, Fig. 4.2c shows the mean image that is an estimate of $f(\overrightarrow{r}) * h(\overrightarrow{r})$ and corresponds to conventional PA imaging. It can be clearly seen that the resolution pro-

vided by conventional imaging is too poor to resolve the branching structure. Fig. 4.2d-f shows the 2nd-, 3rd- and 5th-order cumulant images calculated for N = 50,000 simulated distributions of absorbers. In each image the inset displays the absolute value of the corresponding nth-power PSF $|h^n(\overrightarrow{r})|$.

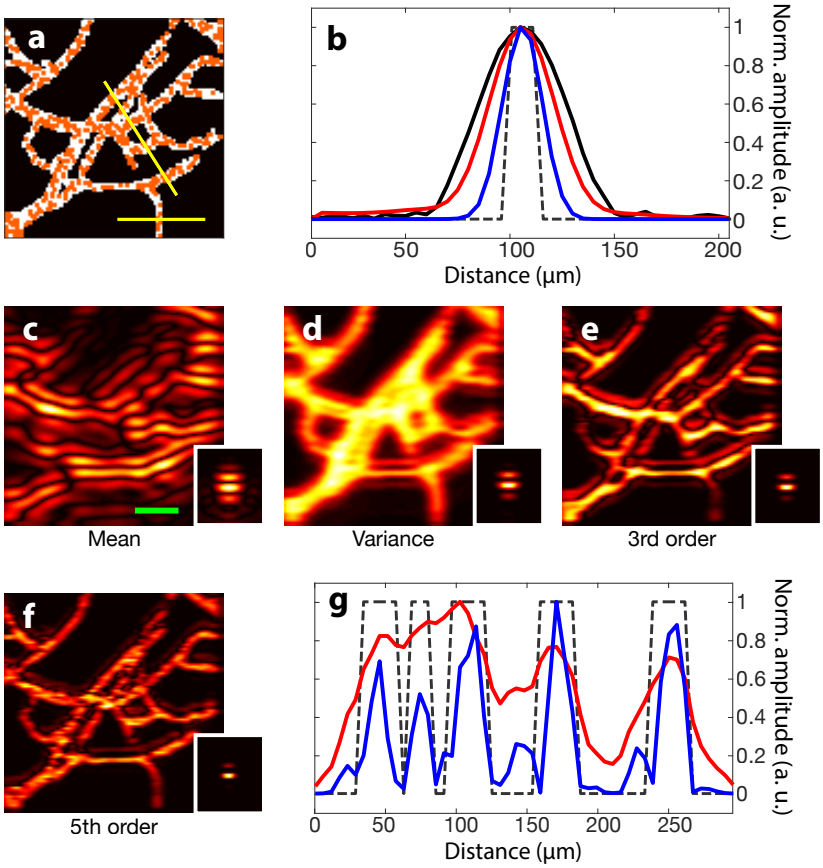

Fig. 4.2 Numerical results obtained for a vessel-like phantom. (a) Branching structure (white) with small round shape absorbers (orange). The yellow lines indicate the directions of the cross-sections in (b) and (g). (b) Cross-sections along the horizontal yellow line in (a): dashed gray: target structure, red: variance, blue: 5th-order cumulant, black: transverse cross-section of the main lobe of the PSF (inset in (c)). (c) Absolute value of the mean PA image. Scale bar: 100 μm. Inset: absolute value of the PSF, $|h(\overrightarrow{r})|$. (d) Variance image. Inset: $|h^2(\overrightarrow{r})|$. (e) Absolute value of the 3rd-order cumulant. Inset: $|h^3(\overrightarrow{r})|$. (f) Absolute value of the 5th-order cumulant. Inset: $|h^5(\overrightarrow{r})|$. (g) Cross-sections along the oblique yellow line in (a): dashed gray: target structure, red: variance, blue: 5th-order cumulant.

The results shown in Fig. 4.2d-f confirm the ability of high-order fluctuation processing to enhance the resolution. The resolution increases with the order of the cumulant : while it is impossible to distinguish individual vessels in the variance image (Fig. 4.2d), the 5th-order cumulant (Fig. 4.2f) successfully resolves most of the branching structure. Fig. 4.2b,g provides a comparison of resolution given by different cumulant orders. As a quantitative measure of the resolution improvement, we computed the full width at half maximum (FWHM) of an isolated thin vessel cross-section (Fig. 4.2b)

for different cumulant orders and compared it with the transverse FWHM of the 1st-order PSF (inset in Fig. 4.2c). The resulting transverse FWHM were found to be ΔX = 49 μm for the 1st-order PSF, ΔX = 36.5 μm for the variance image and ΔX = 21 μm for the 5th-order cumulant. This narrowing of the FWHM falls in line with the theoretically expected $\sqrt{n}$ resolution improvement [Dertinger et al., 2009].

To experimentally validate the proposed approach, we conduct two proof-of-principle experiments. In the first experiment, we seek to obtain a super-resolved cross-sectional image of five parallel microfluidic channels by using fluctuations of microbeads passing through the channels. In the second experiment, we perform super-resolution imaging of the same structure by using fluctuations of a blood flow passing through the channels. To perform SOFI-based reconstruction, we compute not only the variance image, as Chaigne et al. did with speckle illuminations [Chaigne et al., 2016], but also cumulant images of higher orders.

4.2 Materials and methods

4.2.1 Samples

In both experiments we used identical microfluidic samples consisting of five parallel microchannels with a rectangular cross-section (Fig. 4.3). To perform cross-sectional imaging, the microchannels were placed perpendicularly to the imaging plane XZ of a linear transducer array (type L22-8, see Chapter 2) at the ultrasound (US) probe elevational focus distance z_f = 15 mm. In this plane, each channel was h_{ch} = 50 μm high and w_{ch} = 40 μm wide, the center-to-center distance between neighbouring channels being L_{cc} = 180 μm. For more details on fabrication of the microfluidic sample the reader is referred to Chapter 2.

In the first experiment, a water suspension of 10 μm diameter absorbing beads was used. The particle concentration in the suspension was set at $\sim 10^4$ particles per mm^3 (6.3% volume fraction) corresponding to about 15 particles per channel (within the 1 mm thick imaging plane defined by the elevation focus of the US transducer). This relatively low particle concentration was chosen in order to avoid microbeads clogging the microfluidic circuit. The suspension of microbeads was prepared according to the following recipe: 12.5% of the initial 5% microbeads water suspension (Microparticles GmbH, Berlin, Germany), 0.025% of a buffer solution (TWEEN20, Sigma-Aldrich Corp., St. Louis, MO, USA), 19.6% of a density gradient medium (OptiPrep, ProteoGenix SAS, Schiltigheim, France), and 67.9% of water. The buffer solution was used to avoid microbeads sticking to each other whereas the density gradient medium was added to prevent microbeads from precipitating and getting stuck inside the pump system.

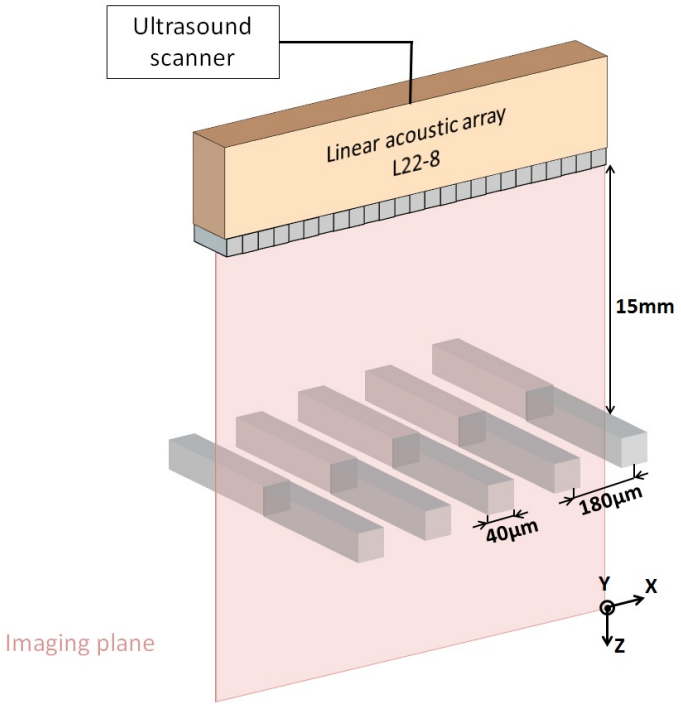

Fig. 4.3 The microfluidic sample consisting of five parallel microchannels is placed perpendicularly to the imaging plane XZ of the linear transducer array at the US probe elevation focus distance z_f = 15 mm. In this plane, each channel is h_{ch} = 50 μm high and w_{ch} = 40 μm wide, the center-to-center distance between neighbouring channels being L_{cc} = 180 μm.

In the second experiment, the microbeads suspension was replaced with whole blood flowing through the channels.

4.2.2 Measurement protocol

The experimental setup is shown in Fig. 2.1. A liquid with moving absorbers (microbeads/RBCs) was flown into the microchannels by a syringe pump providing a constant volumetric flow rate, corresponding to about 2.5 cm/s in the channels to image. At each laser shot ($\lambda_{laser} = 532\ nm$, PRR=100 Hz), the PA signals emitted by the absorbers passing through the imaging plane were recorded by a linear transducer array (type L22-8). For further information about the acquisition equipment the reader is referred to Chapter 2. In the first experiment, N = 20,000 PA acquisitions were performed resulting in the total experiment time of T_{exp} = 3.3 min. In the second experiment, N = 75,000 PA acquisitions were done resulting in the total experiment time of T_{exp} = 12.5 min.

4.2.3 Signal processing

First, the horizontal (arriving at the same time on all transducer elements) laser noise on each acquired RF frames was removed by subtracting the mean value over each

line of the frame (see section 2.2). Afterwards, complex-value beamforming images were obtained by applying standard delay-and-sum beamforming to the RF data (see Appendix 1 for the beamforming algorithm). In this beamforming operation, we assumed a homogeneous speed of sound v_s = 1500 m/s, neglecting the thin (180 μm-thick) polydimethylsiloxane (PDMS) layer covering the channels (see section 2.6). To perform statistical analysis, we removed correlated images: to do it, we determined the fluctuation decorrelation rate by computing correlation between the real components of successive beamforming images after removing from each reconstruction pixel its mean value. As a result, every 5th image was chosen for further processing in both experiments, reducing the effective laser PRR from 100 Hz to 20 Hz.

4.2.3.1 SVD analysis to separate sources of fluctuations

Although the laser noise had been removed, the obtained beamformed images were still contaminated by electronic noise of the acquisition system. To separate fluctuations of absorbers from this electronic noise, we used spatiotemporal filtering through singular value decomposition (SVD). In brief, SVD decomposes the initial data into a basis of spatiotemporal singular vectors. By choosing carefully the singular vectors corresponding to relevant fluctuations, one can discard signals with different spatiotemporal behaviour such as tissue clutter, electronic noise, etc. Specifically, in our experiments all singular vectors with indices $i > 12$ were attributed to electronic noise of the acquisition system. In addition, the first two singular vectors were found to encode a strong mean signal, probably due to the imperfect laser jitter correction. So, only the singular vectors with indices i = 3...11 were kept for the subsequent processing. More details on the SVD approach can be found in Appendix 3.

4.2.3.2 Cumulants for complex-valued signals

In PA and US imaging, the finite bandwidth of the US probe leads to axial oscillations in the reconstruction image. These oscillations are not related to the imaged object and therefore should be removed to avoid being recognized as real structure patterns. In conventional PA and US imaging, such oscillations are eliminated by computing the envelope of the complex analytical signal, i.e. the magnitude of complex-value images, obtained with Hilbert transform (see Appendix A). To retrieve similar envelope- or magnitude-related information as a result of SOFI processing, one can not simply apply Hilbert transform to cumulant images obtained for non-complex RF data, since cumulant images are non-linearly related to the initial RF data. For example, cumulants of even orders are, by definition, non-negative.

To eliminate PSF-related oscillation artifacts in cumulant images, we developed an analytical signal processing framework by generalizing real-value moments and

cumulants to complex random variables [Eriksson et al., 2010]. The proposed analysis is based on complex-value PA images obtained by beamforming complex RF data with the real part composed of the acquired RF data and the imaginary part obtained by applying columnwise Hilbert transform to the acquired RF data. Following *Eriksson et al.* [Eriksson et al., 2010] we define the nth order complex moment as: $m_{p,q}(\overrightarrow{r}) = 1/N \sum_{k=1}^{N} [A_k(\overrightarrow{r})]^p.[A_k(\overrightarrow{r})^*]^q$ where $q = n - p$. Then, complex cumulants of order $n = p + q$, $K_{p,q}$, are linked to complex moments $m_{p,q}$ in the following way (derived from *Eriksson et al.* [Eriksson et al., 2010]):
For $q > 0$:

$$K_{p,q}(\overrightarrow{r}) = m_{p,q}(\overrightarrow{r}) - \sum_{u=1}^{p}\sum_{v=1}^{q-1}\binom{p}{u}\binom{q-1}{v} K_{p-u,q-v}(\overrightarrow{r}) m_{u,v}(\overrightarrow{r}) \tag{4.5}$$
$$- \sum_{v=1}^{q-1}\binom{q-1}{v} K_{p,q-v}(\overrightarrow{r}) m_{0,v}(\overrightarrow{r}) - \sum_{u=1}^{p}\binom{p}{u} K_{p-u,q}(\overrightarrow{r}) m_{u,0}(\overrightarrow{r});$$

For $q = 0$:

$$K_{p,0}(\overrightarrow{r}) = m_{p,0}(\overrightarrow{r}) - \sum_{u=1}^{p-1}\binom{p-1}{u-1} K_{u,0}(\overrightarrow{r}) m_{p-u,0}(\overrightarrow{r}). \tag{4.6}$$

There are $n+1$ complex cumulants for a given order $n = p+q$. In addition, $K_{p,q} = K_{q,p}^*$.

Thanks to additivity and homogeneity of complex cumulants [Eriksson et al., 2010], the nth order complex cumulant involves convolution with $h(\mathbf{r})^p h(\mathbf{r})^{q*}$, i.e. with the complex PSF of the nth-order only. In particular, for even orders n and $p = q$, $|K_{p,q}(\overrightarrow{r})|$, involves convolution with $|h(\overrightarrow{r})|^{2p} = |h(\overrightarrow{r})|^n$ which is the real nth-order PSF, so the cumulant images obtained for even orders are the closest to the object. For both even and odd orders, we observed that the more p differs from q, the coarser the resulting cumulant image.

4.3 Results

4.3.1 Bead samples

In the first experiment, we seek to obtain super-resolution via SOFI imaging based on PA signal fluctuations induced by a flow of absorbing microbeads in the microfluidic channels.

Fig. 4.4 shows typical signals from one PA acquisition in the microbeads experiment. It can be noticed that on the RF frame apart from the relevant signal from the microbeads passing through the imaging plane (the curve with the maximum at $\{t \approx 12$ μs, $N \approx 64\}$) there are signals from other sources, including a signal from the sample

surface (horizontal line at $t \approx 11.75\ \mu s$) and some horizontal laser noise (at $t \approx 11.75\ \mu s$) which has not been completely removed by subtracting the average value across each line of the RF frame.

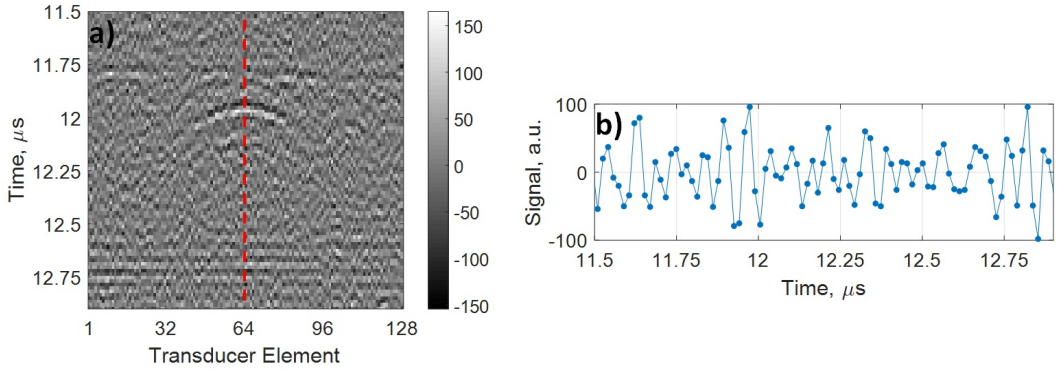

Fig. 4.4 Typical PA signals from one PA acquisition in the microbeads experiment. (a) RF frame. (b) Signal on the 64th transducer element (dashed line in (a)).

In our experiments, reconstruction was based on the set of images obtained by applying SVD filtering to the whole series of the initial beamforming images. Fig. 4.5 shows a typical beamforming image resulting from a single PA acquisition (a,b) and the corresponding filtered image after applying SVD processing (c,d). First, no image displays the correct structure. Then, it can be clearly seen that SVD filtering makes relevant fluctuations more visible by removing the noise as well as the parasite source seen in the top left corner of the reconstruction images shown in Fig. 4.5a,b.

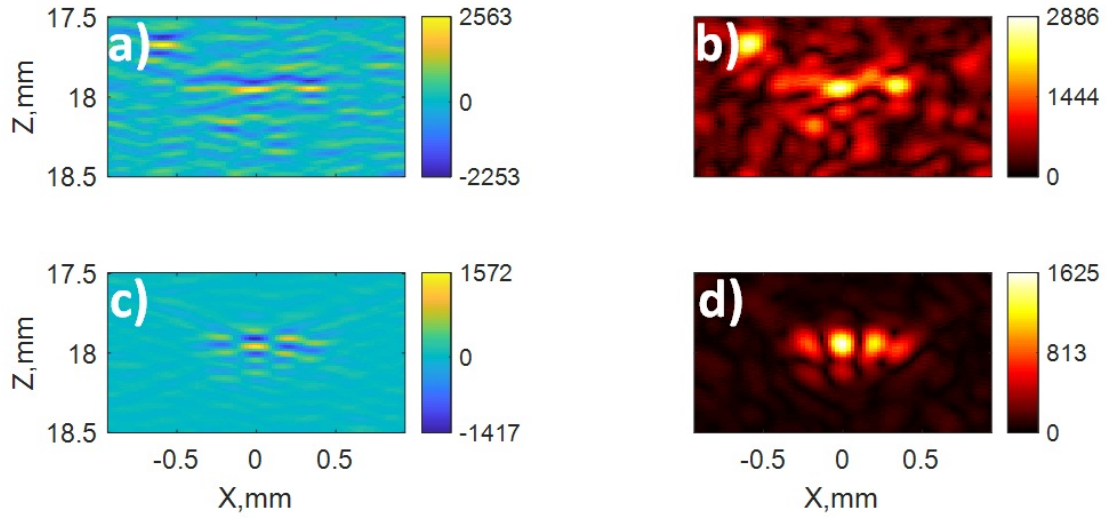

Fig. 4.5 Typical beamforming image resulting from a single PA acquisition (a,b) and the corresponding filtered image after applying SVD processing (c,d) in the microbeads experiment. (a,c) Reconstruction image corresponding only to the real part of the RF data. (b,d,) Envelope reconstruction image.

Reconstruction results obtained in the microbeads experiment are summarized in

Fig. 4.6. As can be observed, the microfluidic channels are indistinguishable in the mean image (Fig. 4.6c) while they are resolved by cumulants starting from the 2nd order (Fig. 4.6d-g,i-l).

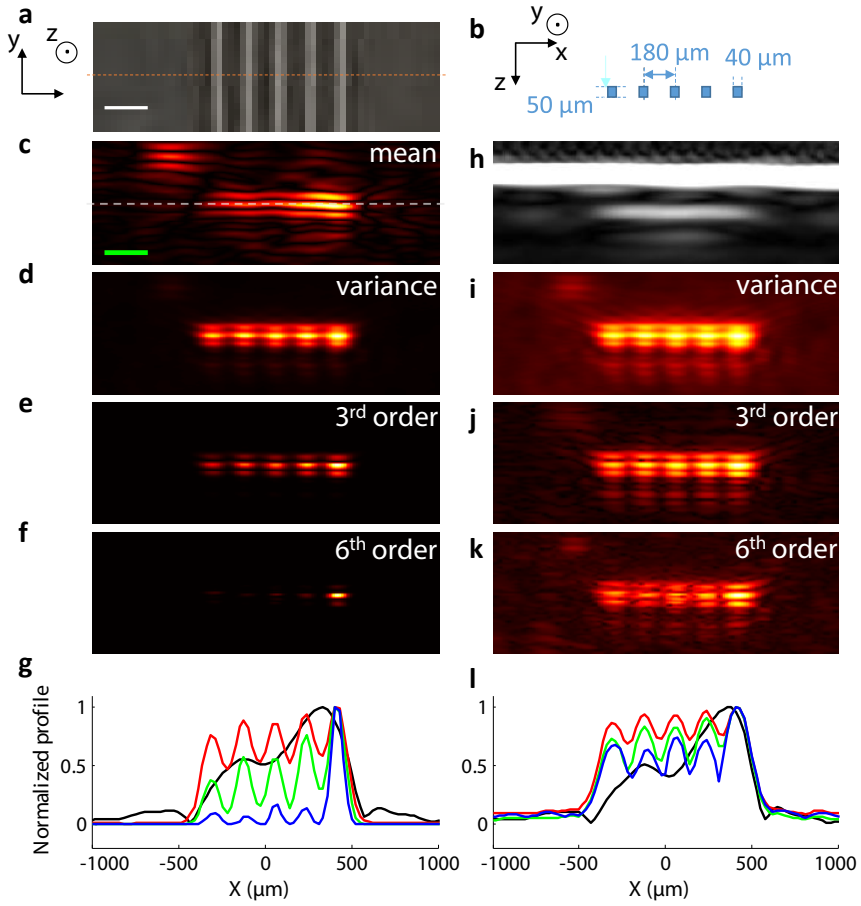

Fig. 4.6 Experimental results obtained by calculating real value cumulants with Eq. (4.1). (a) Top-view photograph of the microfluidic circuit demonstrates 5 parallel channels crossing the XZ imaging plane (dashed orange line). Scale bar: 250 m. (b) Schematic of the imaged channels cross-section with relevant dimensions. (c) Absolute value of the mean PA image, which represents the result of conventional PA imaging. Scale bar: 250 m. (d) Variance image (2nd-order cumulant). (e) Absolute value of the 3rd-order cumulant. (f) 6th-order cumulant. (g) One-dimensional profiles across the channels (orange dashed line in (c)) for the mean (black), variance (red), 3rd-order (green) and 6th-order (blue) cumulant images. (h) Pulse-echo US image of the 5 channels filled with air illustrates the inability to resolve the structure with conventional imaging. (i-k) nth-root of the nth-order cumulant: $n = 2$ (i), $n = 3$ (j) and $n = 6$ (k) computed to provide images with comparable intensity. (l) One-dimensional profiles across the channels for the nth-root of the nth-order cumulant: $n = 1$ (black), $n = 2$ (red), $n = 3$ (green) and $n = 6$ (blue).

To confirm the inability to resolve the channels in conventional imaging we also obtained an US pulse-echo image of the microchannels filled with air. In this image, shown in Fig. 4.6h, the channels appear as a continuous line (the saturated top line corresponds to the strong reflection at the PDMS/water interface). So, the channels in

Fig. 4.6h are indistinguishable, like in the mean PA image (Fig. 4.6c). This inability to resolve the channels in conventional imaging stands in agreement with the diffraction theory as by construction the center-to-center distance between neighbouring channels L_{cc} = 180 μm is below the the lateral FWHM of the PSF ($\Delta X \approx 200\ \mu m$).

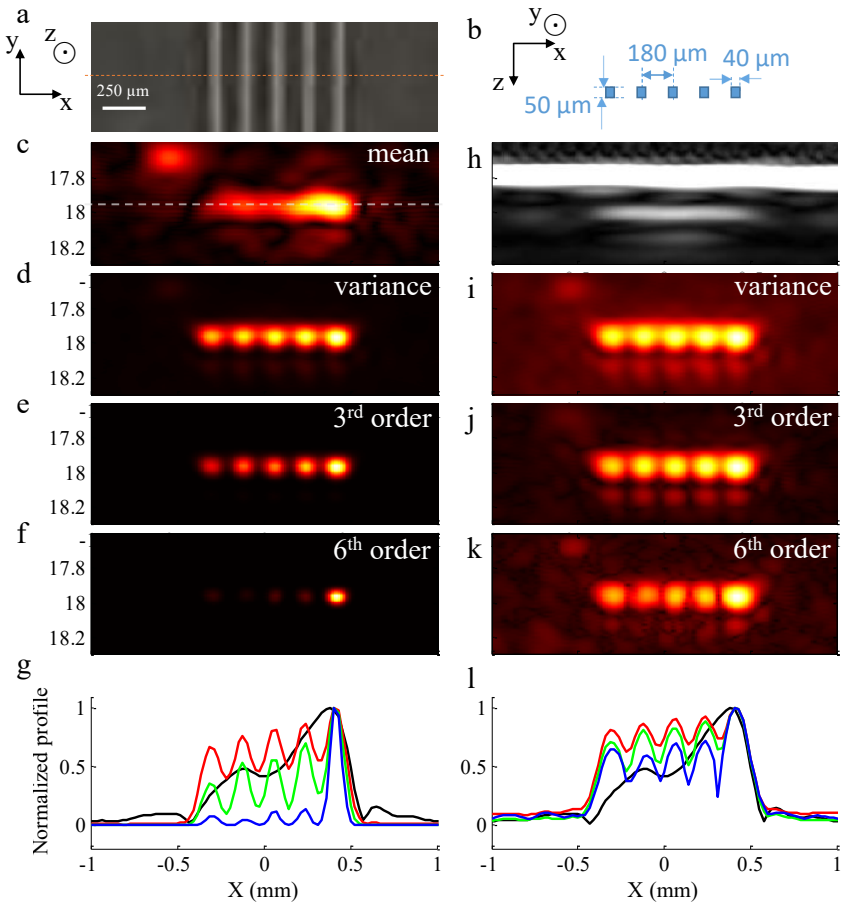

Fig. 4.7 Experimental results obtained by calculating real value cumulants with Eq. (4.5). (a) Top-view photograph of the microfluidic circuit demonstrates 5 parallel channels crossing the XZ imaging plane (dashed orange line). Scale bar: 250 m. (b) Schematic of the imaged channels cross-section with relevant dimensions. (c) Absolute value of the mean PA image, which represents the result of conventional PA imaging. Scale bar: 250 m. (d) Absolute value of the 2nd-order complex cumulant. (e) Absolute value of the 3rd-order complex cumulant. (f) Absolute value of the 6rd-order complex cumulant. (g) One-dimensional profiles across the channels (orange dashed line in (c)) for the mean (black), variance (red), 3rd-order (green) and 6th-order (blue) cumulant images. (h) Pulse-echo US image of the 5 channels filled with air illustrates the inability to resolve the structure with conventional imaging. (i-k) nth-root of the nth-order complex cumulant: $n = 2$ (i), $n = 3$ (j) and $n = 6$ (k) computed to provide images with comparable intensity. (l) One-dimensional profiles across the channels for the nth-root of the nth-order cumulant: $n = 1$ (black), $n = 2$ (red), $n = 3$ (green) and $n = 6$ (blue).

In contrast to the conventional resolution images, cumulant processing resolves individual channels (Fig. 4.6d-f). The corresponding resolution improvement can be observed on the one-dimensional profiles shown in Fig. 4.6g. The lateral FWHM of

the leftmost channel was estimated to be ΔX = 132 μm, 108 μm, 90 μm, 84 μm and 72 μm for orders from 2 to 6 correspondingly. So, the experimental resolution improvement follows closely the theoretical $\sqrt{n}$. Since nth-order cumulants are non-linearly related to the absorption profile they overweight structures producing stronger signals [Dertinger et al., 2009]. To account for this nonlinear weighting, the nth-root of the nth-order cumulant can be used rather than the nth-order cumulant itself (Fig. 4.6i-k). In such a case, the nth-root provides a quantity that is linearly related to the absorption profile. Notably, even when the nth-root is taken, the channels are better resolved at higher orders (Fig. 4.6l).

We would also like to emphasize that more images were needed to calculate high order cumulants. In numerical simulations, we observed that the number of PA images required for computing the n-th order cumulant increases with the cumulant order n in a complex manner [Chaigne et al., 2017].

The experimental results presented as real cumulants in Fig. 4.6 are shown in Fig. 4.7 as the magnitude of complex cumulant images. In particular, Fig. 4.7d- f shows the complex cumulants calculated for even ($p = q$) and odd ($p = q + 1$) orders. By taking the absolute value of complex cumulants, the axial oscillations present in Fig. 4.6 are effectively removed. In addition, the lateral profiles and resolution obtained with the real and complex cumulants are the same. Again, taking the nth root of cumulants permits correcting the difference between the strength of the sources while preserving super-resolution.

4.3.2 Blood samples

Although the results obtained in the first experiment demonstrate that SOFI processing based on fluctuations caused by moving absorbers can lead to super-resolution, this does not unconditionally mean that the proposed approach will also be effective when exploiting blood flow fluctuations for super-resolution imaging of blood vessels. A possible discrepancy in the results might be caused, for example, by diverging physical properties of the two kinds of absorbers and the difference in their concentration ($c \sim 10^4$ particles/mm^3 for microbeads against $c \sim 10^6$ particles/mm^3 for RBCs). Hence, to demonstrate that SOFI processing can lead to super-resolution by exploiting RBCs-induced fluctuations we carried out the second experiment where a flow of human blood was induced inside the channels.

Fig. 4.8 shows typical signals from one PA acquisition in the blood flow experiment. It can be noticed that apart from the relevant signal from the RBCs in the imaging plane (the curve with the maximum at $\{t \approx 11.75\ \mu s,\ N \approx 64\}$) on the RF frame there is a signal from the sample surface (horizontal line at $t \approx$11.75 μs) and a signal from a parasite source on the surface (the curve with the maximum at $\{t \approx 11.8\ \mu s,$

$N \approx 96\}$). It should also be noted that the signal from RBCs is stronger than the signal from microbeads (Fig. 4.4). As the experimental conditions were almost identical, this strong difference in the signal amplitude can be explained by the much higher concentration of RBCs compared to the concentration of microbeads and the difference between the absorption coefficients of these two types of absorbers.

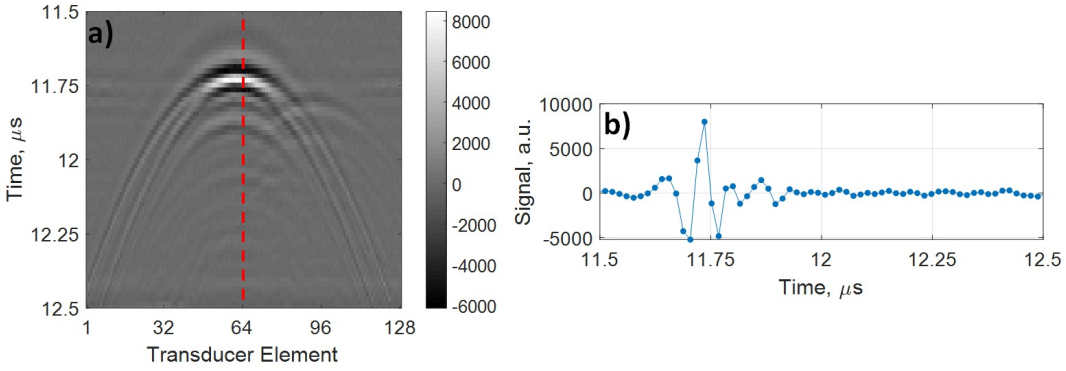

Fig. 4.8 Typical PA signals from one PA acquisition in the blood flow experiment. (a) RF frame. (b) Signal on the 64th transducer element (dashed line in (a)).

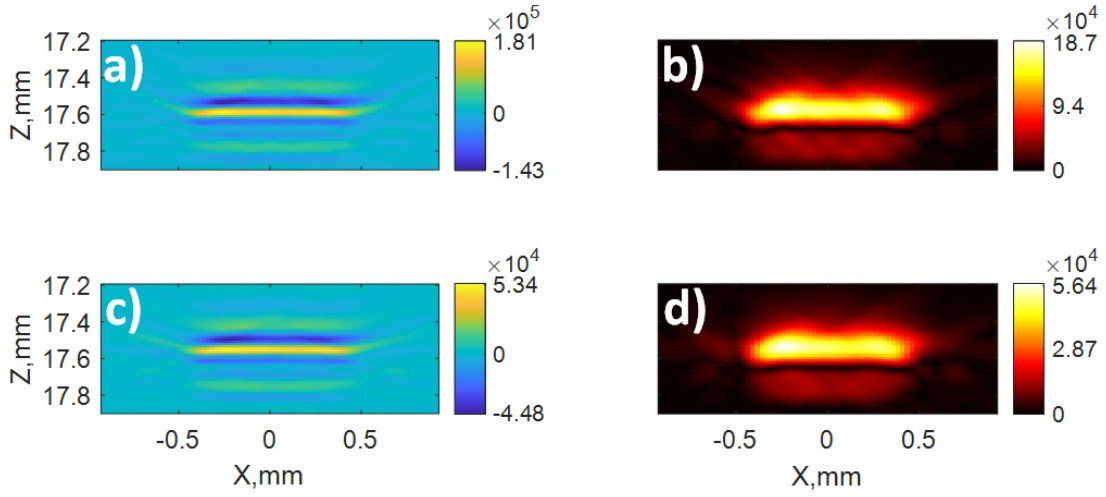

Fig. 4.9 Typical beamforming image corresponding to a single PA acquisition (a,b) and the corresponding filtered image after applying SVD processing (c,d) in the blood flow experiment. (a,c) Reconstruction image corresponding only to the real part of the RF data. (b,d,) Envelope reconstruction image.

Fig. 4.9 shows a typical beamforming image corresponding to a single PA acquisition (a,b) and the corresponding filtered image after applying SVD processing (c,d). Although the effect of SVD filtering on each beamforming image may not seem significant, we did not manage to obtain a super-resolved SOFI image without using SVD to separate relevant fluctuations from the noise of the acquisition system. It is to be emphasized that contrary to the well-controlled experiment with microbeads, it was

considerably more difficult to provide a stable and controllable blood flow inside the sample. So, the quality of SOFI processing was highly dependent on the chosen dataset and the selection of singular vectors for SVD filtering.

Fig. 4.10 summarizes the reconstruction results in the blood flow experiment. First, Fig. 4.10b shows an optical microscope image taken when a blood flow was induced inside the channels. The upper inset in Fig. 4.10b illustrates packing of RBCs inside the channels while the lower inset shows static RBCs located at the input of the circuit. Both insets confirm the expected shape and concentration of RBCs. Then, as in the experiment with microbeads, SOFI processing reconstructs five super-resolved channels (Fig. 4.10c-f) which are completely indistinguishable in the mean PA image (Fig. 4.10a).

It is to be noted that we did not manage to reconstruct the object with any cumulant of order $n < 6$. A possible reason is that not all noise-related fluctuations are removed by the SVD filtering as this technique can not distinguish relevant and non-relevant fluctuations with the same spatiotemporal behaviour. As a result, the object becomes apparent only at $n = 6$ as the 6th-order cumulant of noise-related fluctuations gets weak enough.

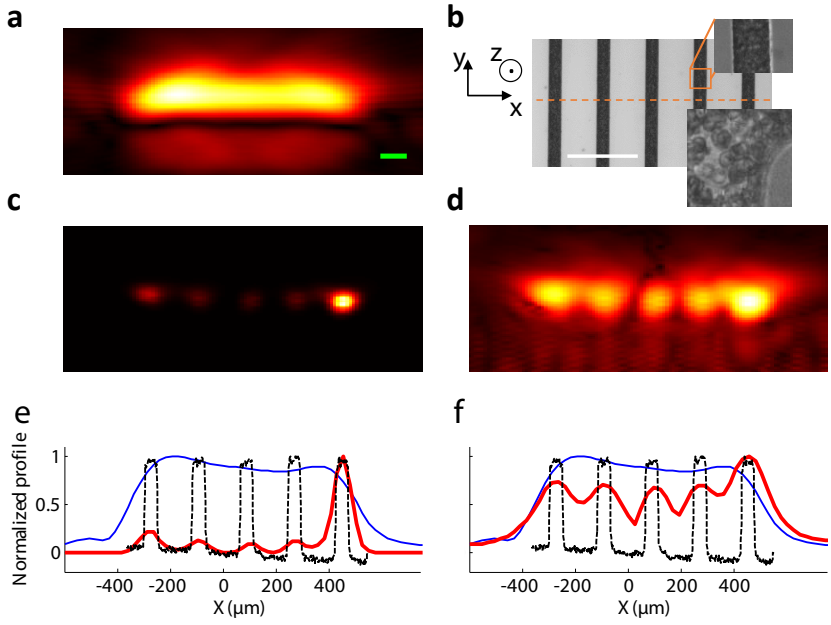

Fig. 4.10 SOFI demonstration using human blood at physiological concentration and N = 15,000 PA images. (a) Mean PA image. Scale bar: 100 μm. (b) Microscope picture of blood flow in the microfluidic channels. Scale bar: 250 μm. Upper inset: larger magnification. Lower inset: RBCs at the input of the circuit. (c) 6th-order complex cumulant. (d) 6th root of the 6th-order complex cumulant. (e-f) Corresponding intensity profiles comparing the mean (blue), 6th-order cumulant (red), and microscope profiles (dashed black).

4.4 Conclusion

We demonstrated that flow-induced fluctuations of PA signals can be used to provide resolution beyond the acoustic diffraction limit. Specifically, we showed that a $\sqrt{n}$ resolution improvement can be achieved via nth-order cumulant analysis. Importantly, thanks to the extended SOFI processing developed in this Chapter, PSF-related oscillations in the resulting super-resolution images can be eliminated. As follows from the results of the experiment with human blood, the proposed method may potentially be used for super-resolution imaging of small densely packed blood vessels. In contrast to localization-based imaging (see Chapter 3) which requires diluted contrast agents added to the blood flow, fluctuation-based imaging is intrinsically based on the endogenous PA contrast of blood.

Despite these promising results, fluctuation-based PA imaging suffers from several limitations. First, as was demonstrated by our blood flow experiment, it can be difficult to separate relevant fluctuations from noise-related fluctuations. When this is done via SVD filtering, the choice of the relevant singular vectors is non-trivial and may be challenging when the imaged object is not known *a priori*. One other limitation is that objects associated with stronger PA signals mask objects associated with weaker PA signals when high order cumulants are computed. As a consequence, in the real imaging environment slight spatial variations of the light intensity may result in weak sources being invisible in the n-th order cumulant image. Finally, the temporal resolution of the proposed technique is intrinsically low. One of the main reasons is that calculating the nth-order cumulant requires a certain number of uncorrelated PA images. The need for *uncorrelated* images may increase further the total acquisition time when imaging small vessels, where blood velocities are of the order of several millimeters per second. On the other hand, the temporal resolution will be limited by the laser pulse repetition rate when imaging large blood vessels, where blood velocities are high. Nevertheless, the eventual acquisition time may be shorter than the acquisition time required by the localization approach (see Chapter 3) since in SOFI imaging a high density of absorbers can be used, whereas localization generally requires that few absorbers appear in the imaging zone at a given moment.

The results of this Chapter obtained in cross-sectional (two-dimensional) imaging of a vessel-like phantom form the base for *in vivo* fluctuation-based super-resolution imaging in three dimensions. Such experiments are being prepared in the context of the PhD study of Guillaume Godefroy. Regarding the contributions of different members of our research team to the results reported in this Chapter, all the experiments were done by me with the assistance of Bastien Arnal. Bastien Arnal performed the SOFI-based processing with complex-value signals and Thomas Chaigne performed the numerical simulations. Here, not all simulation results have been reported. For example, in the

simulations it was demonstrated that the number of PA images required for computing the n-th order cumulant increases with the cumulant order n in a complex manner. For more simulation results, the reader is referred to [Chaigne et al., 2017].

CHAPTER 5

Super-resolution by model-based reconstruction[1]

5.1 Introduction

The duty of any image reconstruction method is to obtain an estimate of the imaged object using the measurement data, i.e. to solve the so-called *inverse problem*. Conventional diffraction-limited photoacoustic (PA) reconstruction was described in section 1.3.3.1. In the conventional reconstruction image, the object is distorted due to the system response that depends on PA generation, wave propagation in the medium, transducer aperture, transducer response function, etc. As a result of the finite system response, high spatial frequencies are lost and sub-diffractional features are indistinguishable in conventional reconstruction. The model-based reconstruction approach proposed in this Chapter may provide super-resolution as it explicitly takes the system response into account. The lack of information about high spatial frequencies is compensated by special constraints placed on the object to reconstruct.

This Chapter is organized as follows. First, we present the grounds of the model-based approach. These grounds do not depend on the nature of the inverse problem and would be valid for other imaging techniques. Afterwards, we propose a forward model for PA imaging that can be used as a basis for the proposed reconstruction approach. Then, we explain why the model-based approach could effectively handle the resolution problem in PA imaging. After presenting some studies involving model-based reconstruction in PA imaging, we report results of a proof-of-concept experiment. In this experiment, we compare reconstruction based on different constraints imposed on the sought object. After that, we conduct more experiments alongside with numerical simulations to determine the resolution limit that can be achieved in model-based reconstruction. We end this Chapter with a theoretical analysis focused on some important aspects of model-based reconstruction including the reliability of the method.

[1] Numerical simulation data was provided by E. Bossy.

5.2 Model-based reconstruction approach

5.2.1 Forward measurement model

The imaged object is defined by the probed property, such as optical absorption. Hence, the imaged object is in principle continuous. However, the measurement data is often discrete in modern digital imaging systems. So, using digital methods for reconstructing the object should involve discretization of the object. To construct an appropriate forward model that can be used in reconstruction, we discretize the imaged object by representing it in the vector form $T_0^{N\times 1}$. As concerns the discrete measurement data, we consider that it is contained in the vector $R^{M\times 1}$. In the absence of noise, a forward linear problem can be written in the form of a system of linear equations:

$$R = \boldsymbol{A}T_0, \tag{5.1}$$

with $\boldsymbol{A}^{M\times N}$ being a matrix of system response (also the propagation matrix or the forward model).

In practice, there is some additive noise inevitably present in the measurement vector R. By taking this noise into account, one can model measurements (5.1) as

$$R = \boldsymbol{A}T_0 + B, \tag{5.2}$$

with $B^{M\times 1}$ being a random vector describing the measurement noise.

5.2.2 Ill-posed linear inverse problems

The noise B can not be separated from the measurement data R. So, the inverse problem consists in finding the best estimate $\hat{T}_0$ of the imaged object T_0 from the measurements R using a known matrix $\boldsymbol{A}$ (either measured or theoretically predicted). The inversion result depends heavily on the matrix $\boldsymbol{A}$, so good estimation of this matrix is important. In the following sections, we will discuss how the matrix $\boldsymbol{A}$ can be obtained in the case of PA imaging.

In this chapter we will deal with situations when computing the object by direct inversion $\hat{T}_0 = \boldsymbol{A}^{-1}R$ is not possible. To explain why, we shall invoke the Kronecker-Capelli theorem. According to this theorem, a linear system has a solution if and only if the rank of its coefficient matrix $\boldsymbol{A}^{M\times N}$ is equal to the rank of its augmented matrix $[\boldsymbol{A}|R]$. If $rank(\boldsymbol{A}) = N$, the solution is unique, otherwise there are infinitely many solutions. This being said, it should be noted that in practice $rank(\boldsymbol{A})$ will not be equal to $rank([\boldsymbol{A}|R])$ due to the noise in the vector R. Second, even when the presence of noise can be neglected, in this chapter we will consider systems for which $rank(\boldsymbol{A}) < N$. In other words, we will have to deal with systems admitting many possible solutions,

or underdetermined systems. Problems that admit many solutions or those that do not admit any solutions are called *ill-posed problems*. In this chapter, we are going to consider ill-posed inverse problems.

So, inversion-based reconstruction should pursue two goals:

- Minimize the influence of the noise B on the inversion result.
- Choose among all possible objects the one which is the closest to the imaged object T_0.

To simultaneously attain these two goals we will perform inversion using so-called *regularization* methods.

5.2.3 Regularization-based solution

5.2.3.1 Principle

An estimate $\hat{T_0}$ of the imaged object T_0 can be obtained via the following minimization:

$$\hat{T_0} = \underset{T}{\operatorname{argmin}}\{||R - \boldsymbol{A}T||_2^2 + \alpha||\boldsymbol{\Phi}T||_p^p\}, \tag{5.3}$$

where $\boldsymbol{\Phi}$ is a certain transformation applied to the *tested* object T and the L_p norm is defined as $||T||_p = \sqrt[p]{\sum_{i=1}^{N} |T(i)|^p}$.

The first term $J_f = ||R - \boldsymbol{A}T||_2^2$ in the right hand side of Eq. (5.3) is called the fidelity term. When the fidelity term equals zero, the object T fits perfectly the measurement data R for the given model $\boldsymbol{A}$. In this case, the solution can be considerably affected by the noise in the measurement vector R.

The second term $J_r = \alpha||\boldsymbol{\Phi}T||_p^p$ is the regularization term that is responsible for both selecting the unique object defined by the desired properties/constraints and minimizing the influence of the noise. The regularization parameter α should provide the trade-off between fitting the probed object to the measurement data on the one hand and handling the noise and the constraint on the other hand.

It should also be noted that some additional constraints may be placed on the object T while performing minimization (5.3). For example, the non-negativity constraint: $T(i) \geq 0$, $i = 1..N$.

5.2.3.2 Solutions corresponding to different constraints

The second term $J_r = \alpha||\boldsymbol{\Phi}T||_p^p$ in the right hand side of (5.3) permits choosing the unique object defined by the transformation $\boldsymbol{\Phi}$, norm L_p and regularization parameter α. Let us consider the most common cases:

1) $\alpha = 0$ ($J_r = 0$). Minimization (5.3) may result in one of many possible objects (non-uniqueness of the solution). Among these objects, the one with the minimal L2 norm is given by

$$\hat{T}_{L2} = (\boldsymbol{V}\boldsymbol{\Sigma}^{-1}\boldsymbol{U}^*)R, \tag{5.4}$$

where the matrices $\boldsymbol{V}$ and $\boldsymbol{U}$ correspond to the singular value decomposition (SVD) of the matrix $\boldsymbol{A}$:

$$\boldsymbol{A} = \boldsymbol{U}\boldsymbol{\Sigma}\boldsymbol{V}^*, \tag{5.5}$$

The matrix $\boldsymbol{\Sigma}^{-1}$ is diagonal, its diagonal values being $\boldsymbol{\Sigma}^{-1}(i,i) = 1/\sigma_i$, where $\sigma_i \geq 0$ are the diagonal values of the matrix $\boldsymbol{\Sigma}$.

When none of the singular values σ_i are zero operation (5.4) corresponds to Moore-Penrose pseudoinverse. The problem of Eq. (5.4) is that the resulting object $\hat{T}_{L2}$ can be very sensitive to the noise in the vector R. The simplest way to make the solution less sensitive to noise is to replace the matrix $\boldsymbol{\Sigma}^{-1}$ with the matrix $\boldsymbol{\Sigma}^{-1}_{ST}$ whose diagonal values are calculated as $\boldsymbol{\Sigma}^{-1}_{ST}(i,i) = w_{ST}(\sigma_i)/\sigma_i$, where w_{ST} is the simple truncation weighting function:

$$w_{ST}(\sigma) = \begin{cases} 1, & \sigma > \sigma_0 \\ 0, & \sigma \leq \sigma_0 \end{cases} \tag{5.6}$$

The thresholding value σ_0 plays the role of the regularization parameter α in (5.3). An inversion based on Eq. (5.6) is said to be based on a truncated singular value decomposition. 2) $\alpha \neq 0$ and $J_r = ||T||_2^2$. Minimization (5.3) corresponds to Tikhonov regularization. The Tikhonov solution can also be obtained using Eq. (5.4) when the matrix $\boldsymbol{\Sigma}^{-1}$ is replaced with the matrix $\boldsymbol{\Sigma}^{-1}_{TH}$ whose diagonal values are calculated as $\boldsymbol{\Sigma}^{-1}_{TH}(i,i) = w_{TH}(\sigma_i)/\sigma_i$, where w_{TH} is the Tikhonov weighting function:

$$w_{TH}(s) = \frac{s^2}{s^2 + \alpha}. \tag{5.7}$$

It should be noted that calculating SVD is challenging when the matrix $\boldsymbol{A}$ is large. In this case, iterative algorithms based on minimization (5.3) are preferred. Iterative algorithms are also used when additional constraints are to be involved in regularization.

3) $\alpha \neq 0$ and $J_r = ||T||_1$. L1-based (or sparsity-based) regularization is usually the method of choice when reconstructing sparse objects. The discrete object T is said to be k-sparse if it contains only k non-zero elements. The ability of L1-based reconstruction to provide the sparsest solution was demonstrated in the context of compressed sensing [Eldar and Kutyniok, 2012]. In the case of L1-based regularization there is no analytical solution and iterative minimization algorithms are to be used.

4) $\alpha \neq 0$, $J_r = ||T||_1$, with the additional non-negativity constraint imposed: $T(i) \geq 0$, $i = 1..N$. As the imaged object, such as a distribution of optical absorp-

tion, can not be negative, negative values in the reconstruction image may appear due to reconstruction artifacts only. So, to remove the negative values in the vector T the non-negativity constraint is sometimes applied at each iteration of the reconstruction algorithm. In addition, it has been noticed that the use of the non-negativity constraint can lead to iterative minimization converging faster.

5) $\alpha = 0$ ($J_r = 0$), with only the non-negativity constraint imposed: $T(i) \geq 0$, $i = 1..N$. To our knowledge, there is no reliable information on the possibility to reconstruct the object by using the non-negativity constraint without the regularization term. However, in this study, we will show that in some cases the non-negativity constraint can successfully replace the regularization term. We will call such reconstruction *positivity-based reconstruction*.

5.3 Photoacoustic forward model

5.3.1 Physical model

In this section, we discuss construction of a matrix-based forward model describing PA imaging with a multielement transducer array. The PA acquisition can be split into three stages:

1) Generation and propagation of PA waves. The PA effect in the heat confinement regime is described by Eq. 1.3. Then, the PA pressure wave $p(\overrightarrow{r}, t)$ can be related to the probed optical absorption $\mu_a(\overrightarrow{r})$ via a linear operator $\boldsymbol{H}_1(\overrightarrow{r}, t)$ encoding the Green function of the medium:

$$p(\overrightarrow{r}, t) = \boldsymbol{H}_1[\mu_a(\overrightarrow{r})\phi_r(\overrightarrow{r}, t)], \tag{5.8}$$

where $\mu_a(\overrightarrow{r})$ is the absorption distribution and $\phi_r(\overrightarrow{r}, t)$ is the fluence rate that can be written for short laser pulses as $\phi_r(\overrightarrow{r}, t) = \phi(\overrightarrow{r})f(t)$ with $f(t)$ being the time profile of a laser pulse.

2) Reception at many points by different transducer elements (spatial discretization) and integration of each received signal over the area of the corresponding element. For each element k the measured pressure can be written as

$$p_{mes}(\overrightarrow{r_k}, t) = \boldsymbol{H}_2[p(\overrightarrow{r}, t)], \tag{5.9}$$

where $\overrightarrow{r_k}$ is the radius-vector to element k and $\boldsymbol{H}_2(\overrightarrow{r_k}, \overrightarrow{r}, t)$ is a linear operator of spatial discretization and integration.

3) Conversion to electrical signals, quantization and discretization in the time do-

main. The recorded electrical signals are related to the measured pressure as

$$S(t_i, \overrightarrow{r_k}) = \boldsymbol{H}_3[p_{mes}(\overrightarrow{r_k}, t)], \tag{5.10}$$

where $\boldsymbol{H}_3(\overrightarrow{r_k}, t)$ is a linear operator of conversion, quantization and discretization in time.

Combining Eq. (5.8)-(5.10) one obtains

$$S(t_i, \overrightarrow{r_k}) = \boldsymbol{H}_3\boldsymbol{H}_2\boldsymbol{H}_1[\mu_a(\overrightarrow{r})\phi(\overrightarrow{r})f(t)]. \tag{5.11}$$

Eq. (5.11) can be written in a shorter form:

$$S(t_i, \overrightarrow{r_k}) = \mathbb{A}[\mu_a(\overrightarrow{r})\phi(\overrightarrow{r})], \tag{5.12}$$

where $\mathbb{A}$ is a global linear operator that relates the continuous imaged object with the measurement signal which is sampled in space and in time. It should be kept in mind that in general the operator $\mathbb{A}$ depends on the temporal intensity profile $f(t)$. However, for nanosecond laser pulses, the influence of the intensity profile can be in practice neglected due to the limited detection bandwidth included in H_3, a widely used assumption in photoacoustic imaging (see section 1.3.3.3).

5.3.2 Discretization of the problem

To obtain a model appropriate for digital processing, we shall discretize the operator $\mathbb{A}$ and the imaged object $\mu_a(\overrightarrow{r})$ in Eq. (5.12). Supposing that $\phi(\overrightarrow{r}) = const$, the imaged object can be discretized on an arbitrary spatial grid, so that each cell of the object $\boldsymbol{T}_0(i, j, k)$ is assigned to the optical absorption $\mu_a(x_i, y_j, z_k)$. The matrix $\boldsymbol{T}_0$ can then be rearranged to form the vector T_0 representing the object. Importantly, the vector T_0 defines the imaged object only on the chosen grid. The received radio-frequency (RF) signals $S(t_i, \overrightarrow{r_k})$ can also be rearranged to form the measurement vector R_{RF}. Then, the discretized forward problem reads

$$R_{RF} = \boldsymbol{A}_{RF}T_0, \tag{5.13}$$

where $\boldsymbol{A}_{RF}$ is the matrix corresponding to the discretized version of the operator $\mathbb{A}$.

There are two main ways to estimate the object T_0 from the measurements. First, by performing inversion corresponding to forward model (5.13). Second, one can try to derive T_0 from estimation of the object via a backprojection/beamforming algorithm. The two following sections describe each of these two possible approaches.

5.3.3 Construction of the RF-space propagation matrix $\boldsymbol{A}_{RF}$

Each column of the matrix $\boldsymbol{A}_{RF}$ contains the radio-frequency point spread function (RF-PSF) associated with a point source at a certain position in the imaging zone. In other words, each column of $\boldsymbol{A}_{RF}$ is the vector R corresponding to a point source at a certain position in the imaging zone.

There are different possible methods to estimate the matrix $\boldsymbol{A}_{RF}$.

1) To estimate $\boldsymbol{A}_{RF}$ theoretically, one needs to compute the operator $\boldsymbol{H}_1$ in Eq. (5.8) using the propagation theory, calculate the operator $\boldsymbol{H}_2$ in Eq. (5.9) according to the acquisition geometry and estimate the operator $\boldsymbol{H}_3$ in Eq. (5.10). This approach assumes a good knowledge of the propagation medium, imaging geometry and electroacoustic properties of each transducer element. As in practice all these parameters are not perfectly known, the resulting matrix $\boldsymbol{A}_{RF}$ may suffer from cumulative errors.

2) The matrix $\boldsymbol{A}_{RF}$ can be measured experimentally by acquiring PA signals for each point in the imaging zone. First, the measurement time is proportional to the number of acquisition points and can be too long. Second, the direct measurement approach assumes that all points in the imaging zone are accessible that is not often the case. Finally, a high precision of the displacement motors is needed and the medium should be stable during the whole measurement process.

3) Only one RF-PSF in the imaged zone is measured experimentally. All columns of $\boldsymbol{A}_{RF}$ are derived from this RF-PSF by using a certain propagation model. This approach assumes that the only difference between signals detected for different source positions consists in different propagation time. This difference is encoded in the operator $\boldsymbol{H}_1$ in Eq. (5.8) while the operator $\boldsymbol{H}_2$ in Eq. (5.9) is independent of the transducer and source coordinates. We implement this approach in the present chapter.

Under the assumptions stated above, if the single RF-PSF is acquired for a source placed at $\{x_q, z_q\}$, then column p of the matrix $\boldsymbol{A}_{RF}$ should be derived from the RF-PSF data which is shifted for each transducer element k according to the time difference Δt_{pqk}:

$$\Delta t_{pqk} = \frac{1}{v_s}\Big(\sqrt{(x_k - x_p)^2 + (z_k - z_p)^2} - \sqrt{(x_k - x_q)^2 + (z_k - z_q)^2}\Big), \qquad (5.14)$$

where $\{x_k, z_k\}$ are the coordinates of element k of the transducer array, $\{x_p, z_p\}$ are the coordinates corresponding to point p of the reconstruction grid.

The idea is illustrated in Fig. 5.1: the signals corresponding to the point P (olive) are derived by shifting in time the signals acquired for the point Q (crimson) according to the time differences $\Delta t_{pq1} = (r_3 - r_1)/v_s = t_3 - t_1$ (1st element) and $\Delta t_{pq3} = (r_4 - r_2)/v_s = t_4 - t_2$ (3rd element).

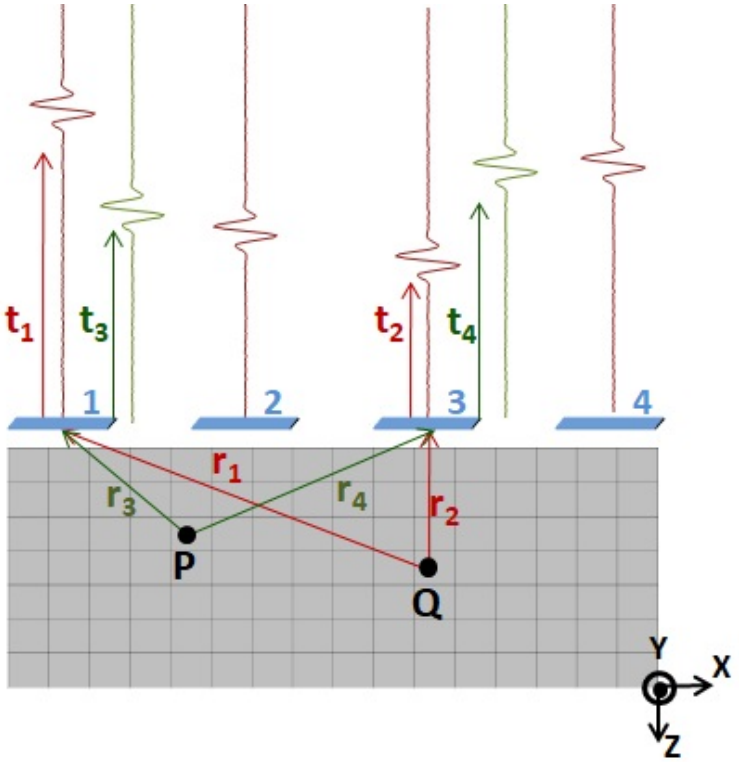

Fig. 5.1 Construction of the propagation matrix $\boldsymbol{A}_{RF}$: the signals corresponding to the point P (olive) are derived by shifting in time the signals acquired for the point Q (crimson) according to the time differences $\Delta t_{pq1} = (r_3 - r_1)/v_s = t_3 - t_1$ (1st element) and $\Delta t_{pq3} = (r_4 - r_2)/v_s = t_4 - t_2$ (3rd element).

5.3.4 Construction of the BF-space propagation matrix $\boldsymbol{A}_{BF}$

Let us denote R_{BF} the vector obtained by rearranging the beamformed image. As the beamformed image is linearly related to the optical absorption, there exists a matrix $\boldsymbol{A}_{BF}$ such that

$$R_{BF} = \boldsymbol{A}_{BF} T_0. \tag{5.15}$$

Each column of the matrix $\boldsymbol{A}_{BF}$ contains a bipolar PSF in the beamforming space (BF-PSF).

Two techniques can be used to compute $\boldsymbol{A}_{BF}$:

1) Each column of $\boldsymbol{A}_{BF}$ is obtained by beamforming the RF data contained in each column of $\boldsymbol{A}_{RF}$.

2) One column of $\boldsymbol{A}_{BF}$ is computed by beamforming data corresponding to one point source and all other columns are obtained by translating this PSF in the beamforming space. In this case, translational invariance of the BF-PSF is assumed.

In this PhD study, we only assume translational invariance in the time domain to compute the matrix $\boldsymbol{A}_{RF}$. So, we construct the matrix $\boldsymbol{A}_{BF}$ from $\boldsymbol{A}_{RF}$ using the first suggested technique, without supposing translational invariance in the beamforming

space.

5.3.5 Resolution and ill-posedness of the reconstruction problem

Here, we shall specify some cases when PA reconstruction deals with an underdetermined system and regularization-based techniques are required to obtain the right solution. For the sake of simplicity, we neglect the noise in the measurement data.

Let us consider imaging in an isotropic homogeneous medium performed with a multielement transducer array with a circular aperture of diameter D. The resonance frequency of the transducer f_c corresponds to the wavelength $\lambda_{ac} = v_s/f_c$, where v_s is the speed of sound in the medium. The spacing between neighbouring elements of the array is approximately $\lambda_{ac}/2$ ($\lambda_{ac} << D$), following the Nyquist condition for spatial sampling. So, the total number of transducer elements is $N_{el} \approx \pi D/(\lambda_{ac}/2)$. The imaging geometry is shown Fig. 5.2.

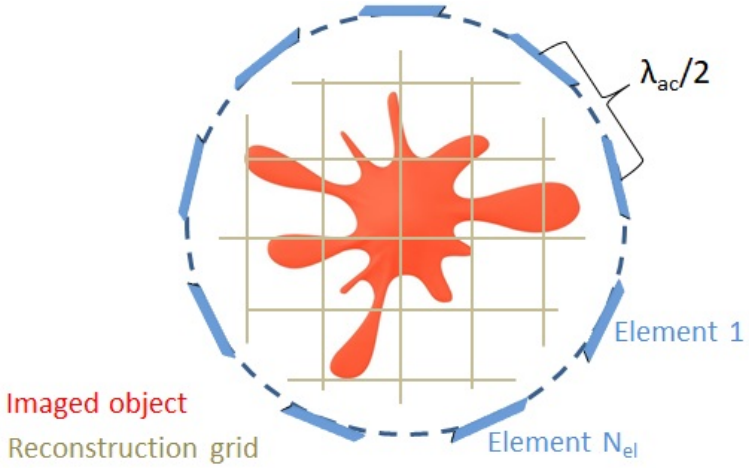

Fig. 5.2 Imaging with a multielement array having a circular aperture covering the whole angle $\Omega_0 = 2\pi$. The distance between neighbouring elements is about $\lambda_{ac}/2$, the aperture diameter is D.

We seek to reconstruct the object over a 2D grid with a step of $\lambda_{ac}/2$. The grid fills the whole imaging space inside the transducer aperture. Then, the number of points N of this grid can be estimated as

$$N \sim \frac{\pi D^2}{4 * \left(\frac{\lambda_{ac}}{2}\right)^2}. \tag{5.16}$$

If the RF signals are acquired with the sampling frequency $f_s = 2f_c = 2v_s/\lambda_{ac}$ then the number of samples M can be estimated as

$$M \sim 2N_{el}\frac{D}{\lambda_{ac}} = 4N. \tag{5.17}$$

It follows from Eq. (5.16) and (5.17) that $M \geq N$. If the M measurements are independent then $rank(\boldsymbol{A}) = N$. Therefore, the inverse problem is well-posed and there is only one object $T^{N\times 1}$ that can be reconstructed for the acquisition data $R^{M\times 1}$.

If for one reason or another the number of measurements M becomes smaller than the number of unknowns N then $rank(\boldsymbol{A}) \leq min(M, N) = M < N$ and the reconstruction problem will be ill-posed. There are two common situations:

1) When the reception aperture does not cover the whole tomographic angle $\Omega_0 = 2\pi$.

2) When the reconstruction grid step is below $\lambda_{ac}/2$, i.e. when a sub-diffractional resolution is required.

In this chapter, we will try to achieve super-resolution with the model-based approach, i.e. we will deal with case (2).

5.4 State-of-the-art and objectives of this chapter

In PA imaging, the model-based approach was first introduced to palliate visibility artifacts in 3D photoacoustic tomography (PAT) [Wang et al., 2012; Liu et al., 2012; Buehler et al., 2011; Provost and Lesage, 2008; Meng et al., 2012; Dean-Ben et al., 2012; Han et al., 2017].

In PAT, volumetric reconstruction is achieved in multiple acquisitions by scanning the imaged object from different angles or in a single acquisition by using a receiver whose elements can capture acoustic waves emitted in many directions. When PA acquisitions are performed under different angles, not all the angles are usually accessible or scanning at many positions can be time-consuming. This lack of scanning angles results in specific artifacts in the reconstruction image when standard reconstruction methods, such as delay-and-sum beamforming/backprojection, are used. Artifacts related to spatial undersampling do also appear in single-shot imaging when transducer elements are placed more than $\lambda_{ac}/2$ apart. This problem is pertinent in 3D PAT where the number of elements is reduced due to technical limitations (see Chapter 6). It has been demonstrated that accompanied by additional priors on the imaged object model-based reconstruction can remove artifacts related to an incomplete set of scanning angles [Wang et al., 2012; Liu et al., 2012; Buehler et al., 2011; Provost and Lesage, 2008], a large spacing between transducer elements [Meng et al., 2012] or both [Dean-Ben et al., 2012; Han et al., 2017]. Fig. 5.3 shows how the model-based approach can be used to improve reconstruction results in limited-view 3D PAT [Wang et al., 2012].

In parallel to using model-based reconstruction to handle reconstruction artifacts in PAT, it was proposed to employ this approach to achieve super-resolution in US and PA imaging.

For example, in US imaging the vector R can be associated with the diffraction-

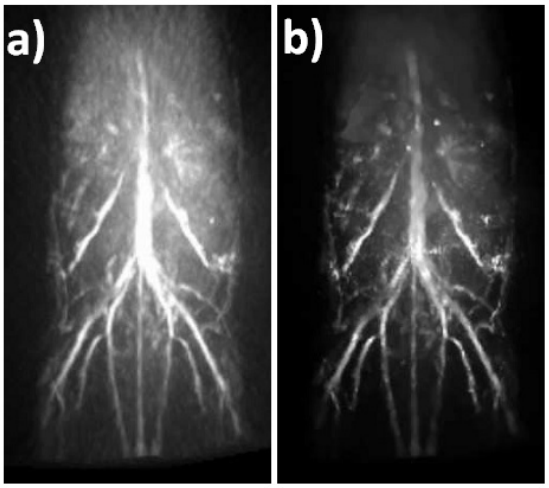

Fig. 5.3 Mean intensity projection renderings of 3D images of a mouse body reconstructed from the 180-view data with (a) a backprojection algorithm (b) model-based reconstruction [Wang et al., 2012].

limited envelope image while the propagation matrix $\boldsymbol{A}$ will contain a library of envelope PSFs [Morin et al., 2012; Zhao et al., 2016; Shu et al., 2018]. To improve the resolution further, it has also been proposed to apply model-based reconstruction to fluctuation data. The method called sparsity-based ultrasound super-resolution hemodynamic imaging (SUSHI) [Bar-Zion et al., 2018] relies on sparsity-based regularization with the vector R representing the time variance of the beamformed image and the matrix $\boldsymbol{A}$ consisting of PSFs raised to the 2nd power.

In PA imaging, some groups reported [Hojman et al., 2017; Murray et al., 2017] to achieve super-resolution in model-based reconstruction involving joint support recovery, i.e. the fact that under M_s random optical speckle illuminations PA signals can be generated only at the points belonging to the imaged object. In this case, the vector R contains the results of all M_s acquisitions. The joint support can be taken into account by using a mixed L1/L2 term [Murray et al., 2017] as the regularization term in minimization (5.3) or by reconstruction based on the multiple sparse Bayesian learning (M-SBL) algorithm [Hojman et al., 2017]. It was shown that in terms of resolution model-based reconstruction outperforms fluctuation-based reconstruction [Murray et al., 2017] and Richardson-Lucy deconvolution [Hojman et al., 2017; Murray et al., 2017]. To provide an example, the MSB-L approach is compared with other reconstruction techniques in Fig. 5.4. Despite these promising results, using optical speckle illuminations in clinical imaging is challenging as the small fluctuation signal can be difficult to distinguish on the strong background when imaging is performed at depths exceeding several millimeters (see section 1.4).

In this Chapter we obtain super-resolution via the model-based approach without relying on speckle illuminations. We first achieve super-resolution using only one con-

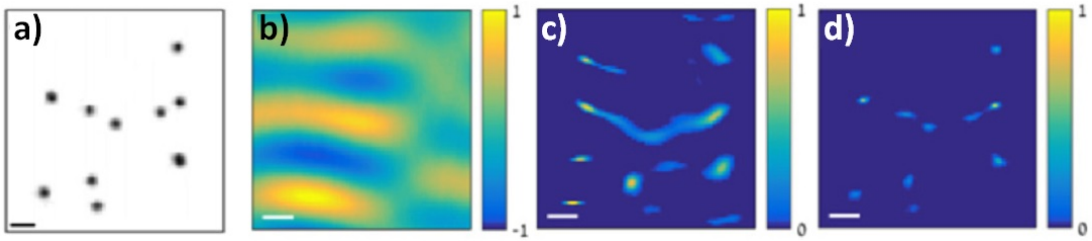

Fig. 5.4 Model-based reconstruction leads to super-resolution of point targets. (a) Ground truth. (b) Standard beamforming reconstruction. (c) Richardson-Lucy deconvolution. (d) Model-based reconstruction (M-SBL algorithm) [Hojman et al., 2017].

ventional PA acquisition (i.e. in single-shot imaging). For this data, we compare different regularization
schemes and reconstruction images resulting from RF and BF data. Then, we try to estimate the resolution limit of sparsity-based reconstruction. Afterwards, we test a SUSHI-like approach in photoacoustics by applying sparsity-based reconstruction to variance data. The last part of this Chapter is devoted to a theoretical investigation of sparsity-based reconstruction. In this last part, we study how the reconstruction result depends on the regularization parameter and on the non-negativity constraint. In this context, we also discuss reliability and limitations of sparsity-based reconstruction. Finally, we discuss positivity-based reconstruction in the noiseless case.

5.5 A proof-of-principle experiment

In a proof-of-principle experiment, we sought to obtain super-resolution in single shot PA imaging. As in the previous chapters, we will perform cross-sectional imaging of a microfluidic sample consisting of five parallel channels separated by a sub-diffractional distance. Then, we will try to reconstruct the imaged cross-section using different regularization schemes applied to RF and BF data.

5.5.1 Materials and methods

5.5.1.1 Measurement protocol

The sample to image consists of five identical parallel microfluidic channels with a rectangular cross-section (Fig. 5.5). To perform cross-sectional imaging, the microchannels are placed perpendicularly to the imaging plane XZ of a linear transducer array (type L22-8) at the US probe elevational focus distance z_f = 15 mm. In this plane, each channel is h_{ch} = 50 μm high and w_{ch} = 40 μm wide, the center-to-center distance between neighbouring channels being L_{cc} = 125 μm. To provide a good PA contrast the sample is filled with absorbing liquid (Patent Blue V). For more details on fabrication of the microfluidic sample the reader is referred to Chapter 2.

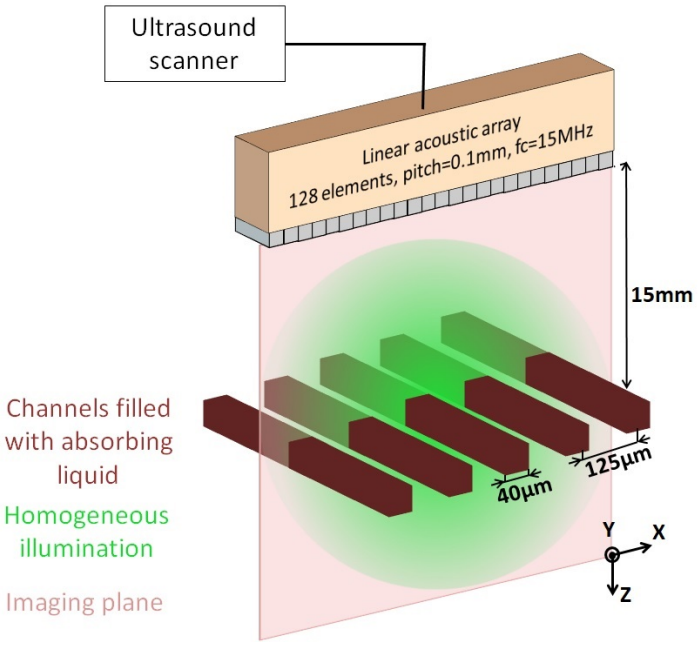

Fig. 5.5 The sample to image consists of five identical parallel microchannels filled with absorbing liquid. The sample is placed at z_f = 15 μm from the US probe, each channel is $w_{ch} = 40$ μm wide, the interchannel center-to-center distance is L_{cc} = 125 μm. The sample is illuminated by a single laser pulse and the resulting PA signals are received by the US probe connected to the acquisition electronics.

A schematic of the experimental setup is shown in Fig. 2.1. In the experiment, PA signals were acquired on illuminating the sample with a single laser pulse ($\lambda_{laser} = 532$ nm, fluence = 3 mJ/cm^2). To apply model-based reconstruction, we also acquired the PSF of the imaging system, the full width at half maximum (FWHM) of the BF-PSF being $\Delta X = 154$ μm, $\Delta Z = 139$ μm (see section 2.5). For any details on the experimental equipment the reader is referred to Chapter 2.

Fig. 5.6 shows the acquired single-shot RF data. The laser noise was removed by subtracting the average value for each line of the RF frame (see section 2.2). The horizontal line appearing at $t = 9.35$ μs corresponds to the signal from the sample surface. The signal-to-noise ratio (SNR) calculated as the ratio between the maximum of the RF signal and the noise variance computed over a signal-free region of the RF data is SNR=$max(RF)/\sigma_n \approx 4000/30 = 133$.

The result of standard beamforming reconstruction is illustrated in Fig. 5.7. Being separated by less than the FWHM of the PSF (L_{cc} = 125 μm ¡ 154 μm), the microchannels appear indistinguishable.

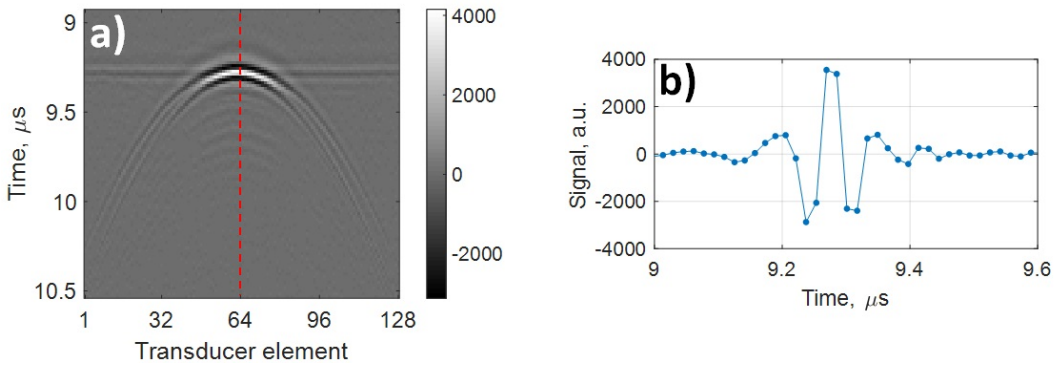

Fig. 5.6 (a) RF data acquired in single shot imaging of the microchannels filled with absorbing liquid. The horizontal line appearing at $t = 9.35\ \mu s$ corresponds to the signal from the sample surface. (b) The signal acquired by the 64th transducer element, designated with the dashed line in (a).

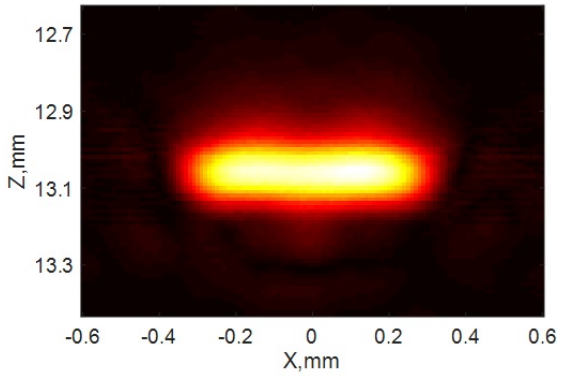

Fig. 5.7 Standard beamforming reconstruction of the imaged cross-section of the five parallel microchannels separated by $L_{cc} = 125\ \mu m$. Being separated by less than the FWHM of the PSF ($\Delta X = 154\ \mu m$), the microchannels appear indistinguishable.

5.5.1.2 Reconstruction methods

We first performed reconstruction based on the acquired RF data and then based on the BF data.

The RF-based reconstruction involves the following forward model (Eq. (5.13)):

$$R_{RF} = \boldsymbol{A}_{RF} T_0,$$

where $R_{RF}^{M\times 1}$ is the vector representation of the RF frame, $\boldsymbol{A}_{RF}^{M\times N}$ is the propagation matrix, $T_0^{N\times 1}$ is the imaged object discretized on the reconstruction grid.

The number N depends on the reconstruction zone that can be chosen based on the region corresponding to the unresolved structure of the sample on the diffraction-limited beamforming image. The beamforming image is shown in Fig. 5.7. So, the size of the reconstruction zone is about $750\ \mu m \times 150\ \mu m$. By discretizing the imaged object on a $L_{cc}/10 = 12.5\ \mu m$ grid, one obtains $N = 750 \times 150/(12.5)^2 = 720$. The number

M is determined by the number N_{el} of transducer elements and the number N_t of time samples in the RF frame, the latter being reduced using the approach demonstrated in Appendix 2. So, $M = N_{el} \times N_t = 128 \times 37 = 4736$. The propagation matrix $\boldsymbol{A}_{RF}$ is constructed using only one PSF acquisition in the imaging zone. The approach is described in detail in section 5.2.3. Although $M > N$, calculating the rank of the matrix $\boldsymbol{A}_{RF}$ gives $rank(\boldsymbol{A}_{RF}) = 346 < N$.Hence, the inverse problem is ill-posed, which could be expected as the reconstruction grid is chosen with a sub-diffractional step.

The BF-based reconstruction involves the following forward model (Eq. (5.15)):

$$R_{BF} = \boldsymbol{A}_{BF} T_0,$$

where $R_{BF}^{M\times 1}$ is the vector representation of the standard beamforming image, $\boldsymbol{A}_{BF}^{M\times N}$ is the propagation matrix, $T_0^{N\times 1}$ is the imaged object discretized on the reconstruction grid.

The number $N = 720$ is determined by discretization of the object on the reconstruction zone and is the same as for the RF-based reconstruction. The number M is determined by the number of points in the beamforming zone. Each point source in the reconstruction zone can be associated with a PSF in the beamforming zone. As the PSF has a certain size (PSF FWHM being $\Delta X = 154\ \mu m$, $\Delta Z = 139\ \mu m$), the beamforming zone should be chosen larger than the reconstruction zone (see Appendix 2). So, we choose the beamforming zone of $1000\ \mu m \times 500\ \mu m$. The sampling frequency of the acquisition machine being $f_s = 4f_c$ ($f_c = v_s/\lambda_{ac}$ is the central frequency of the US probe), the minimal beamforming grid step is $\lambda_{ac}/4 \approx 25\ \mu m$. Thus, $M = 1000 \times 500/25^2 = 800$. Again, although $M > N$, calculating the rank of the matrix $\boldsymbol{A}_{BF}$ gives $rank(\boldsymbol{A}_{BF}) = 324 < N$. So, the inverse problem is again ill-posed.

To solve the ill-posed reconstruction problem for the RF and BF data, we tested several approaches:

- Moore-Penrose pseudoinverse with simple truncation weighting function via Eq. (5.4) and (5.6).
- Tikhonov regularization via Eq. (5.4) and (5.7).
- Positivity-based reconstruction via minimization (5.3 with $\alpha = 0$ and the non-negativity constraint.
- Sparsity-based reconstruction via minimization (5.3) without the non-negativity constraint.

The regularization parameter α for Tikhonov regularization and the thresholding singular value s_0 for pseudoinverse reconstruction were estimated using the L-curve

method [Hansen, 1999]. To do it, we first plotted the L2 norm of the reconstructed object $||\hat{T}_{L2}||_2^2$ as a function of the norm of the residual $||R - \boldsymbol{A}\hat{T}_{L2}||_2^2$ in logarithmic scale for a series of values of the sought parameter. Afterwards, the parameter corresponding to the corner of the obtained curve was taken. In sparsity-based reconstruction the regularization parameter α was determined heuristically by comparing visually the reconstructed object with the real sample.

When the non-negativity constraint was not applied at each iteration of the algorithm, all negative values on the final reconstruction image were replaced with zeros.

Minimization (5.3) is performed using the FISTA algorithm. The reader is referred to Appendix 2 for more details on the minimization algorithm.

5.5.1.3 Results

Experimental results obtained with model-based reconstruction applied to RF data are shown in Fig. 5.8. Moore-Penrose pseudoinverse, Tikhonov regularization and positivity-based reconstruction are all unable to recover the object structure. In contrast, L1-based regularization provides a super-resolved image with five well separated regions.

First, both Moore-Penrose pseudoinverse and Tikhonov regularization lead to a smooth profile that is far from the true object structure. In these techniques noise suppression is achieved by ignoring a number of highly (spatially) oscillating singular vectors of the propagation matrix $\boldsymbol{A}$. The number of singular vectors to ignore is determined by the thresholding singular value σ_0 in Eq. (5.6) for Moore-Penrose pseudoinverse and the regularization parameter α in Eq. (5.7) for Tikhonov regularization. However, the discarded singular vectors do encode some object features. So, by unavoidably discarding singular vectors to suppress noise, Moore-Penrose pseudoinverse and Tikhonov regularization fail to reconstruct the fine structure of the imaged object.

Then, positivity-based reconstruction leads to an image with point-like artifacts. As mentioned in section 5.1.3.2 there is no evidence that the non-negative constraint can lead to the correct object.

Finally, L1 - based regularization provides super-resolution. Apparently, on the L1 reconstruction image the microchannels appear as points since the reconstruction of the full channel dimensions would not provide the minimum-L1-norm solution. This pointy structure was the closest to the imaged object for α varying from zero to the value at which the reconstructed object completely disappears. Importantly, it was observed that the reconstructed object is highly dependent on α. In particular, at small α a series of unregularized solutions was observed, the number of non-zero points of the object decreasing rapidly with the increase of α. Then, the regularized solution shown in Fig. 5.8d appeared. Afterwards, the object sparsity (or the number of reconstructed channels) decreased gradually with the increase of α until the reconstructed object com-

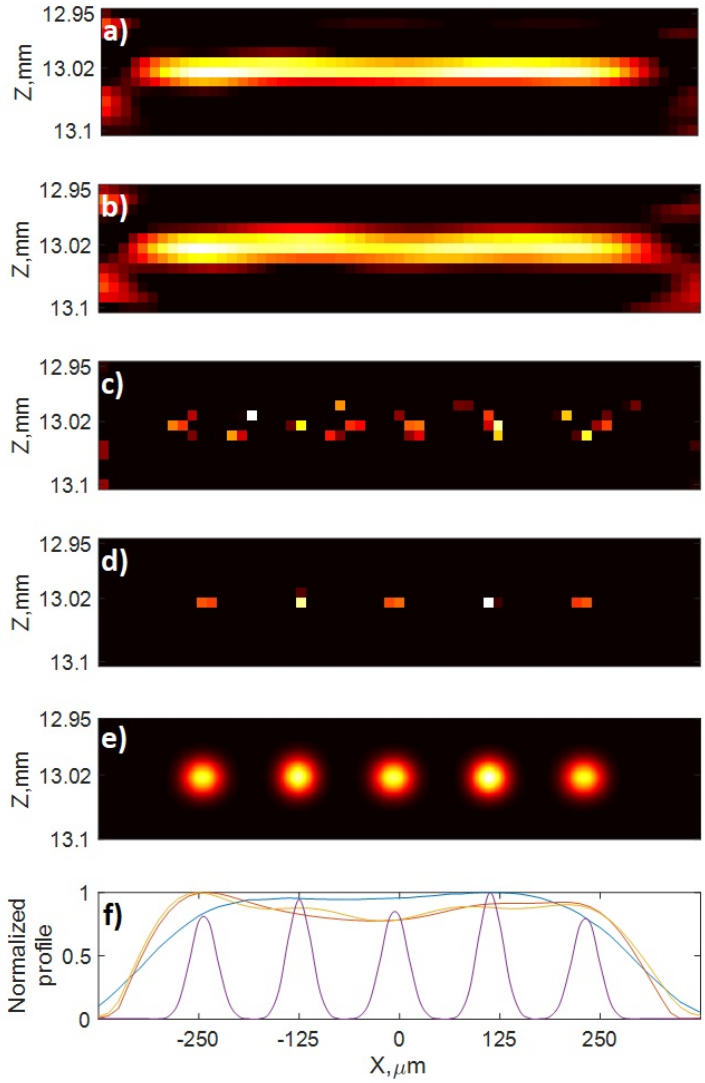

Fig. 5.8 Model-based reconstruction for five parallel microfluidic channels (RF data). (a) Moore-Penrose pseudoinverse image. (b) Tikhonov regularization image, very similar to (a). (c) Positivity-based reconstruction. (d) L1 regularization image. The reconstruction recovers five distinct regions corresponding to the microfluidic channels. (e) Reconstruction image (d) after smoothing out with a 2D spatial Gaussian filter (σ_g = 12.5 μm) and interpolating on a 3 μm grid. (f) Normalized amplitude profiles. Blue: envelope image (Fig. 5.7); Red: Pseudoinverse image (a); Yellow: Tikhonov regularization image (b); Violet: L1 regularization image (e).

pletely disappeared. So, without knowing the imaged object *a priori* we would not have been able to make the right choice of the regularization parameter and obtain a correct reconstruction.

To correct for the pointy appearance of the sources caused by the nature of the L1 - based solution, the point-like image in Fig. 5.8d was convolved with a 2D gaussian function with a kernel size corresponding to one reconstruction point (σ_g = 12.5 μm). On the resulting lateral profile (Fig. 5.8f, violet) the average distance between neigh-

bouring peaks corresponds to the interchannel separation $L_{cc} = 125\ \mu m$.

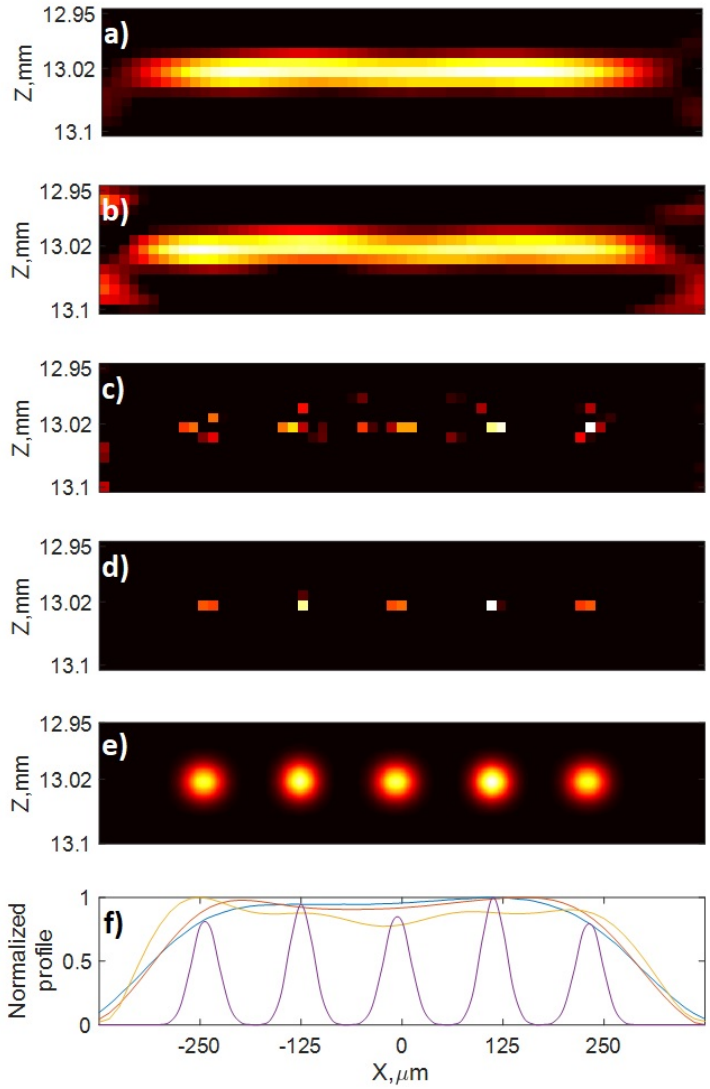

Fig. 5.9 Model-based reconstruction for five parallel microfluidic channels (BF data). The results are similar to those in RF-based reconstruction (Fig. 5.8). (a) Moore-Penrose pseudoinverse image. (b) Tikhonov regularization image. (c) Positivity-based reconstruction. (d) L1 regularization image. (e) Reconstruction image (d) after smoothing out with a 2D spatial Gaussian filter (σ_g = 12.5 μm) and interpolating on a 3 μm grid. (f) Normalized amplitude profiles. Blue: envelope image (Fig. 5.7); Red: Pseudoinverse image (a); Yellow: Tikhonov regularization image (b); Violet: L1 regularization image (e).

Experimental results obtained with model-based reconstruction applied to BF data are shown in Fig. 5.9. It can be clearly seen that they are very close to those obtained with RF data (Fig. 5.8). However, one may suppose that the positivity-based reconstruction leads to the right object that can be recognized in the reconstruction image despite the presence of noise. We also note that thanks to the smaller size of the matrix $\boldsymbol{A}$ and the vectors X and Y, computation burden in BF-based reconstruction is reduced and the reconstruction time is shorter than in RF-based reconstruction.

5.5.1.4 First conclusions

We demonstrated experimentally that sparsity-basedreconstruction can provide super-resolution in acoustic-resolution photoacoustic imaging. With other regularization schemes, such as Moore-Penrose pseudo-inverse, Tikhonov regularization and positivity-based reconstruction, super-resolution was not achieved. We also showed that regularization provides very similar results when applied to RF or BF data. We note that working on BF data may be preferable as in this case the matrix-based reconstruction is faster. A number of important questions still have to be addressed:

1. What is the ultimate resolution that can be reached in sparsity-based reconstruction ?

2. Is there a way to choose the regularization parameter without *a priori* knowledge of the object?

3. For a good SNR, would the positivity-based reconstruction provide the right object?

In the following sections, we will try to answer questions (1)-(3).

5.6 Two-channel case to further investigate the resolution limit

In this section, we shall investigate the resolution limit of sparsity-based reconstruction. We define the resolution limit as the minimal lateral distance ΔX at which two point sources lying at the same depth Z can be separated in reconstruction.

To this end, in experiments and then in simulations we reconstruct different cross-sections of two approaching channels lying in the XY plane. In experiments, the minimal center-to-center separation is 75 μm due to fabrication limitations (see section 2.6). So, we choose the probe L7-4 which has a coarser resolution (PSF FWHM ΔX = 389 μm) compared to the probe L22-8 (PSF FWHM ΔX = 154 μm) to reach the sub-diffractional regime more easily with the microfluidic sample. To reduce the computational burden, we apply model-based reconstruction not to RF but to BF data.

5.6.1 Simulations of RF data : method

In order to remove experimental uncertainties and focus on the fundamental limitations and principles of the methods in question we complement our experimental investigations with numerical simulations. The simulated data is generated on the following grounds:

- All the transducer elements are point sources;

- The emitted PA wave is the same for all imaged point sources, the detected signals are identical in amplitude and spectrum, but they are shifted in time according to the distance between each imaged source and each transducer element;
- The detected signals have the central frequency and bandwidth corresponding to those used in experiments, with the same sampling frequency as in experiments.

5.6.2 Single shot/mean image

5.6.2.1 Experiments

The sample to image consists of two approaching microfluidic channels lying in the plane XY at z_f = 25 mm from the US transducer (Fig. 5.10). In the plane XZ, each channel is $w_{ch} = 40\ \mu m$ wide and $h_{ch} = 50\ \mu m$ high, the interchannel center-to-center distance ΔX varies between 80 μm and 360 μm.

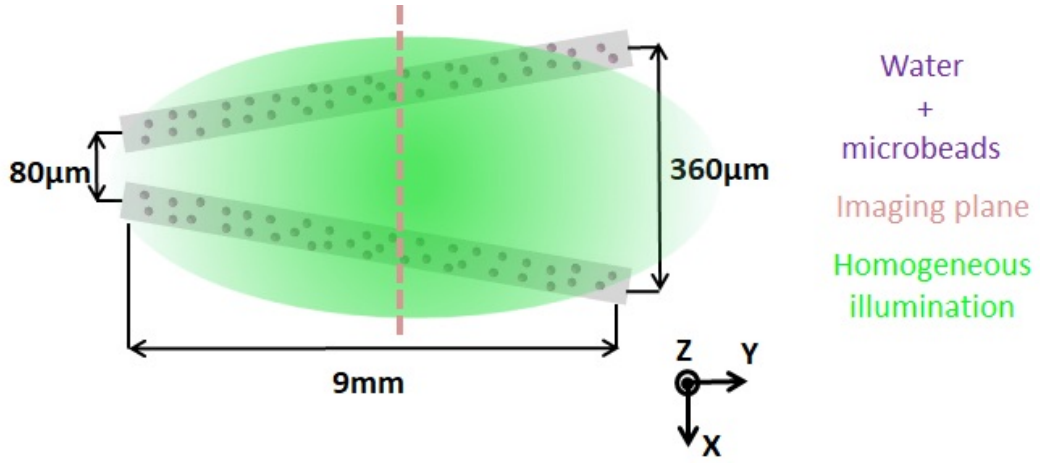

Fig. 5.10 Several cross-sections (in the XZ plane) of two approaching microchannels are imaged by moving the US probe along the Y axis. The sample is place at z_f = 25 mm from the US probe, each channel is $w_{ch} = 40\ \mu m$ wide and $h_{ch} = 50\ \mu m$ high, the interchannel center-to-center distance varies between 80 μm and 360 μm. At each laser shot PA signals emitted by the microbeads crossing the imaging plane XZ are captured by the linear transducer array (type L7-4) connected to the acquisition electronics.

A schematic of the experimental setup is shown in Fig. 2.1. In the experiment, a flow of spherical absorbing 10-μm diameter beads was induced through the channels. We used a flow of beads instead of a homogeneous absorbing liquid in order to be able to use the same dataset to test a SUSHI-like reconstruction approach combining fluctuation-based reconstruction with model-based reconstruction (see section 5.6.3). At each laser shot ($\lambda_{laser} = 532$ nm, fluence = 3 mJ/cm^2) the PA signals from the beads in the imaging plane were registered by a linear transducer array (type L7-4). By moving the US probe along the Y axis, several cross-sectional images were obtained

for interchannel distances ranging from 80 μm to 360 μm. For more information about the acquisition equipment the reader is referred to Chapter 2.

The suspension of microbeads was prepared according to the following recipe: 12.5% of the initial 5% microbeads water suspension (Microparticles GmbH, Berlin, Germany), 0.025% of a buffer solution (TWEEN20, Sigma-Aldrich Corp., St. Louis, MO, USA), 19.6% of a density gradient medium (OptiPrep, ProteoGenix SAS, Schiltigheim, France), and 67.9% of water. The buffer solution was used to avoid microbeads sticking to each other whereas the density gradient medium was added to prevent microbeads from precipitating and getting stuck inside the pump system.

In total, 20,000 acquisitions were made for each position of the probe. In each position, the acquired data was beamformed and averaged over time. In each beamforming image the SNR computed as the maximum of the signal over the standard deviation of noise in a signal-free region was SNR $\approx 7000/2 = 3500$.The size of the propagation matrix $\boldsymbol{A}_{BF}^{M\times N}$ was M=216, N=1107. The rank of the propagation matrix $\boldsymbol{A}_{BF}$ was $rank(\boldsymbol{A}_{BF}) = 206 < N$.

To apply model-based reconstruction, we also acquired a PSF corresponding to one isolated microchannel (see section 2.5). The PSF FWHM was $\Delta X = 389\ \mu m$, $\Delta Z = 418\ \mu m$.

Projections of XZ reconstruction images onto the X axis obtained for different distances ΔX between the channels are combined in Fig. 5.11. The channels remain distinguishable down to 80 μm (the PSF lateral FWHM being ΔX = 398 μm) which was the minimal center-to-center distance available on the microfluidic sample.

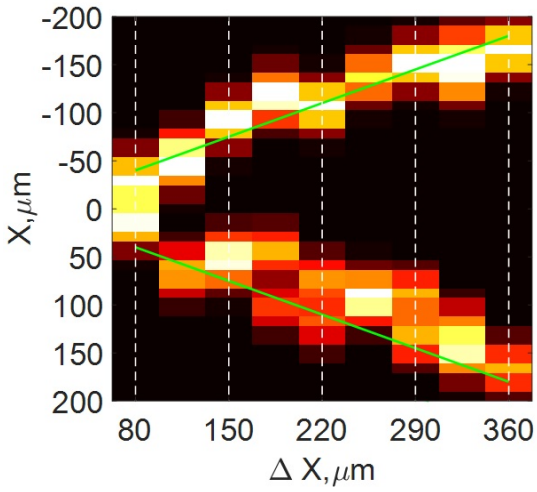

Fig. 5.11 Sparsity-based reconstruction for two approaching channels (experiment, BF-based, mean data): projections of XZ reconstruction images onto the X axis, obtained for different distances ΔX between the channels. The green lines designate theoretical separation.

5.6.2.2 Noise-free simulations

As in the experiment all the imaged cross-sections were properly reconstructed, we had to perform numerical simulations for shorter interchannel distances to find the true limit of sparsity-based reconstruction. To look for the best achievable resolution, the simulations were performed without adding noise.

The simulation results are shown in Fig. 5.12. It can be noticed that the channels are resolved for $\Delta X > 22\ \mu m$. The corresponding regularization parameter $\alpha = \alpha_{opt}$ was the same for all interchannel distances. Below $\alpha = \alpha_{opt}$ the channels were poorly resolved as the regularization term was too low for the minimization algorithm to work properly (see Eq. (5.29)). For $\alpha > \alpha_{opt}$ the channels appeared closer than they were on the sample as some measurement data was ignored since the fidelity term was allowed to be relatively high. The numerically determined resolution limit can be explained by the PSFs of the approaching channels getting more and more correlated when the channels become closer. Each PSF corresponding to a point in the discretized imaging zone is encoded as a column of the propagation matrix $\boldsymbol{A}$. Then, at the imaging depth $z = z_f$ the correlation between columns corresponding to PSFs separated by $\Delta X = 20\ \mu m$ is $C = 0.87$ whereas the correlation between columns related to PSFs separated by $\Delta X = 100\ \mu m$ is $C = 0.24$. So, the PSFs corresponding to the approaching channels get so similar to each other that the reconstruction algorithm is unable to distinguish them, which leads to a faulty reconstruction.

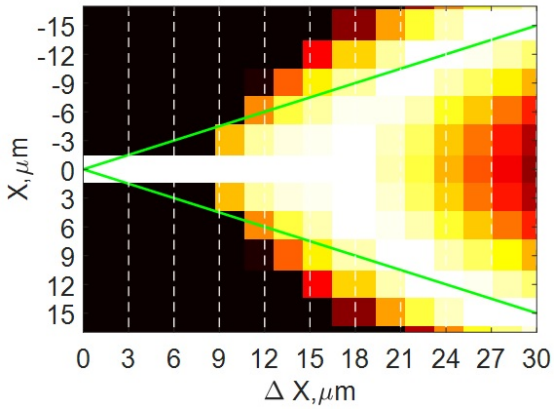

Fig. 5.12 Sparsity-based reconstruction for two approaching channels (simulations, BF-based, mean data): projections of XZ reconstruction images onto the X axis, obtained for different distances ΔX between the channels. The green lines designate theoretical separation.

5.6.2.3 Conclusion/discussion

We demonstrated experimentally that in sparsity-based reconstruction two point sources could be resolved down to 80 μm which is about four times smaller than the FWHM of

the PSF ($\Delta X = 389\ \mu m$). In simulations, we were able to model sources separated by smaller distances, with a perfectly known propagation model and without any additional noise. As a result, the corresponding resolution limit was about $24\ \mu m$ for the same PSF FWHM as in the experiment ($\Delta X = 389\ \mu m$). This figure is apparently related to the available numerical precision. It still remains unclear whether a similar resolution could be obtained experimentally even at a very high SNR since in practice the propagation model is not perfectly known. In addition, the reported resolution limits would probably not have been obtained if the SNR were lower. So, additional studies are needed to determine the effect of model imperfection and the SNR on the resolution limit.

5.6.3 Fluctuation-based+model-based imaging

In fluctuation-based imaging the super-resolved image is obtained by calculating a certain statistical property over each pixel of a stack of beamformed images (see Chapter 4). In particular, it was demonstrated by Chaigne et al. [Chaigne et al., 2016] that variance-based reconstruction can lead to a $\sqrt{2}$ resolution improvement in PA imaging. In the same study, it was shown that the result of fluctuation-based imaging may be additionally improved by applying L2 reconstruction to the variance image. The corresponding forward model can be expressed as:

$$R_{BF}^{VAR} = \boldsymbol{A}_{BF}^{VAR} T_0, \tag{5.18}$$

where the vector R_{BF}^{VAR} represents the variance beamforming image (pixelwise time variance calculated over a set of beamformed images) and $\boldsymbol{A}_{BF}^{VAR}$ is the elementwise matrix product $\boldsymbol{A}_{BF}^{VAR}(i,j) = \boldsymbol{A}_{BF}(i,j)\boldsymbol{A}_{BF}(i,j)$.

Later on, it was demonstrated that L1 (sparsity-based) reconstruction applied to the variance image can lead to super-resolution in US imaging [Bar-Zion et al., 2018]. Fig. 5.13 shows some *in vivo* results obtained for a rabbit kidney in [Bar-Zion et al., 2018]. It can be seen that the SUSHI approach (sparsity-based reconstruction applied to the variance image) can resolve close blood vessels which appear indistinguishable when other reconstruction techniques are applied.

Inspired by [Bar-Zion et al., 2018] we tried to obtain super-resolution in PA imaging by applying sparsity-based reconstruction to the variance beamforming image. We investigated the resolution limit of the proposed technique in experiments and in simulations using the model of two approaching channels.

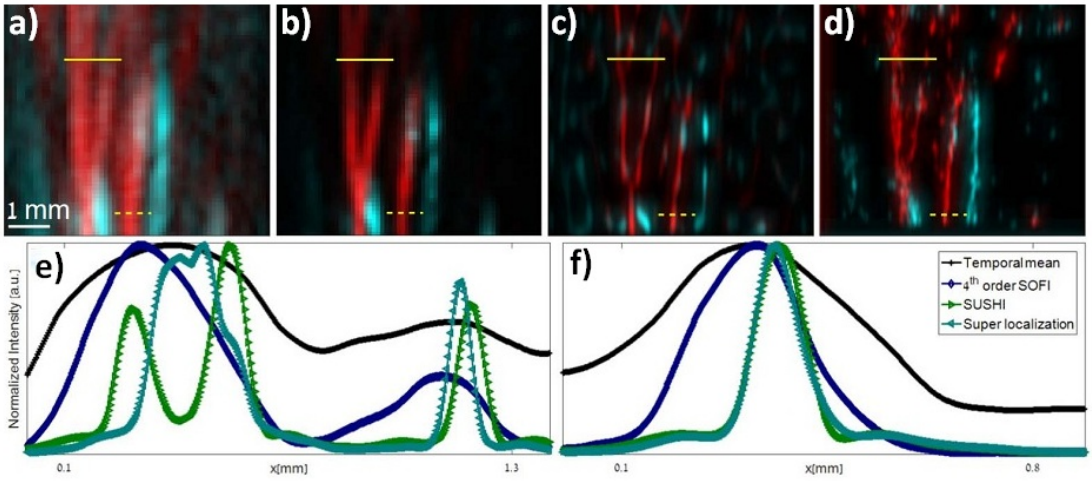

Fig. 5.13 Experimental reconstruction of blood vessels in a rabbit kidney [Bar-Zion et al., 2018]. (a) Mean beamforming image. (b) SOFI image (c) SUSHI image (d) super-localization result. (e) and (f) Intensity profiles measured along the solid and dashed yellow lines on (a)–(d). (e) shows that in high density areas (e.g., bifurcations), SUSHI is superior, while in low density areas [e.g., isolated vessel in (f)], SUSHI exhibits comparable spatial resolution to super-localization.

5.6.3.1 Experimental protocol

The experimental protocol has been described in section 5.5.2.1. To perform variance-based reconstruction, for each imaged cross-section we computed the variance beamforming image. On each variance image the SNR calculated as the maximum of the signal over the standard deviation of noise in a signal-free region was SNR$\approx 1.2 \times 10^6/756 = 1600$. The size of the propagation matrix $\boldsymbol{A}_{BF}^{VAR}$ was M=216, N=1107. The rank of the propagation matrix $\boldsymbol{A}_{BF}^{VAR}$ was $rank(\boldsymbol{A}_{BF}^{VAR}) = 216 < N$.

5.6.3.2 Experimental results

Projections of XZ reconstruction images obtained for different distances ΔX between the channels are combined in Fig. 5.14. As in the mean-based reconstruction (Fig. 5.11), the channels remain distinguishable down to 80 μm (the PSF lateral FWHM being ΔX = 398 μm) which was the minimal center-to-center distance available on the microfluidic sample.

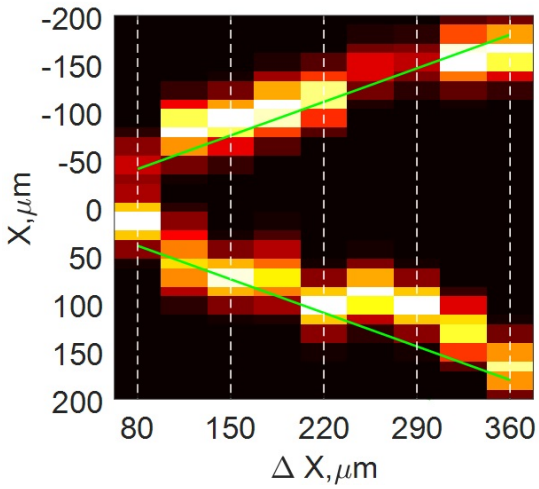

Fig. 5.14 Sparsity-based reconstruction for two approaching channels (experiment, BF-based, variance data): projections of XZ reconstruction images onto the X axis, obtained for different distances ΔX between the channels. The green lines designate theoretical separation.

5.6.3.3 Simulation results

As in single-shot imaging, we performed noise-free simulations to determine the fundamental limit of the technique. The simulation results are shown in Fig. 5.15. It can be noticed that the channels are resolved for $\Delta X \geq 16\ \mu m$. So, the resolution improvement is about $22/16 \approx \sqrt{2}$ compared to sparsity-based reconstruction applied to the mean image (section 5.5.2.2). It is to be noted that in fluctuation-based super-resolution imaging the variance beamforming image also demonstrates a $\sqrt{2}$ resolution improvement with respect to the mean image [Chaigne et al., 2016].

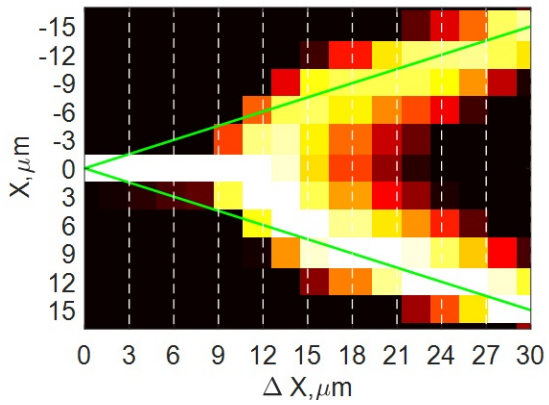

Fig. 5.15 Sparsity-based reconstruction for two approaching channels (simulations, BF-based, variance data): projections of XZ reconstruction images onto the X axis, obtained for different distances ΔX between the channels. The green lines designate theoretical separation.

5.6.3.4 Conclusion/discussion

We showed that sparsity-based reconstruction applied to the variance image leads to super-resolution in PA imaging. Being a combination of two other super-resolution techniques, the applied method improves the resolution of each of them. As a result, the maximal resolution is only about $\sqrt{2}$ times better than in classical sparsity-based reconstruction (16 μm beside 22 μm). So, if Fig. 5.13 from [Bar-Zion et al., 2018] was complemented with the result of sparsity-based reconstruction applied to the mean image the difference between SUSHI and classical sparsity-based reconstruction would probably be merely noticeable. It should be kept in mind that a certain number of acquisitions should be made to obtain the variance image and the $\sqrt{2}$ gain in spatial resolution may cost too much in terms of temporal resolution.

5.6.4 Some insights into performance and mechanism of model-based reconstruction

In this section we will perform computer simulations to better understand model-based reconstruction in the context of super-resolution PA imaging. We restrict our analysis to reconstruction based on the following minimization:

$$\hat{T}_0 = \underset{T}{\operatorname{argmin}}\{||R_{RF} - \boldsymbol{A}_{RF}T||_2^2 + \alpha^*||T||_1\}. \tag{5.19}$$

When sparsity-based reconstruction ($\alpha \neq 0$) is considered, the non-negativity constraint $T(i) \geq 0$ is not used unless the opposite is stated.

When the positivity-based reconstruction is considered, the non-negativity constraint is imposed but the regularization parameter α is equal to 0.

For the rest of this section we will suppress the indices of R_{RF} and $\boldsymbol{A}_{RF}$.

In the first part of the section, we shall study sparsity-based reconstruction. In particular, we will investigate how the reconstruction result depends on the regularization parameter. As noted in section 5.1.2, regularization should suppress the noise and choose a solution which is close to the imaged object. So, first we consider noise suppression (in the absence of object) afterwards we discuss object reconstruction (in the absence of noise) and then we analyze object reconstruction in the presence of noise, which is close to real imaging conditions. In the first part, we will also determine the role of the non-negativity constraint when it complements sparsity-based reconstruction. We will conclude this part by discussion on the choice of the regularization parameter, giving an answer to question (2) of section 5.4.1.4.

In the second part of the present section we shall determine whether in the noiseless case the correct object can be provided by positivity-based reconstruction (question (3) of section 5.4.1.4). To do it, we will apply positivity-based reconstruction to simulation data for the two approaching channels. In these simulations, we will also determine the

resolution limit of positivity-based reconstruction.

The simulation data was generated on the following grounds:

- All the transducer elements are point sources;
- The emitted PA wave is the same for all imaged point sources, the detected signals are identical in amplitude and spectrum, but they are shifted in time according to the distance between each imaged source and each transducer element;
- The detected signals have a central frequency and bandwidth corresponding to those used in experiments, with the same sampling frequency as in experiments;
- When noise is considered, gaussian noise with a zero mean and the rms of $\sigma_n = 30$ is added to the detected signals. Such noise resembles the noise produced by the acquisition electronics used in our experiments (see section 2.3).

5.6.5 Mechanism and performance of sparsity-based reconstruction

To study sparsity-based reconstruction, we generated PA data for a modelled object consisting of $K = 5$ points separated by $L_{cc} = 125\ \mu m$. The propagation matrix $\boldsymbol{A}^{M\times N}$ (M = 4608, N = 765), size of the reconstruction zone (550 μm × 200 μm), frequency and bandwidth of the received signals (corresponding to the probe L22-8) as well as other reconstruction and imaging parameters are close to the experiment with five parallel microchannels, the maximum of the RF signal related to a single reconstruction point being $A_1 = 15$. When noise is considered, white Gaussian noise with controlled rms value is added to each detected signal.

5.6.5.1 Renormalization

Let us consider the fidelity term $J_f = ||R - \boldsymbol{A}T||_2^2$ in minimization (5.19). When the vector $R^{M\times 1}$ is acquired in the absence of imaged object ($T = 0$), it contains only noise. If the noise rms is σ_n then $||R||_2^2 \approx M\sigma_n^2$. Therefore, the fidelity term J_f is approximately equal to $M\sigma_n^2$ when the object is perfectly reconstructed. So, it is convenient to introduce

$$J_f^* = ||R - \boldsymbol{A}T||_2^2/(M\sigma_n^2) = J_f/(M\sigma_n^2) \tag{5.20}$$

and then consider reconstruction only around $J_f^* = 1$.

One can also consider the normalized regularization parameter

$$\alpha^* = \alpha/(M\sigma_n^2). \tag{5.21}$$

In this case, minimization (5.19) will be equivalent to minimization (5.22):

$$\hat{T}_0 = \underset{T}{\text{argmin}}\{J_f^* + \alpha^* ||T||_1\}. \tag{5.22}$$

5.6.5.2 Reconstruction in presence of noise only (no object)

Let us consider the vector R which contains only noise. In this case the reconstructed object T will also contain only noise. Simulation curves illustrated in Fig. 5.16 show that more and more noise in T is removed when the regularization parameter increases. First, even at very small values of α^* about 98% of noise energy is already rejected. This substantial noise reduction is due to the matrix $\boldsymbol{A}$ being considerably structured. Then, for high values of α^* the fidelity term $J_f^* = ||R - \boldsymbol{A}T||_2^2/(M\sigma_n)$ is close to one (the norm $||T||_1$ approaching zero), which means that all noise is suppressed.In addition, it can be noticed that the non-negativity constraint leads to the noise being removed more rapidly with the growth of α^*.

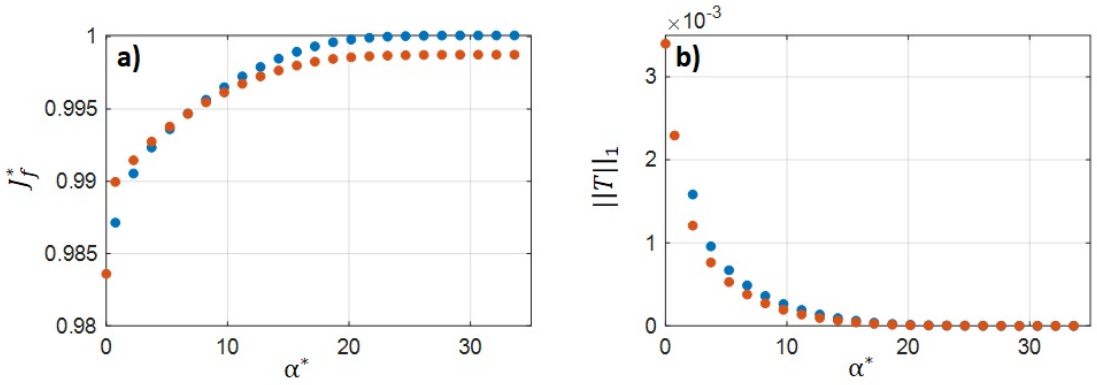

Fig. 5.16 J_f^* term (a) and $||T||_1$ norm (b) computed by minimizing Eq. (5.22) with (red dots) and without (blue dots) the non-negativity constraint. The measurement vector R contains only gaussian noise with $\sigma_n = 30$.

5.6.5.3 Reconstruction of an object with no noise

Let us consider the following 1D minimization problem ($r, a, t \in \mathbb{R}^1$):

$$t = \underset{t}{\text{argmin}}\{||r - at||_2^2 + \alpha||t||_1\} \tag{5.23}$$

The L1 norm and the fidelity term J_f corresponding to the solution t to minimization problem (5.23) can easily be found (the number of sources $K = 1$):

$$||t||_1 = -\frac{1}{2a^2}K\alpha + \frac{r}{a}K. \tag{5.24}$$

$$J_f = \frac{1}{4a^2}K\alpha^2. \tag{5.25}$$

It should be noted that L1 norm (5.24) is a linear function of αthat attains zero at

$$\alpha_e = 2ra. \tag{5.26}$$

Below, we will show that if sparsity-based regularization leads to the correct object reconstruction, Eq. (5.24)-(5.26) correspond well to minimization problem (5.19) when K is the object sparsity (number of non-zero points) and the following substitutions for the variables a and r are applied:

$$a^2 = E_{PSF}, \tag{5.27}$$

with $E_{PSF} \approx \frac{1}{N}\sum_{i=1}^{M}\sum_{j=1}^{N}\boldsymbol{A}(i,j)\boldsymbol{A}(i,j)$ being the average energy of the RF-PSF;

$$r = \frac{A_1}{A_{PSF}}\sqrt{E_{PSF}}, \tag{5.28}$$

with A_1 being the maximum of the RF signal corresponding to a single point in the reconstruction grid and $A_{PSF} \approx \frac{1}{N}\sum_{j=1}^{N} max(\boldsymbol{A}(:,j))$ being the average amplitude of the RF-PSF.

It follows from our experimental and simulation observations that the numerical minimizer works properly only when the regularization term becomes significant and the ratio between the regularization J_r and fidelity J_f terms reaches a certain value γ. Afterwards, the ratio between the regularization J_r and fidelity J_f terms will decrease with α, as follows from Eq. (5.24) and (5.25). So, a correct reconstruction can be expected when

$$\frac{J_r}{J_f} = \frac{\alpha||T||_1}{||R - \boldsymbol{A}T||_2^2} = -2 + \frac{4ar}{\alpha} \leq \gamma. \tag{5.29}$$

Using Eq. (5.29), one obtains the minimal value α_s that is necessary to retrieve the minimum-L1-norm solution:

$$\alpha_s = \frac{4ar}{2+\gamma} = 4\frac{1}{2+\gamma}\frac{E_{PSF}}{A_{PSF}}A_1 = A_1 F(\gamma). \tag{5.30}$$

For the modelled object, the values of a and r estimated using Eq. (5.27) and (5.28) were $a = 5.2 \times 10^5$, $r = 258$. The normalization factor in Eq. (5.20) and (5.21) was $M\sigma_n^2 = 4.1 \times 10^6$. The parameter $\alpha_e^* = 64$ was computed using Eq. (5.26). The parameter $\alpha_s^* = 2 \times 10^{-3}$ was estimated heuristically.

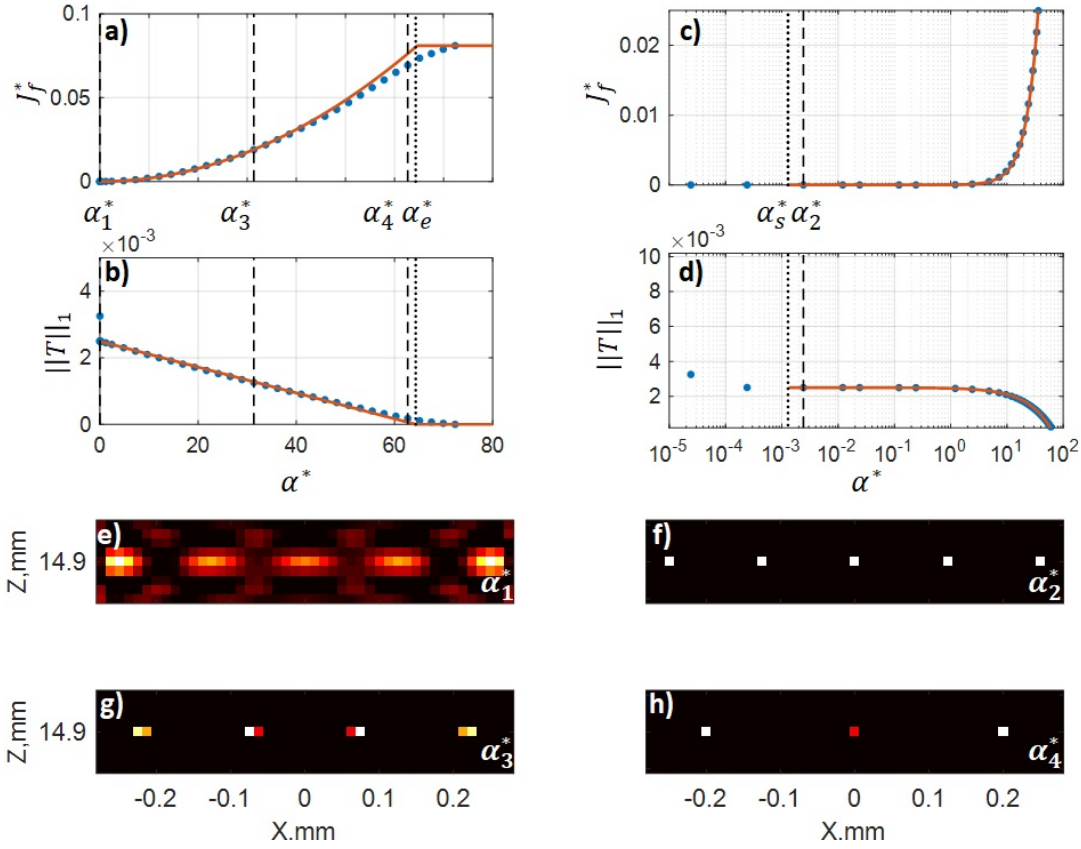

Fig. 5.17 Sparsity-based reconstruction (without the non-negativity constraint) of the modelled object in absence of noise. (a,b) Reconstruction (dotted blue) and theoretical (solid red) curves for the $||T||_1$ norm and the fidelity J_f^* term, overview. Three distinct regions are observed: insufficient regularization ($0 \leq \alpha^* < \alpha_s^*$), regularized solution ($\alpha_s^* \leq \alpha^* < \alpha_e^*$), total object suppression ($\alpha_e^* \leq \alpha^*$). (c,d) Zoom of (a,b) for small α^*. (e-h) Objects reconstructed at different α^*, denoted as $\alpha_1^* = 0$, $\alpha_2^* = 2.4 \times 10^{-3}$, $\alpha_3^* = 31$, and $\alpha_4^* = 64$ in (a-d).

L1 reconstruction results obtained for the modelled object are shown in Fig. 5.17. Three regions with different reconstruction behaviour can be distinguished.

I) $0 \leq \alpha^* < \alpha_s^*$. Condition (5.29) is not satisfied and the L1 reconstruction does not provide the minimum-L1-norm solution. In fact, the reconstruction passes through different solutions (starting from the object shown in Fig. 5.17e) to the underdetermined system $R = \boldsymbol{A}T$. The L1 norm decreases steeply (the vertical part in Fig. 5.17b) until

the minimum-L1-norm solution, which matches the modelled object, is reached (Fig. 5.17f).

II) $\alpha_s^* \leq \alpha^* < \alpha_e^*$. The reconstruction passes from the minimum-L1-norm solution (Fig. 5.17f) to the complete destruction of the object T. In particular, in the reconstruction image the number of sources K decreases while the distances between them shrink (Fig. 5.17f-h).

III) $\alpha_e^* \leq \alpha^*$. All the signal is suppressed and $T(i) = 0, \forall i = \overline{1..N}$. So, the fidelity term attains its maximum whereas the L1 norm reaches zero.

Notably, the theoretical $||T||_1$ and J_f^* curves, obtained using Eq. (5.24) and (5.25), match a large part of the reconstruction curves. The deviation of the $||T||_1$ and J_f^* reconstruction curves from the theoretical behaviour at large α^* is probably due to the strong interference between the sources. As follows from the observed evolution of the reconstructed object, when $\alpha^* >> \alpha_s^*$ the $||T||_1$ and J_f^* curves might still obey Eq. (5.24) and (5.25) with the number of sources K decreasing and the parameter r increasing.

5.6.5.4 Reconstruction of an object under noisy condition

L1 reconstruction results obtained for the modelled object with added noise are shown in Fig. 5.18.

Contrary to reconstruction in absence of noise (Fig. 5.17), when noise is present, reconstruction at $\alpha^* = \alpha_2^* = 2.4 \times 10^{-3}$ (Fig. 5.18f) does no longer provide the correct object. It is only at $\alpha^* = \alpha_4^* = 4.82$ when reconstruction becomes satisfactory (Fig. 5.18h).

The $||T||_1$ and J_f^* curves shown in Fig. 5.18a-d do have two contributions: from the relevant signal (Fig. 5.17a-d) and from the noise (Fig. 5.16). So, at $\alpha^* = \alpha_4^* = 4.82$ most of the noise is suppressed, with the J_f^* noise term reaching one and the L1 noise norm reaching zero. As a result, the object becomes recognizable in the reconstruction image (Fig. 5.18h). For $\alpha_4^* \leq \alpha^*$ reconstruction follows the noiseless case (Fig. 5.17).

5.6.5.5 Choice of the regularization parameter

As follows from object reconstruction in the noiseless case, the reconstruction algorithm provides the best possible solution at $\alpha = \alpha_s$. Below this value, the regularization term is too small and the algorithm does not provide the minimum-L1-norm solution. Above this value, the reconstruction image undergoes undesirable transformations.

The value of α_s^* could be found by fitting theoretical J_f^* and $||T||_1$ curves to the reconstruction ones. However, to build the theoretical model, one must know the object sparsity K and the maximum A_1 of the RF signal corresponding to a single point on the reconstruction grid. These values are not usually available in practice. In addition,

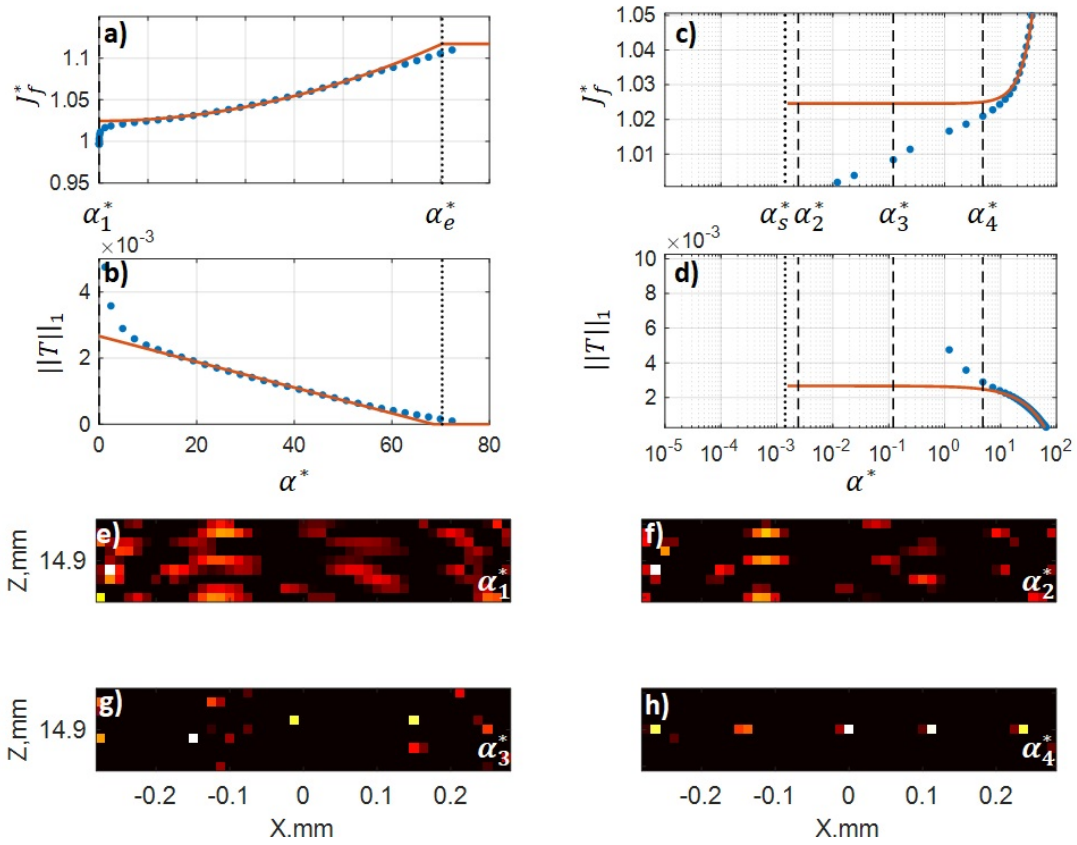

Fig. 5.18 Sparsity-based reconstruction (without the non-negativity constraint) of the modelled object in presence of noise. (a,b) Reconstruction (dotted blue) and theoretical (solid red) curves for the $||T||_1$ norm and the J_f^* term, overview. (c,d) Zoom of (a,b) for small α^*. (e-h) Objects reconstructed at different α^*, denoted as $\alpha_1^* = 0$, $\alpha_2^* = 2.4 \times 10^{-3}$, $\alpha_3^* = 0.12$, and $\alpha_4^* = 4.82$ in (a-d). The object appear unrecognizable(e-g) until most of the noise is suppressed (h).

the presence of noise can make fitting more challenging as noise perturbs the initial part of the J_f^* and $||T||_1$ curves (Fig. 5.18). Moreover, when too much noise is added, the imaged object is not recognizable at $\alpha = \alpha_s$. In this case, the imaged object may appear at higher α^* when most of the noise is suppressed, but the reconstruction fidelity can not be assured.

In summary, the right value of the regularisation parameter can hardly be estimated without exploiting additional (not following from sparsity-based reconstruction) information about the object.

5.6.6 Influence of the non-negativity constraint

5.6.6.1 Noise-free situation

Several reconstruction images obtained in sparsity-based regularization with the non-negativity constraint are shown in Fig. 5.19. On comparing Fig. 5.17e and 5.19a, one

remarks that the non-negativity constraint is enough to provide the right solution when $\alpha^* = 0$ (the L1 regularization term does not intervene at all). Starting from $\alpha^* = \alpha_s^*$, condition (5.29) is fulfilled. As a result, it is the L1 regularization term that contributes the most to the reconstruction and the reconstruction results shown in Fig. 5.17f-h and 5.19b-d appear identical.

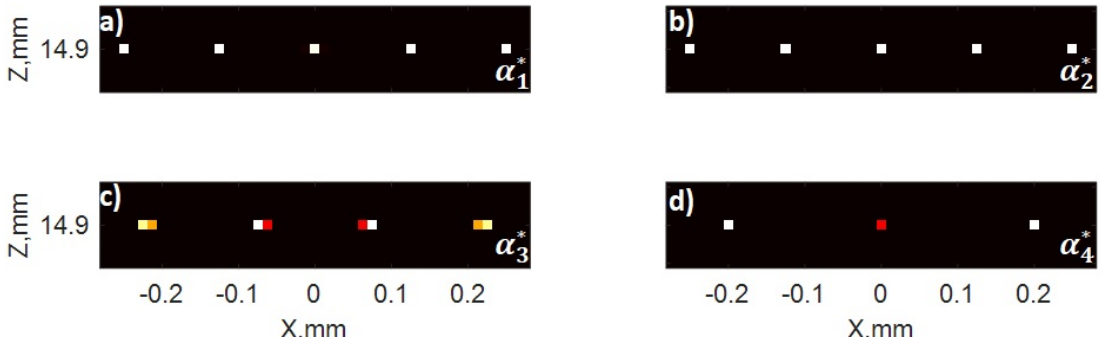

Fig. 5.19 Sparsity-based reconstruction (with the non-negativity constraint) of the modelled object in absence of noise, the reconstruction images corresponding to different values of the regularization parameter: $\alpha_1^* = 0$ (a), $\alpha_2^* = 2.4 \times 10^{-3}$ (b), $\alpha_3^* = 31$ (c), and $\alpha_4^* = 64$ (d). The non-negativity constraint leads to the right solution (a) even when $\alpha^* = 0$ and the L1 regularization term is not present at all.

5.6.6.2 Noisy situation

Reconstruction results obtained with added noise are shown in Fig. 5.20. As in the noiseless case (Fig. 5.19), the object can be already recognized at $\alpha_1^* = 0$. At higher α^* L1 regularization suppresses the noise further.

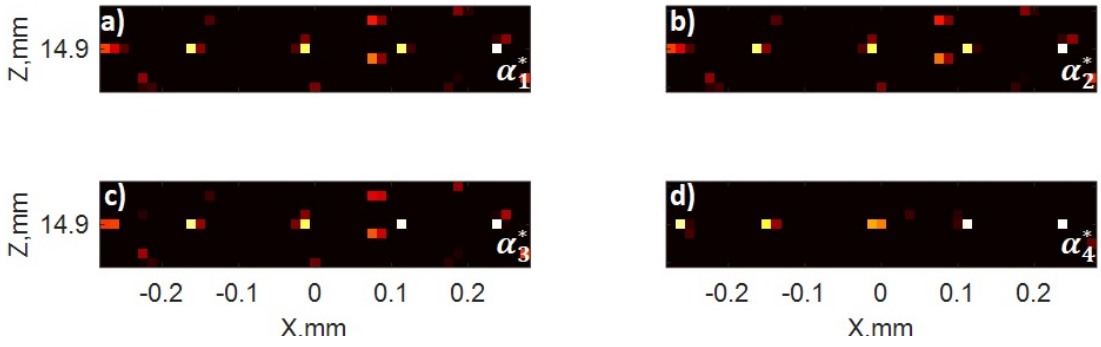

Fig. 5.20 Sparsity-based reconstruction (with the non-negativity constraint) of the modelled object in presence of noise, the reconstruction images corresponding to different values of the regularization parameter: $\alpha_1^* = 0$ (a), $\alpha_2^* = 2.4 \times 10^{-3}$ (b), $\alpha_3^* = 0.12$ (c), and $\alpha_4^* = 4.82$ (d). The object is already quite well reconstructed at $\alpha_1^* = 0$. Then, at higher α^* L1 regularization suppresses the noise further.

5.6.7 Reliability

Fig. 5.21 shows several modelled objects and images reconstructed using the sparsity-based approach. Although two sources separated by $\Delta X = 25\ \mu m$ are correctly reconstructed (Fig. 5.21a,d), the object consisting of three sources separated by the same distance is not reconstructed properly (Fig. 5.21b,e). In particular, the central source is not visible in the reconstruction image. A possible reason is that the signal from the central source is masked by signals from the two other sources due to interference effects. It is only when the source separation reaches $\Delta X = 50\ \mu m$ that interference effects become weak enough and all the three sources are reconstructed (Fig. 5.21c,f).

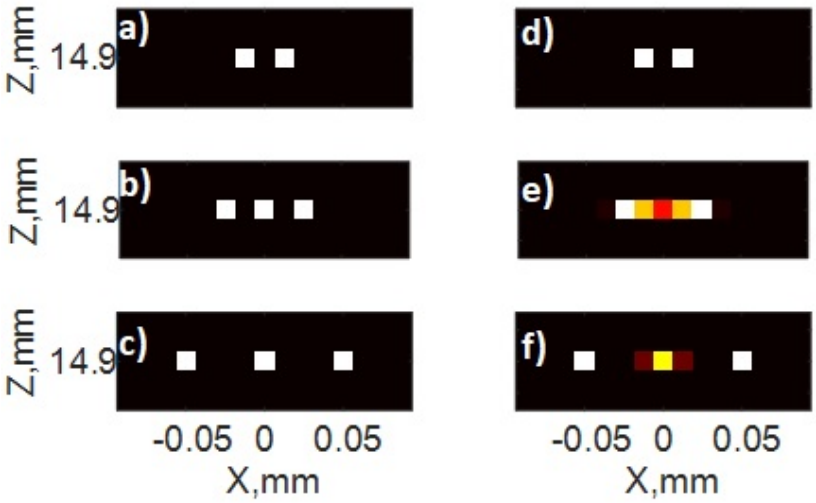

Fig. 5.21 Modelled objects (a-c) and corresponding reconstruction images (d-f) obtained in sparsity-based reconstruction. (a) 2 points separated by $\Delta X = 25\ \mu m$. (b) 3 points separated by $\Delta X = 25\ \mu m$. (c) 3 points separated by $\Delta X = 50\ \mu m$.

This simple example shows that the reliability of sparsity-based reconstruction depends in a complex manner on the imaged object. Being able to distinguish two sources separated by a certain distance ΔX does not mean that any object with the minimal feature separation equal to ΔX will be correctly reconstructed.

5.6.8 Positivity-based reconstruction

In this section we will determine whether the non-negativity constraint can be enough to reconstruct the object without using the regularization term. To be able to compare the positivity-based resolution with the resolution provided by sparsity-based regularization, we apply positivity-based reconstruction to the noise-free simulated data for the two channel experiment that we used in section 5.5.3.3.

5.6.8.1 Resolution limit

The positivity-based reconstruction results obtained for the simulated two channel experiment are shown in Fig. 5.22. It can be noticed that these results are similar to the L1 reconstruction images obtained without the non-negativity constraint (Fig. 5.22). However, the resolution limit in positivity-based reconstruction is higher: $\Delta X = 44\ \mu m$ beside $\Delta X = 24\ \mu m$ in sparsity-based reconstruction (the PSF lateral FWHM being $\Delta X = 398\ \mu m$).

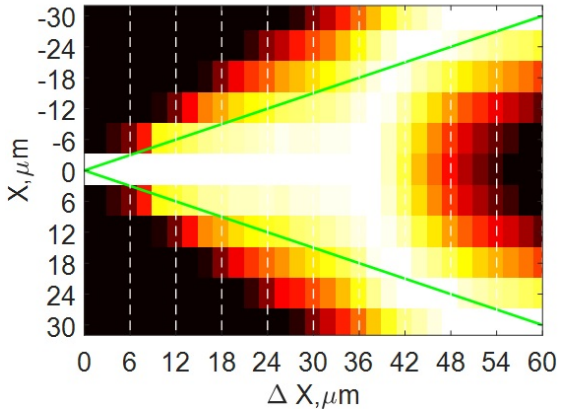

Fig. 5.22 Positivity-based reconstruction for two approaching channels (simulations, BF-based, without noise): projections of normalized XZ reconstruction images (reconstruction grid step $dx = 6\ \mu m$) onto the X axis, obtained for different distances ΔX between the channels. The green lines designate theoretical separation. (a) Reconstruction applied to the mean image. (b) Reconstruction applied to the variance image.

5.6.8.2 Reliability

Fig. 5.23 illustrates several modelled objects and images obtained in positivity-based reconstruction. These results are similar to those shown for sparsity-based reconstruction in Fig. 5.21. In particular, for the same minimal distance between object features, one object can be reconstructed well (Fig. 5.23a,d), while another one is not reconstructed (Fig. 5.23b,e). Similarly to sparsity-based reconstruction, reliability of positivity-based reconstruction depends in a complex manner on the imaged object.

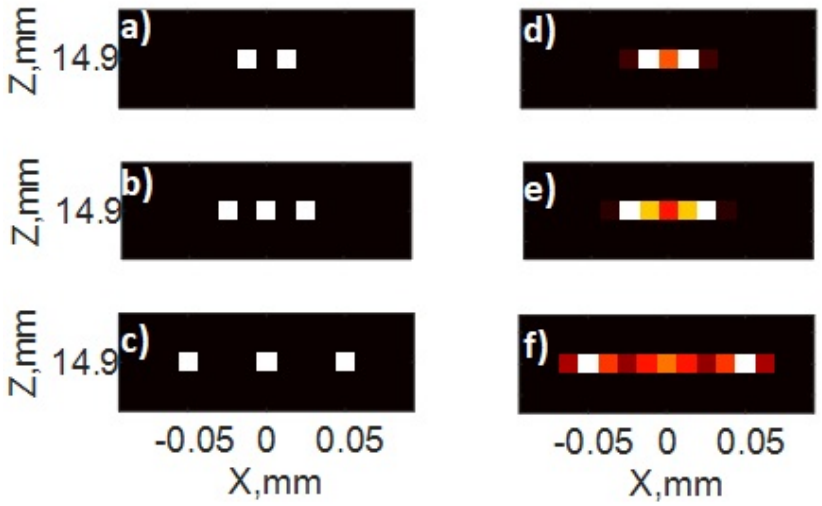

Fig. 5.23 Modelled objects (a-c) and corresponding reconstruction images (d-f) obtained in positivity-based reconstruction. (a) 2 points separated by $\Delta X = 25\ \mu m$. (b) 3 points separated by $\Delta X = 25\ \mu m$. (c) 3 points separated by $\Delta X = 50\ \mu m$.

5.7 Conclusion

In this Chapter, super-resolution in cross-sectional PA imaging was obtained by exploiting a model-based reconstruction approach. In particular, it was shown that in a real imaging environment where some noise is present, L1 (sparsity-based) reconstruction can lead to sub-diffractional resolution while other model-based techniques (Moore-Penrose pseudoinverse, Tikhonov regularization, positivity-based reconstruction) may result in the imaged object appearing unrecognizable in the reconstruction image. In our study, five regularly distributed targets of equal strength separated by $L_{cc} = 125\ \mu m$ were resolved in the L1 reconstruction image, the classical resolution limit being around $154\ \mu m$. In the same proof-of-principle experiment we also showed that model-based reconstruction provides equivalent results whether it is applied to RF or BF data.

In another experiment, we demonstrated that two point targets can be resolved at least down to 80 μm in L1 reconstruction. Shorter distances were explored in computer simulations, where we demonstrated that two point targets can be resolved down to 24 μm (classical resolution limit being about 398 μm). This limit is probably related to the maximal numerical precision and for the same acoustic signals will vary slightly for different acquisition equipment and signal processing pipeline. We also demonstrated that when the variance image is used for reconstruction instead of the single-shot (mean) image the resolution can be about $\sqrt{2}$ times better. This resolution improvement corresponds to the resolution gain provided by 2nd order statistical analysis [Chaigne et al., 2016].

To understand better the mechanism of sparsity-based reconstruction, especially the role of the regularization parameter (which the reconstruction result depends on) and the non-negativity constraint, we carried out a theoretical analysis. We proposed a model that describes the evolution of the fidelity term and the L1 norm of the reconstructed object as a function of the regularization parameter and verified this model in simulations. We showed that the regularization parameter in L1-based reconstruction can hardly be predicted without using additional (not related to regularization) information about the object. By testing different objects we also demonstrated that it is hard to predict whether L1 reconstruction will provide the right object at any value of the regularization parameter.

Additional studies were carried out to determine whether the positivity-based reconstruction (model-based reconstruction with the non-negativity constraint without the regularization term) can in principle (at infinite SNR) provide super-resolution. In computer simulations it was shown that two targets can be resolved down to 44 μm which is a bit higher than for sparsity-based reconstruction. However, similarly to sparsity-based reconstruction, the possibility to reconstruct a given object using the non-negativity constraint can not be certain.

To sum up, sparsity-based reconstruction can lead to super-resolution but additional knowledge about the object is necessary to assess the reconstruction result and to predict the optimal value of the regularization parameter. In this regard, additional information can be provided by other imaging techniques. One other approach would be to use the deep learning framework trained with pairs consisting of input RF/BF data and corresponding regularization parameters. Some combinations of the deep learning and sparsity-based techniques have already been proposed [van Sloun et al., 2018].

It should also be noted that in this chapter we demonstrated that under some conditions sparsity-based reconstruction can successfully resolve point targets separated by a sub-diffractional distance. This can be applied in super-localization imaging, where the concentration of contrast agents at any time moment is currently limited by classical resolution (see Chapter 1). If sparsity-based reconstruction could be employed to resolve densely packed contrast agents, this could drastically improve the temporal resolution of super-localization. In US super-localization, it has already been proposed to use L1-based reconstruction [Shu et al., 2018] to detect microbubbles on each diffraction-limited image. From the results reported in [Shu et al., 2018] and those of the present chapter one can expect that sparsity-based reconstruction will permit a significant increase in the concentration of contrast agents in PA as well as in US super-localization.

CHAPTER 6

Photoacoustic and ultrasound imaging with a sparse array

6.1 Introduction

6.1.1 2D imaging vs 3D imaging

Detection arrays consisting of a number of identical elements are often used for acquiring acoustic signals in ultrasound (US) as well as in photoacoustic (PA) imaging. Developed for cross-sectional 2D imaging, linear transducer arrays usually have N_{el} = 128 or N_{el} = 256 elements arranged in a single row, the element spacing being about $\lambda_{ac}/2$ [Cheston and Frank, 1990] ($\lambda_{ac} = v_s/f_c$ being the acoustic wavelength at the central frequency f_c of the transducer). Such arrays permit imaging an object in the XZ plane in a single scan (see section 1.3.4). As stated in Chapter 1, at a distance R from the transducer aperture, the classical lateral resolution of a linear array is given by

$$\Delta X \sim \lambda_{ac}\frac{R}{D}, \tag{6.1}$$

where D is the length of the transducer aperture.

If one wants to retrieve a volumetric distribution of the probed quantity in a single scan, detection arrays with a 2D or 3D aperture, such as matrices of elements or ring arrays, are to be used. To provide classical resolution given by Eq. (6.1) in the lateral directions X and Y, the aperture size in the plane XY should be $D \times D$. In addition, to avoid grating lobes appearing due to spatial undersampling, the element spacing should be at most $\lambda_{ac}/2$. Thus, detection arrays for 3D imaging should have at least N_{el}^2 elements. For example, if a linear array has 128 elements, the corresponding array for 3D imaging should have $N_{el}^2 = 16384$ elements. However, such a great number of elements are hard to connect and are hard to control [Fenster et al., 2001]. So, it is important to propose methods that would provide the same quality of reconstruction images with fewer transducer elements.

6.1.2 State-of-the-art

One of the earliest schemes for reducing the number of elements is to use a sparse array. Sparse arrays were first proposed in 3D US imaging [Turnbull and Foster, 1991; Smith et al., 1991]. The corresponding reduction scheme suggests using a selection of elements of a periodic dense array without changing the total transducer aperture. Such a selection can either be a random subset of elements [Turnbull and Foster, 1991] or a defined pattern [Smith et al., 1991]. The advantage of random sparse arrays is that in these arrays grating lobes are avoided by eliminating the uniform, periodic arrangement of elements [Turnbull and Foster, 1991]. Experimental investigations of imaging performance of sparse arrays confirmed [Roux et al., 2017b,a; Cohen and Eldar, 2018] that such arrays can provide a diffraction-limited resolution similar to that of all-element arrays.

Sparse arrays have also been used for 3D photoacoustic tomography (PAT) [Ephrat et al., 2008; Roumeliotis et al., 2011, 2012; Han et al., 2017; Dean-Ben et al., 2012; Wang et al., 2012]. In PA sparse-array imaging, transducer elements are usually regularly distributed. To compensate for artifacts arising from spatial undersampling, reconstruction via the model-based approach is usually employed. For additional details on model-based reconstruction in PA imaging the reader is referred to Chapter 5.

All the studies on sparse arrays cited above considered only diffraction-limited resolution. It has been only recently that super-resolution was demonstrated in sparse-array imaging. In particular, a super-resolved image of two touching subwavelength-diameter tubes was obtained in sparse-array 3D US imaging [Harput et al., 2019]. However, the demonstrated resolution improvement was achieved by super-localization which requires contrast agents and has a poor temporal resolution (see Chapter 3).

6.1.3 Objectives of this chapter

In this chapter, we propose to apply model-based reconstruction, in particular L1 (sparsity-based) regularization, to achieve super-resolution in sparse-array imaging. Model-based reconstruction is chosen as, in opposite to other super-resolution techniques, including super-localization, it can provide super-resolution in single-shot imaging and it does not require any contrast agents (see Chapter 5). We restrict out demonstration to 2D imaging although the same principles could be used in 3D imaging. Our study is based on two proof-of-concept experiments, the first experiment demonstrating super-resolution in sparse-array PA imaging, the second one demonstrating super-resolution in sparse-array US imaging. In these experiments, we obtain a cross-sectional image of five parallel microfluidic channels separated by a sub-diffractional distance. In addition, we conduct computer simulations to determine how the L1 reconstruction quality is related to the number of transducer elements and the signal-to-noise ratio (SNR).

6.2 Experimental demonstration

6.2.1 Materials and methods

6.2.1.1 Samples

In both PA and US experiments we use identical samples, each consisting of five parallel microfluidic channels with a rectangular cross-section (Fig. 6.1). To perform cross-sectional imaging, the microchannels are placed perpendicularly to the imaging plane XZ of a linear transducer array (type L22-8) at the US probe elevational focus distance z_f = 15 mm. In this plane, each channel is h_{ch} = 50 μm high and w_{ch} = 40 μm wide, the center-to-center distance between neighbouring channels being L_{cc} = 125 μm. To provide a good contrast, the sample is filled with absorbing liquid (Patent Blue V) in the PA experiment and left empty in the US experiment. For more details on fabrication of the microfluidic samples the reader is referred to Chapter 2.

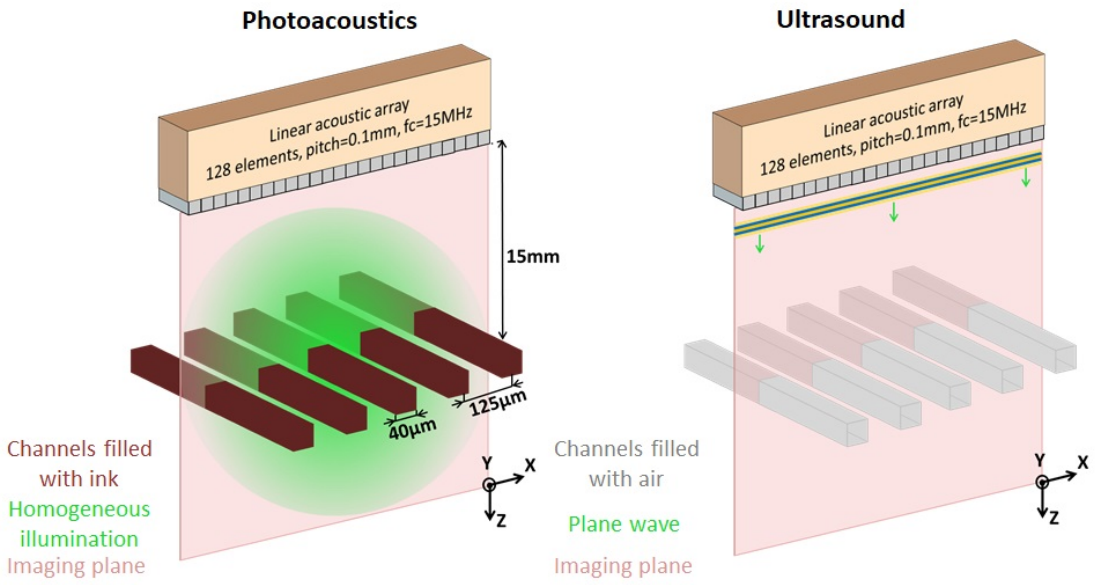

Fig. 6.1 Samples carrying five parallel microchannels are placed perpendicularly to the imaging plane. Each channel h_{ch} = 50 μm high and w_{ch} = 40 μm wide, the center-to-center distance is L_{cc} = 125 μm. In the PA experiment, the sample is illuminated by a laser pulse and the resulting PA signals are received by a linear US probe. In the US experiment, a plane wave is emitted in the sample's direction and the backscattered signals are registered.

6.2.1.2 Experimental protocols

A schematic of the experimental setup is shown in Fig. 2.1. In our experiments, transmission and reception of acoustic waves were assured by 128 elements of a linear transducer array (type L22-8).

In the PA experiment, PA signals were acquired on illuminating the sample with a single laser pulse ($\lambda_{laser} = 532\ nm$, fluence= 3 mJ/cm^2).

In the plane wave US experiment, US backscattered signals were registered after a short US pulse was sent perpendicularly to the sample. This pulse was simultaneously emitted by all the 128 available elements of the linear transducer array (emission amplitude 35 V).

For additional information on the experimental equipment the reader is referred to Chapter 2.

To apply model-based reconstruction, we also acquired the PSF of the imaging system in both PA and US regimes. The PSF full width at half maximum (FWHM) was $\Delta X = 154\ \mu m$, $\Delta Z = 139\ \mu m$ in PA imaging and $\Delta X = 154\ \mu m$, $\Delta Z = 80\ \mu m$ in US imaging (see section 2.5).

The experimental SNR was computed as the ratio between the maximum of the acquired radio frequency (RF) signal and the standard deviation of electronic noise calculated over a signal-free region of the RF data. In the PA experiment, the estimated SNR was $\text{SNR}_{PA} \approx 4500/30 = 150$. In the US experiment, the estimated SNR was $\text{SNR}_{US} \approx 2500/30 = 83$.

6.2.1.3 Image reconstruction

Image reconstruction was performed via L1 regularization that was considered in detail in Chapter 5. The L1 reconstruction was based on the following minimization:

$$\hat{T}_0 = \underset{T}{\text{argmin}}\{||R - \boldsymbol{A}T||_2^2 + \alpha||T||_1\}, \tag{6.2}$$

where $R^{M\times 1}$ represents the received radio frequency (RF) PA or RF US data, $\hat{T}_0^{N\times 1}$ is an estimate of the imaged object discretized on the reconstruction grid, $\boldsymbol{A}^{M\times N}$ is the propagation matrix containing the PSF for each point of the reconstruction grid, α is the regularization parameter. The matrix $\boldsymbol{A}$ was constructed using the single PSF acquired in the imaging zone (see section 5.2.3 for construction of the matrix $\boldsymbol{A}$).

As follows from section 5.6.5.1 the fidelity term $J_f = ||R - \boldsymbol{A}T||_2^2$ in Eq. (6.2) is proportional to the number of transducer elements when the choice of α provides the right object. So, if the regularization parameter $\alpha = \alpha(N_1)$ is somehow obtained for N_1 elements, the same ratio between the fidelity J_f and the regularization $J_r = \alpha||T||_1$ terms for N_2 elements will be at $\alpha(N_2) = N_2/N_1\alpha(N_1)$. This choice would provide an efficient noise suppression at $N_{el} = N_2$. On the other hand, the regularization term should be large enough to reconstruct the right object. In this regard, α should first be estimated for the smallest number of elements at which reconstruction is acceptable. So, in our experiments we first determined $\alpha = \alpha(N_{el} = 8)$ by comparing visually

the reconstructed object with the real sample. Based on $\alpha(N_{el} = 8)$ the regularization parameter for other values of N_{el} was obtained.

Reconstruction (6.2) was performed with a fast iterative shrinkage-thresholding algorithm (FISTA) [Beck and Teboulle, 2009; Vu, 2016]. Details on the realization of the reconstruction algorithm can be found in Appendix B. The object to image was discretized over a cartesian grid with a L_{cc}/10 = 12.5 μm step, resulting in $N_x = 61$ points in the X direction and $N_z = 13$ points in the Z direction. In the PA experiment, the length of the vector $T^{N\times1}$ was N = $N_x \times N_z = 793$, the length of the vector $R^{M\times1}$ was M = 4636, the rank of propagation matrix $\boldsymbol{A}^{M\times N}$ was $rank(\boldsymbol{A}) = 346 < N$. In the US experiment, the length of the vector $T^{N\times1}$ was N = $N_x \times N_z = 793$, the length of the vector $R^{M\times1}$ was M = 5632, the rank of propagation matrix $\boldsymbol{A}^{M\times N}$ was $rank(\boldsymbol{A}) = 368 < N$.

A 2D Gaussian filter with σ_g = L_{cc}/10 = 12.5 μm was applied after reconstruction to smooth the pointy images. Bicubic interpolation was used afterwards to improve image visualization. The interpolated values were placed on a spacial grid with a $L_{cc}/40 \approx 3$ μm step.

6.2.2 Results

6.2.2.1 Photoacoustic and ultrasound super-resolution with the full array

First, we tested whether a super-resolved image of the object can be obtained in PA and US regimes with all 128 available transducer elements. Standard delay-and-sum beamforming and L1 reconstruction results obtained in all-element imaging are compared in Fig. 6.2.

As shown in Fig. 6.2a,e, after standard reconstruction the five imaged cross-sections appear indistinguishable. This complies with the diffraction theory as, by construction, the center-to-center distance between neighbouring channels (L_{cc} = 125 μm) is below the resolution limit defined by the lateral FWHM of the PSF (ΔX = 154 μm in PA and US imaging). As expected from the results of Chapter 5, the L1 approach provides a super-resolved image with five well separated regions in both PA and US experiments. Importantly, here we extend the results of Chapter 5 to single-shot plane wave US imaging, illustrating the generality of the proposed reconstruction approach.

Although the PA and US reconstruction images in Fig. 6.2 look similar, some artifacts are present in the US images. Furthermore, the average interchannel distance in the US images (112 μm) also deviates from the true value ($L_{cc} = 125$ μm), whereas in the PA images the interchannel distance is restored correctly. There are several constraints that may lead to the observed differences in PA and US reconstruction. For example, since in the US experiment the acoustic wave crosses the upper PDMS layer two times whereas there is only one passage in the PA experiment, one can expect the US data re-

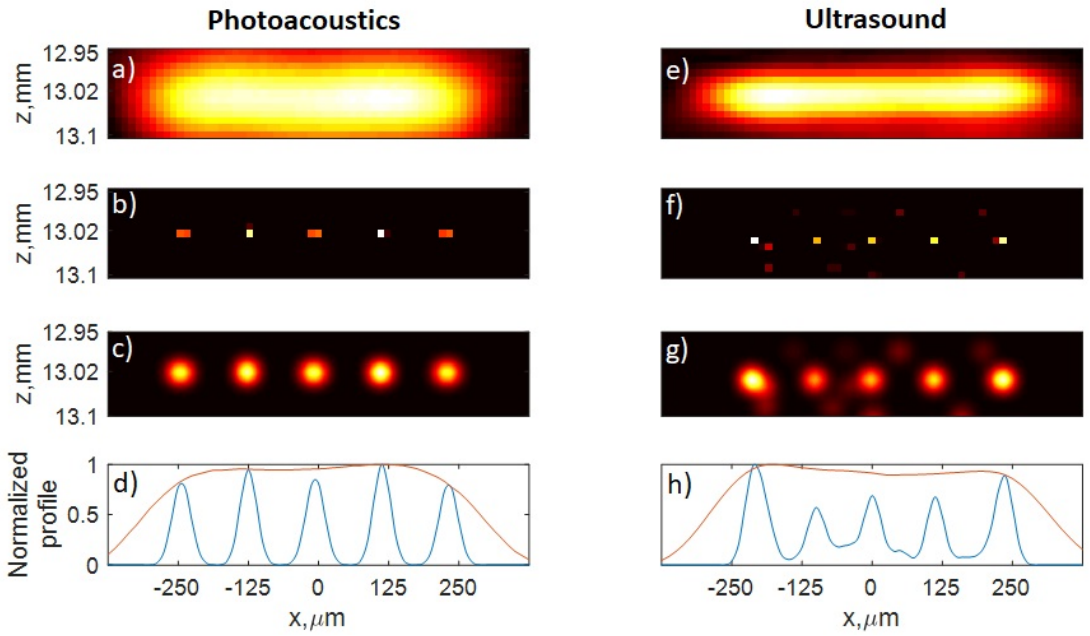

Fig. 6.2 Images reconstructed in the PA (a-d) and US (e-h) experiments using 128 elements of the probe. (a,e) Conventional beamformforming cross-sectional images of the sample. The microchannels are indistinguishable as the center-to-center distance L_{cc} = 125 μm is smaller than the lateral FWHM of the PSF (154 μm). (b,f) Images obtained with L1 - reconstruction. The reconstruction recovers five distinct regions corresponding to the microfluidic channels. (c,g) Reconstruction images (b) and (f) after smoothing out by a 2D spatial Gaussian filter (σ_g = 12.5 μm) and interpolating on a 3 μm grid. (d,h) Red: normalized amplitude profile on the envelope images (a) and (b); blue: normalized amplitude profile on the filtered reconstruction images (c) and (g).

construction to be more erroneous as we neglect the deviation of the speed of sound in PDMS from the speed of sound in water. In addition, reverberations between the PDMS surface and the PDMS-channel interface interfere significantly with the useful signal in US imaging. Given the actually rather strong assumption that consists in neglecting the presence of PDMS (especially in US imaging), the proposed super-resolution reconstruction scheme can be considered relatively robust in spite of the sample geometry being simple.

6.2.2.2 Photoacoustic and ultrasound super-resolution with a sparse array

To investigate whether L1 reconstruction can lead to super-resolution in sparse-array imaging we applied L1 reconstruction to data acquired by only a fraction of the probe elements. To this end, we removed the elements of the vector R and the rows of the matrix $\boldsymbol{A}$ corresponding to the transducer elements taken out from consideration. To preserve the classical resolution limit, the resulting probe aperture was kept constant by including the first and the last elements of the transducer array. The other elements were regularly distributed along the probe. The objects reconstructed with 4, 8 and 16

elements are compared to the full-array reconstruction in Fig. 6.3.

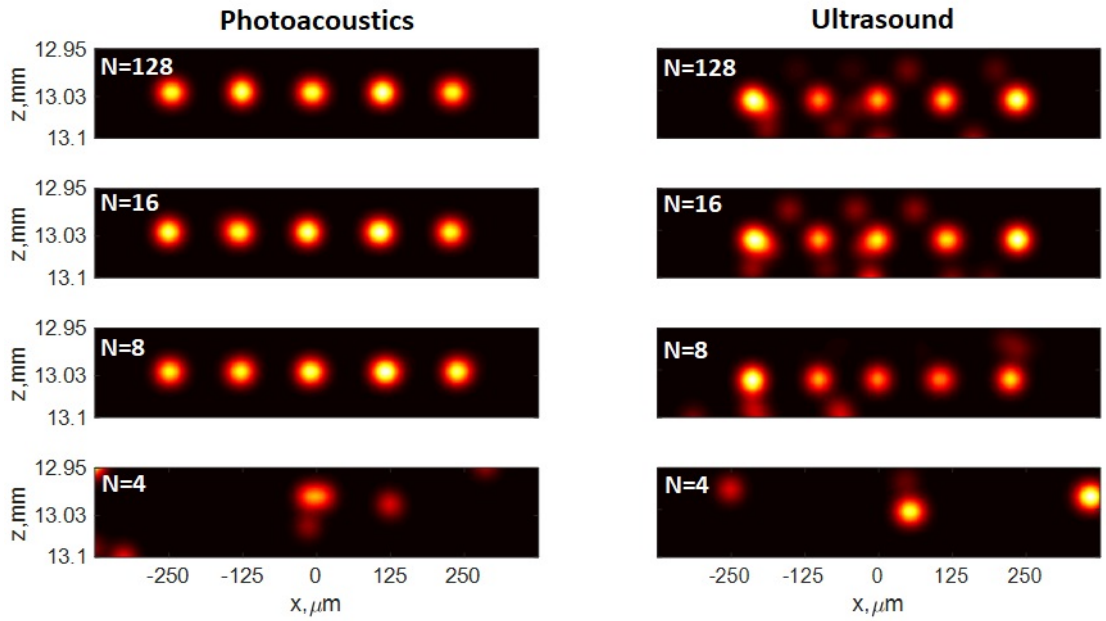

Fig. 6.3 Images obtained with L1 reconstruction in PA and US experiments using N_{el} = 4, 8, 16 and 128 transducer elements regularly distributed along the probe aperture. A 2D spatial Gaussian filter (σ_g = 12.5 μm) interpolation on a 3 μm grid were applied after the reconstruction.

It turns out that in both PA and US experiments super-resolved images of the microchannels can be obtained by using down to 8 elements of the probe. Interestingly, the drastic reduction in the number of probe elements (8 against 128) did not affect the apparent image quality. However, with less than 8 elements used for the reconstruction, the resulting object is unrecognizable in the reconstruction image.

The fact that L1 reconstruction fails to recover the object with less than 8 transducer elements could be explained by lack of information about the object. Indeed, the quantity of the useful signal decreases when the number of elements is reduced whereas the noise level remains the same. So, it can be supposed that for a given SNR there is the minimal number of elements $N_{el\,min}$ that provides the required quality of reconstruction.

6.3 Theoretical investigation

To investigate how $N_{el\,min}$ depends on the SNR, we carried out a series of numerical simulations mimicking our PA experiment (but also representative for the US experiment). The five imaged cross sections were modelled as five point sources separated by $L_{cc} = 125\ \mu m$. In the simulations, we performed model-based reconstruction of this modelled object using a perfectly known propagation matrix $\boldsymbol{A}$ for several levels of the SNR.

6.3.1 Simulation methods

The simulation data was generated on the following grounds:

- All the transducer elements are point sources;
- The emitted PA wave is the same for all imaged point sources, the detected signals are identical in amplitude and spectrum, but they are shifted in time according to the distance between each imaged source and each transducer element;
- The detected signals have a central frequency and bandwidth corresponding to those used in experiments, with the same sampling frequency as in experiments;
- Different levels of SNR are chosen by changing the amplitude of the modelled PA signals. In all simulations, Gaussian noise with a zero mean and the rms of $\sigma_n = 30$ is added to the detected signals. Such noise resembles the noise produced by the acquisition electronics in our experiments (see section 2.3).

As a metrics of the reconstruction quality, we computed the correlation between each reconstructed object $\hat{T}_0$ and the true modeled object T_{ref}:

$$C = \frac{\sum_{i=1}^{n} \hat{T}_0(i) \cdot T_{ref}(i)}{\sqrt{\sum_{i=1}^{n} \hat{T}_0^2(i) \cdot \sum_{i=1}^{n} T_{ref}^2(i)}}. \tag{6.3}$$

Before computing correlation (6.3), the filtering and interpolation used for the reconstruction images (see section 6.2.1.3) were also applied to T_{ref}. For each SNR level, correlation (6.3) was calculated for 100 noise realizations, Fig. 6.4 represents the average correlation value.

6.3.2 Results

Fig. 6.4 illustrates how the average correlation between the reconstruction image and the modeled object depends on the number of transducer elements and the SNR.

First, it can be clearly seen from Fig. 6.4 that for any number of elements the correlation increases with the SNR. Then, for small number of transducer elements, the SNR required for a given correlation goes down steeply while the number of elements increases. When more than 8 elements are taken, the SNR required for a given correlation decreases very gradually with the increase of the number of elements.

The observed behaviour can be partially explained using the rank of the propagation matrix $\boldsymbol{A}$. Regularization-based reconstruction has two tasks: to provide the right object out of many possible objects corresponding to the input data and to suppress noise. The number of possible objects depends on the rank of the propagation matrix $\boldsymbol{A}$. The higher the rank, the fewer objects match the input data. Fig. 6.5 shows how the

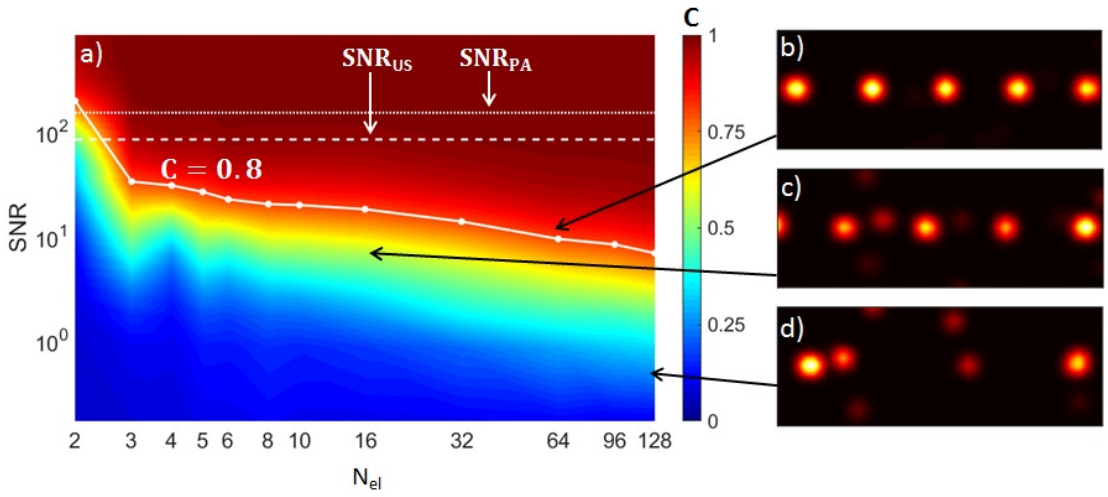

Fig. 6.4 Simulation results. (a) - correlation C as a function of the single-element signal-to-noise ratio (SNR) and the number of transducer elements N_{el}, dotted line: SNR_{PA} = 150 in the PA experiment, dashed line: SNR_{US} = 83 in the US experiment. (b-d) - typical simulation images: (b) - N_{el} = 64, SNR = 16, C = 0.85, (c) - N_{el} = 16, SNR = 10, C = 0.57, (d) - N_{el} = 128, SNR = 0.8, C = 0.23.

rank of the propagation matrix depends on the number of transducer elements N_{el}. For small number of elements, $rank(\boldsymbol{A})$ increases rapidly, then it levels off at $N_{el} = 32$. This means that for $N_{el} > 32$ adding more transducer elements does not bring new information about the object. A possible reason is that signals from neighbouring elements become highly correlated. However, adding new transducer elements improves the SNR. This correlates with the observed behaviour of the C = 0.8 curve plotted in Fig. 6.4: for $N_{el} > 32$ this curve fits $A/\sqrt{N_{el}}$, $A = const$.

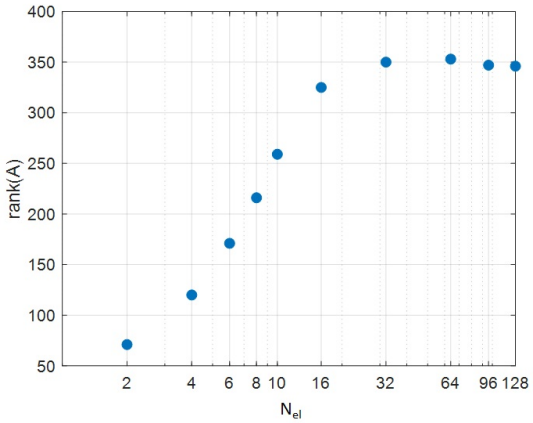

Fig. 6.5 Rank of the propagation matrix $\boldsymbol{A}$ as a function of the number of transducer elements (simulations). For small number of elements N_{el} , $rank(\boldsymbol{A})$ increases rapidly, then it levels off at $N_{el} = 32$. This means that for $N_{el} > 32$ adding more transducer elements does not bring new information about the object.

It can also be observed that when central elements of the probe make up a large

proportion of the elements taken (for example, in imaging with 3 or 5 transducer elements), the observed correlation experiences a noticeable drop. This may arise from the fact that signals coming from different microchannels are the least distinguishable on the central part of the probe aperture.

Finally, our simulations show than if the SNR is very high, only two transducer elements could be enough for an acceptable reconstruction. This result stands in agreement with the triangulation principle stating that only two antennas are needed to localize a point source lying on a plane. Then, the ability to distinguish different sources is limited by the SNR.

Although our simulations provide a good qualitative explanation of the experimental results, they predict a high correlation coefficient for $N_{el} > 2$ transducer elements and the experimental SNR (SNR_{PA} = 150, SNR_{US} = 83) whereas the experimental reconstruction does not provide the correct object with less than 8 elements. This quantitative discrepancy is due to the reconstruction of the simulated data being based on a perfectly known forward model while the experimental reconstruction involves several assumptions and approximations. For example, in experiments the PSF is not perfectly known as it may vary from one experiment to another due to a small difference between the samples and some alignment uncertainties. In addition, in simulations the signal amplitude is the same on all transducer elements while for a real transducer the signal amplitude decreases towards the boundary elements.

6.4 Conclusion

We demonstrated experimentally that L1 reconstruction can provide super-resolution in single-shot sparse-array PA and US imaging. In particular, super-resolved images obtained using only 8 transducer elements were close to those reconstructed with 128 transducer elements. By use of computer simulations, we showed that for each SNR there exists a minimal number of array elements required for a given quality of reconstruction. This minimal number decreases when the SNR goes up.

One of the major advantages of L1 reconstruction is that this approach can in principle be applied to any spatial distribution of the transducer elements as the imaging geometry is automatically taken into account by the propagation matrix. So, one could expect that results similar to those reported here would have been obtained even if the transducer elements were not distributed regularly on the probe aperture. For the same reason, L1 reconstruction could provide super-resolution in 3D imaging. In this case, the additional coordinate(s) of the transducer elements would also be taken into account by the propagation matrix.

Following these promising preliminary results, more theoretical simulations and experiments should be conducted to further investigate L1 reconstruction in super-

resolution sparse-array imaging. Certainly, additional experiments are needed to test the proposed approach with more sophisticated samples and in the case of 3D imaging. In addition, it would be interesting to study how the resolution limit of l_1 - based reconstruction depends on the probe aperture.

CHAPTER 7

Flow-based visibility enhancement in photoacoustic imaging

7.1 Introduction

7.1.1 Origin of visibility problems in photoacoustic imaging

In ultrasound (US) imaging, spatial heterogeneities of acoustic properties of the imaged medium lead to formation of speckles that enable visualization of large or complex-shaped structures [Wagner, 1983]. In contrast, photoacoustic (PA) imaging is generally considered to be speckle-free. The reason [Guo et al., 2009] is that in PA imaging under instantaneous and homogeneous illumination, all points of the imaged object experience a simultaneous pressure rise which results in emission of strongly coherent acoustic waves interfering constructively in some directions and destructively in others. While the absence of speckles in PA imaging is often presented as an advantage of the technique, it may also lead to some reconstruction artifacts. Fig. 7.1 illustrate two common visibility artifacts in PA imaging with images obtained with the commercial system AcousticX (https://www.cyberdyne.jp).

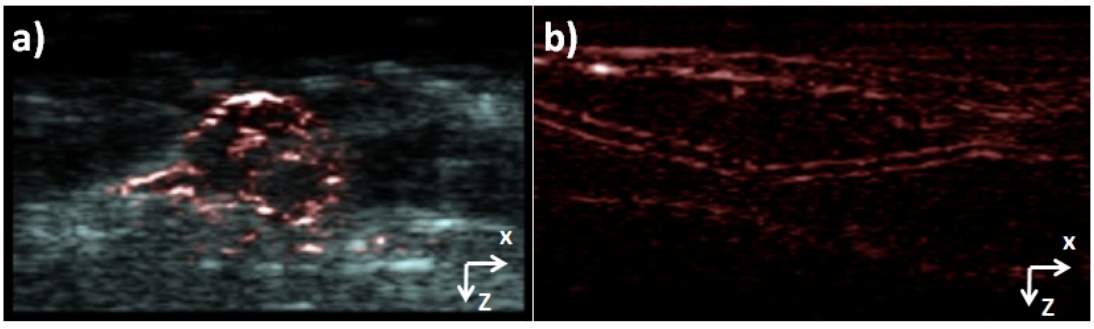

Fig. 7.1 Visibility artifacts are present in PA images: the central part of large objects is not reconstructed, blood vessels along the Z axis are not visible. (a) Tumor in a mouse body. (b) Blood vessels in a human body. The images are obtained with the commercial system AcousticX (https://www.cyberdyne.jp).

It can be clearly seen in Fig. 7.1 that only the boundaries of the tumor (a) and those of the blood vessels (b) are visible in the PA images. The reason is that large (compared to the acoustic wavelength λ_{ac}) absorbers produce PA signals with a strong

low-frequency component that is usually filtered out by the transfer function of the receiving US probe. As a result, it is the boundaries of large absorbers that are mostly present after reconstruction. This effect can be referred as the limited-bandwidth problem. One other problem is that structures elongated in some directions are not fully reconstructed. PA imaging of elongated structures leads to interference effects resulting in formation of PA waves that favours some directions rather than others. When the field of view of the US probe does not cover all the angles, such PA waves may escape detection and the related PA absorbers may not be entirely reconstructed. This effect can be referred as the limited-view problem. The limited-view problem is illustrated in Fig. 7.1a which reveals horizontal bright boundaries but does not display the vertical ones.

7.1.2 State-of-the-art

Many studies devoted to suppression of PA imaging artifacts considered the limited-view problem only. Particularly, acoustic waves propagating in various directions can be captured by rotating a linear transducer around the object [Yang et al., 2007] or by rotating the imaged object itself [Kruger et al., 2003]. It has also been proposed to place additional US transducers [Shu et al., 2016] to augment the detection view of a single transducer array. Instead of additional transducers, acoustic reflectors can be placed at boundaries of the imaging zone [Huang et al., 2013; Li et al., 2015]. In such a case, reconstruction can be improved by taking into account reflected PA signals that can be separated in time from PA waves directly emitted in the direction of the US probe. As an extreme case, the imaged object can be placed inside a reverberating cavity [Cox et al., 2007; Ellwood et al., 2014; Cox and Beard, 2009]. This allows detection of PA waves emitted in all possible directions even if a single element transducer is used [Cox and Beard, 2009].

A major disadvantage of the mentioned methods is that some angles can be inaccessible for transducers and reflectors in real clinical imaging. In addition, using acoustic reflectors requires perfect knowledge of acoustic properties of the propagation medium and the reflectors.

Other techniques eliminate interference effects by creating small PA sources inside the imaged object. Such methods can potentially handle both limited-view and limited-bandwidth problems. For example, artificial PA sources can be created by heating the sample locally by means of focused ultrasound [Wang et al., 2015]. By scanning the whole volume with an US beam and accumulating PA images obtained at each point, the entire object is reconstructed. However, this approach is time-consuming and limited by safety thresholds of ultrasound in medical use. It has also been proposed to tackle visibility issues by using moving absorbers whose distribution in the imaging zone is

random at any time moment. The reconstruction image can then be computed as the pixelwise sum of non-negative PA images obtained by model-based reconstruction at each laser shot [Deán-Ben et al., 2017]. A weak point of this method is the model-based approach that requires knowledge of the PSF and the so-called regularization parameter, the latter being difficult to estimate (see Chapter 5). Alternatively, if moving absorbers are sparsely distributed inside the sample, visibility artifacts can be eliminated by PA localization [Dean-Ben and Razansky, 2018]. However, the need for sparsely distributed absorbers entails the use of contrast agents and may extend considerably the acquisition time. One other method consists in creating fluctuating point-like PA sources by using random optical speckle patterns [Gateau et al., 2013]. In this case, the reconstruction image is obtained by calculating a statistical property of each pixel over a series of PA images, each image corresponding to a different speckle pattern. However, using optical speckle illuminations in clinical imaging is challenging as the small fluctuation signal can be difficult to distinguish on the strong background when imaging is performed at depths exceeding several millimeters (see section 1.4).

7.1.3 Principles of the proposed approach

As Gateau et al. [Gateau et al., 2013], we propose to handle visibility issues by computing the variance of PA images based on fluctuations of optical absorbers. However, we shall consider fluctuations originating from moving optical absorbers rather than from optical speckles. Importantly, we propose that red blood cells (RBCs) play the role of moving absorbers since fluctuations of RBCs are intrinsic to blood vessels and the usage of these fluctuations would therefore eliminate the need for contrast agents in clinical imaging.

To demonstrate that variance-based imaging relying on RBCs fluctuations can successfully eliminate visibility artifacts, we report results of three proof-of-concept PA experiments, each carried out for a vessel-mimicking sample in which a flow of human blood was induced. In this Chapter, we also conduct numerical simulations in order to understand the physics of the proposed approach and determine its limitations.

7.2 Proof-of-principle experimental demonstration

7.2.1 Materials and methods

7.2.1.1 Samples

Fig. 7.2 illustrates the imaging geometries used in the PA experiments and computer simulations. The first experiment consisted in imaging a C-shaped structure formed by a polycarbonate (PC) capillary (inner diameter D = 100 μm, wall thickness w = 20 μm, Paradigm Optics Inc., Vancouver, USA) whereas the second and the third experiments

consisted in imaging a cross-section of a glass tube (inner diameter D = 1 mm, wall thickness w = 100 μm, Capillary Tube Supplies Ltd, UK) placed perpendicularly to the imaging plane and inside the imaging plane correspondingly. In each experiment, the center of the sample is placed at the US probe (type L22-8) elevational focus distance z_f = 15 mm. The blood flow inside the sample is assured at a constant physiological rate (1.7 cm/s for the PC capillary, 1 cm/s for the glass tube).

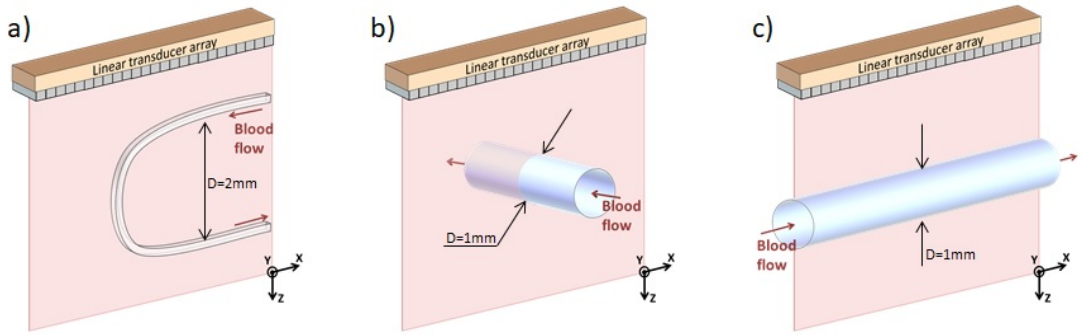

Fig. 7.2 Imaging geometries used in experiments and simulations. (a) A C-shaped capillary loop (D = 100 μm) lying in the imaging plane. (b) A tube (D = 1 mm) lying perpendicular to the imaging plane. (c) A tube (D = 1 mm) lying in the imaging plane parallel to the US transducer array.

7.2.1.2 Measurement protocols

The experimental setup is shown in Fig. 2.1. In each experiment, radio-frequency (RF) signals are acquired by illuminating the sample with flowing blood by laser pulses (τ_{pulse} = 5 ns, PRR = 100 Hz) at λ_{laser} = 532 nm (C-shaped sample) or at λ_{laser} = 680 nm (glass tube). For additional information on the imaging equipment the reader is referred to Chapter 2.

The wavelength λ_{laser} = 680 nm was used for imaging the glass tube due to the high absorption of blood at 532 nm. While for the thin C-shaped capillary the illumination could be considered almost uniform within the sample, for the glass tube with a much larger cross-section the light intensity decline on the tube diameter might be considerable. Blood absorption at 680 nm ($\mu_a \sim 1$ mm^{-1}) being much smaller than at 532 nm ($\mu_a \sim 10$ mm^{-1}), it is λ_{laser} = 680 nm that was chosen for imaging the glass tube sample.

The total number of acquired RF frames are N = 1,000 (C-shaped capillary), N = 10,000 (glass tube, perpendicular orientation), N = 1,000 (glass tube, parallel orientation) resulting in the total experiment time of T_{exp} = 10 s, T_{exp} = 100 s, and T_{exp} = 10 s for the first, second, and third experiments correspondingly.

7.2.1.3 Image reconstruction

To perform PA reconstruction, we first assembled complex RF data by merging the real part consisting of the acquired RF data and the imaginary part obtained by applying columnwise Hilbert transform to the acquired RF data. Then, complex beamformed images (or IQ images) were obtained by separately beamforming the real and the imaginary parts of the complex RF data (see Appendix 1). Afterwards, we proceeded with the removal of correlated images. To do so, we determined the fluctuation decorrelation rate by computing correlation between the real components of successive IQ images after removing from each reconstruction pixel k its mean value $< s_k >$. For the remaining M uncorrelated complex IQ images, we computed the mean image and the standard deviation image by calculating for each pixel k the complex mean $< s_k >= \frac{1}{M}\sum_{i=1}^{M} s_k(i)$ and the complex variance $\sigma_k^2 = \frac{1}{M}\sum_{i=1}^{M}(s_k(i) - < s_k >)(s_k(i) - < s_k >)^*$. At the final step of the reconstruction we obtained the envelope image by taking the module of the complex mean image and the standard deviation image by taking the square root of the variance image.

Before computing the standard deviation image for the experimental data, we applied spatiotemporal filtering through singular value decomposition (SVD) to the complex IQ data in order to reduce the impact of the laser noise appearing as unstable horizontal lines on RF data. In brief, SVD decomposes the initial data into a basis of spatiotemporal singular vectors. By choosing carefully the singular vectors corresponding to relevant fluctuations, one can discard signals with different spatiotemporal behaviour such as tissue clutter, laser and electronic noise, etc. Specifically, in our experiments the laser noise was empirically found to reside in the first 21 singular vectors, whereas the information about the fluctuations turned out to be encoded in the following 49 vectors. All singular vectors with indices $i > 70$ were attributed to the electronic noise of the acquisition system. So, by choosing the singular vectors with indices i = 22...70 we managed to clean the acquired data not only from the laser noise but also from the electronic noise. More details on the SVD approach can be found in Appendix 3.

7.2.2 Results

7.2.2.1 C-shaped sample

To test the proposed approach in the limited-view scenario, we carried out an experiment with the C-shaped capillary lying in the imaging plane (Fig. 7.2a). The experimental results are demonstrated in Fig. 7.3. First, due to the limited view problem, the vertical segment of the sample does not appear in the mean image: interference effects lead to PA waves that propagate parallel to the surface of the transducer array

and therefore can not be captured. In contrast, the fluctuation-based image reveals the previously invisible part. However, the apparent reconstruction is not fully homogenous (contrary to the simulation results presented below). A possible reason is that the SVD spatiotemporal filtering applied in order to remove the noise affects some useful signal as well.

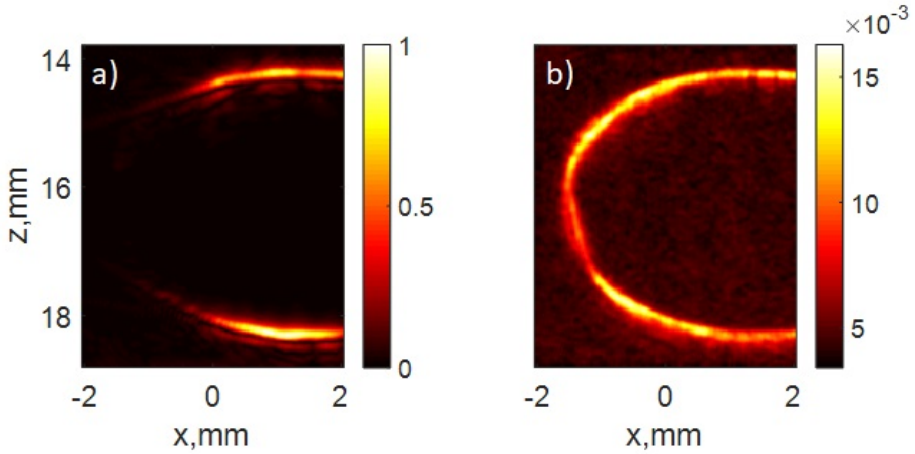

Fig. 7.3 Experimental results obtained for the C-shaped capillary (see Fig.7.2a) and human blood flowing through the sample. Reconstruction is based on N = 1,000 PA images, experiment duration T_{exp} = 10 s. (a) Mean envelope PA image leads to a deficient reconstruction, the vertical segment disappears due to the limited-view problem. (b) Fluctuation-based reconstruction recovers the entire object.

7.2.2.2 Straight line tube sample

To test the proposed approach in the limited-bandwidth scenario, we carried out an experiment with a glass tube placed perpendicularly (Fig. 7.2b) to the imaging plane and inside (Fig. 7.2c) the imaging plane. The experimental results are demonstrated in Fig. 7.4. First, due to the limited-bandwidth problem, the central part of the sample does not appear in the mean image: the tube diameter D = 1 mm is by an order of magnitude greater than the acoustic wavelength λ_{ac} = 0.1 mm (for the central frequency of transducer f_c = 15 MHz and the speed of sound in water v_s = 1500 m/s). Second, due to the limited-view problem, the left and the right vertical boundaries of the tube in Fig. 7.4a are not visible since only the upper and the lower horizontal boundaries emit PA waves towards the transducer array. In contrast, the fluctuation-based reconstruction provides a faithful image of the object. The appearance of clutter below the object in Fig. 7.4b,d is probably related to signal reverberations within the walls of the glass tube.

It should be emphasized that in order to discard correlated images we took every 10th image in the experiment with the perpendicular tube orientation (see Fig. 7.2b)

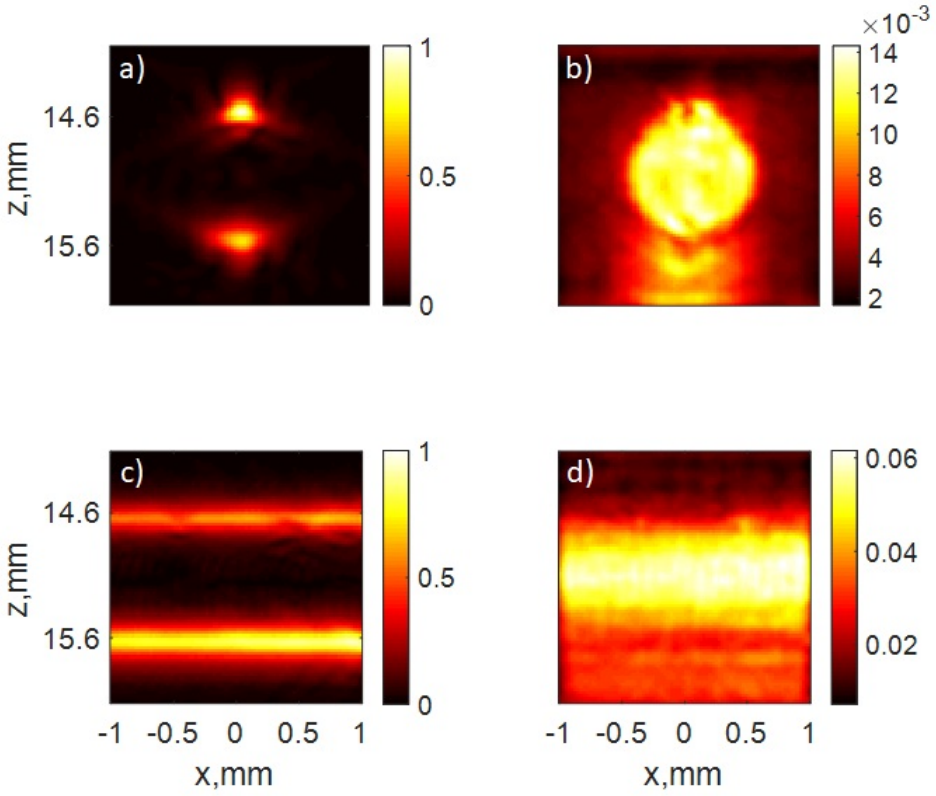

Fig. 7.4 Experimental results obtained for the glass tube oriented perpendicularly (a,b) and parallel (c,d) to the imaging plane (see Fig.7.2b,c) and human blood flowing through the sample. Reconstruction is based on N = 1,000 PA images, experiment duration: (a,b) - T_{exp} = 100 s, (c,d) - T_{exp} = 10 s. (a,c) Mean envelope PA image leads to a prominent buildup of the sample boundaries, the central part disappears due to the limited-bandwidth problem. (b,d) Fluctuation-based reconstruction recovers the entire object.

while in the two other experiments (see Fig. 7.2a,c) we took every single image. The difference in the decorrelation rate results from different decorrelation distances determined by the ΔX, ΔY, and ΔZ dimensions of the acoustic PSF for displacements in the X, Y, and Z directions correspondingly. In the conditions of our experiments, the estimated full width at half maximum (FWHM) of the PSF in the X, Y and Z directions turned out to be ΔX = 154 μm, ΔY = 1 mm, and ΔZ = 118 μm correspondingly. Hence, at the laser PRR of 100 Hz and the flow rate of 1 cm/s, any 10 successive images corresponding to the perpendicular tube orientation (along the Y direction) could be considered correlated. So, 90 % of the images obtained for the perpendicular tube orientation were discarded. As a result, we had to acquire 10,000 PA images and take only 1,000 of them which increased the experiment time T_{exp} by a factor of 10.

7.3 Theoretical analysis

In this section we investigate the mechanism by which the proposed approach leads to suppression of visibility artifacts. In particular, we shall study how the amplitude of the fluctuation signal depends on the volume fraction of absorbers and the number of absorbers per acoustic PSF.

7.3.1 Theoretical model

In the case of absorbers flowing in a static structure, the distribution of optical absorption can be expressed as

$$\alpha_k(\overrightarrow{r}) = \mu_0[f(\overrightarrow{r}) \times g_k(\overrightarrow{r})], \tag{7.1}$$

where μ_0 is the optical absorption of the material of absorbers, $g_k(\overrightarrow{r})$ is the distribution of absorbers at laser shot k, and $f(\overrightarrow{r})$ is the object structure. PA reconstruction image A_k corresponding to laser shot k can thus be written as:

$$A_k(\overrightarrow{r}) = I_0[\alpha_k(\overrightarrow{r}) * h(\overrightarrow{r})], \tag{7.2}$$

where I_0 is the light intensity and $h(\overrightarrow{r})$ is the bipolar PSF in the beamforming space.

By averaging over M PA images, one obtains

$$< A_k(\overrightarrow{r}) > \sim < \alpha_k(\overrightarrow{r}) * h(\overrightarrow{r}) > \xrightarrow{M\to\infty} \mu_0\eta[f(\overrightarrow{r}) * h(\overrightarrow{r})], \tag{7.3}$$

where $\eta =< g_k(\overrightarrow{r}) >$ is the volume fraction of absorbers that are assumed homogeneously distributed.

Now we shall compute the variance PA image

$$\begin{aligned} \sigma^2[A](\overrightarrow{r}) \sim & < \int (\alpha(\overrightarrow{r}\prime) - < \alpha(\overrightarrow{r}\prime) >) h(\overrightarrow{r} - \overrightarrow{r}\prime) d\overrightarrow{r}\prime \times \\ & \times \int (\alpha(\overrightarrow{r}\prime\prime) - < \alpha(\overrightarrow{r}\prime\prime) >) h(\overrightarrow{r} - \overrightarrow{r}\prime\prime) d\overrightarrow{r}\prime\prime > = \\ & = \iint C(\overrightarrow{r}\prime, \overrightarrow{r}\prime\prime) h(\overrightarrow{r} - \overrightarrow{r}\prime) h(\overrightarrow{r} - \overrightarrow{r}\prime\prime) d\overrightarrow{r}\prime d\overrightarrow{r}\prime\prime, \end{aligned} \tag{7.4}$$

where $C(\overrightarrow{r}\prime, \overrightarrow{r}\prime\prime) =< (\alpha(\overrightarrow{r}\prime) - < \alpha(\overrightarrow{r}\prime) >)(\alpha(\overrightarrow{r}\prime\prime) - < \alpha(\overrightarrow{r}\prime\prime) >) >$ is the covariance of absorption distribution.

Assuming that the absorbers are sufficiently small compared to the PSF, the covariance $C(\overrightarrow{r}\prime, \overrightarrow{r}\prime\prime)$ can be considered proportional to the delta function $\delta(\overrightarrow{r}\prime - \overrightarrow{r}\prime\prime)$, so $C(\overrightarrow{r}\prime, \overrightarrow{r}\prime\prime) = \sigma_\alpha^2(\overrightarrow{r}\prime)\delta(\overrightarrow{r}\prime - \overrightarrow{r}\prime\prime)$, where $\sigma_\alpha^2(\overrightarrow{r}\prime)$ is the variance of absorption distribution.

If at laser shot k there is an absorber at point $\overrightarrow{r}$ then $g_k(\overrightarrow{r}) = 1$, otherwise

$g_k(\overrightarrow{r}) = 0$. In addition, if the absorbers are uniformly distributed inside the sample then the probability to find an absorber at any point $\overrightarrow{r}$ is equal to the volume fraction of absorbers η. Such statistical properties describe a Bernoulli distribution, so for the variance $\sigma_\alpha^2(\overrightarrow{r})$ one can write $\sigma_\alpha^2(\overrightarrow{r}) = \mu_0^2\eta(1-\eta)f^2(\overrightarrow{r})$.

Thus,

$$\sigma^2[A](\overrightarrow{r}) \sim \mu_0^2\eta(1-\eta)\int f^2(\overrightarrow{r}')h^2(\overrightarrow{r}-\overrightarrow{r}')d\overrightarrow{r}' = \mu_0^2\eta(1-\eta)[f^2(\overrightarrow{r}) * h^2(\overrightarrow{r})]. \tag{7.5}$$

Contrary to reconstruction (7.3) that leads to feature suppression due to strong interference effects resulting from convolution with the bipolar PSF $h(\overrightarrow{r})$, fluctuation-based reconstruction (7.5) recovers the entire object as interference effects are avoided by convolution with the positive $h^2(\overrightarrow{r})$. In other words, while PA signals interfere either constructively or destructively depending on the part of the object considered, variance signals from independent fluctuating sources always sum up incoherently.

For complex IQ data, complex variance can be computed by replacing $h(\overrightarrow{r}-\overrightarrow{r}'')$ in Eq. (7.4) with its complex conjugate $h^*(\overrightarrow{r}-\overrightarrow{r}'')$. This will smooth out the PSF-related oscillations in the reconstruction image as the object $f^2(\overrightarrow{r})$ will be convoluted with the smooth PSF envelope $|h(\overrightarrow{r})|^2$:

$$\sigma^2[A](\overrightarrow{r}) \sim \mu_0^2\eta(1-\eta)[f^2(\overrightarrow{r}) * |h(\overrightarrow{r})|^2]. \tag{7.6}$$

7.3.2 Validation in numerical simulations

7.3.2.1 Principle of the numerical simulations

To perform numerical simulations, for each of the imaging geometries shown in Fig. 7.2 we modelled radio frequency (RF) PA signals associated with randomly generated patterns of sources in the imaging plane. Each pattern was obtained by discretizing the imaged cross-section on a grid with a step corresponding to the absorber diameter D_a and assigning with a certain probability p a virtual source to each point of this grid. Typical patterns corresponding to the perpendicular tube orientation are shown in Fig. 7.5. The probability p was taken equal to the imposed volume fraction of sources η.

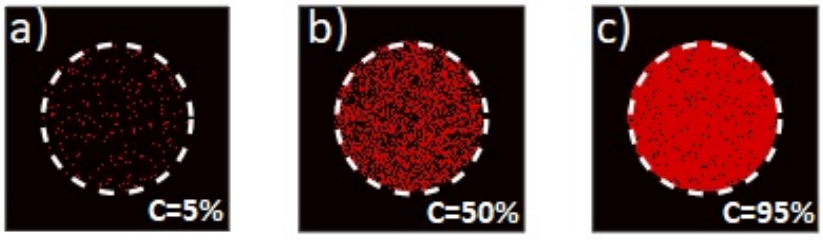

Fig. 7.5 Typical simulation patterns for different volume fraction η of sources. (a) η = 5%, (b) η = 50%, (c) η = 95%.

The simulation signals were generated using the 2D version of SimSonic, finite-difference time-domain simulation software (www.simsonic.fr) which models propagation of acoustic waves (including PA waves). Photoacoustic sources were defined with random patterns such as those presented in Fig. 7.5. For each pattern, a set of PA signals was recorded by 128 virtual point-like detectors. As in all our simulations, the detected signals had the central frequency and the bandwidth corresponding to those used in experiments, with the same final sampling frequency as in experiments after downsampling the simulated signals.

Two kinds of simulation data were generated, based on two different types of random absorbers distributions. First, different values of volume fraction η = 5%, 25%, 40%, 50%, 60%, 75%, 95% were chosen with D_a corresponding to an approximate RBC diameter $D_a = D_{rbc}$ = 10 μm. Second, different source diameters D_a = 2.5 μm , 5 μm, 7.5 μm, 10 μm, 15 μm, 20 μm, 25 μm were chosen with the volume fraction η corresponding to the average RBCs volume fraction in human blood $\eta = \eta_{RBC}$ = 50%. For each D_a the number of sources per acoustic PSF was calculated as $N_s = \Delta X \times \Delta Z / D_a^2$, where ΔX and ΔZ is the full width at half maximum (FWHM) of the PSF along the X and Z axes respectively (ΔX = 154 μm, ΔZ = 118 μm). In total, for each η ($D_a = D_{rbc}$) and each N_s ($\eta = \eta_{RBC}$), 100 RF data frames were generated based on 100 random patterns.

7.3.2.2 Influence of the volume fraction (fixed absorber)

To study the influence of the volume fraction η on PA reconstruction, we computed the mean and the variance PA images for different η and fixed absorber diameter D_a corresponding to the average RBC size $D_a = D_{RBC} = 10\ \mu m$.

Fig. 7.6 and 7.7 show simulation results for the C-shaped sample and the round tube obtained for η = 50%. It can be seen that as in experiments, fluctuation-based reconstruction recovers the entire object whereas some object parts are missing on the mean image due to the limited-view and limited-bandwidth problems.

Fig.7.8 shows how the mean signal from the object boundaries and the fluctuation signal from the inner part of the object depend on the volume fraction η. First, as predicted by Eq. (7.3) the boundary buildup is proportional to the concentration of absorbers. As concerns the fluctuation signal, the Bernoulli standard deviation predicted by Eq. (7.6) is fully validated. So, the standard deviation curve has a domed shape with a single maximum at η = 50%. It is worth mentioning that this maximum is of primary interest for reconstruction based on blood flow fluctuations as the average RBCs volume fraction in human blood is very close to η = 50%.

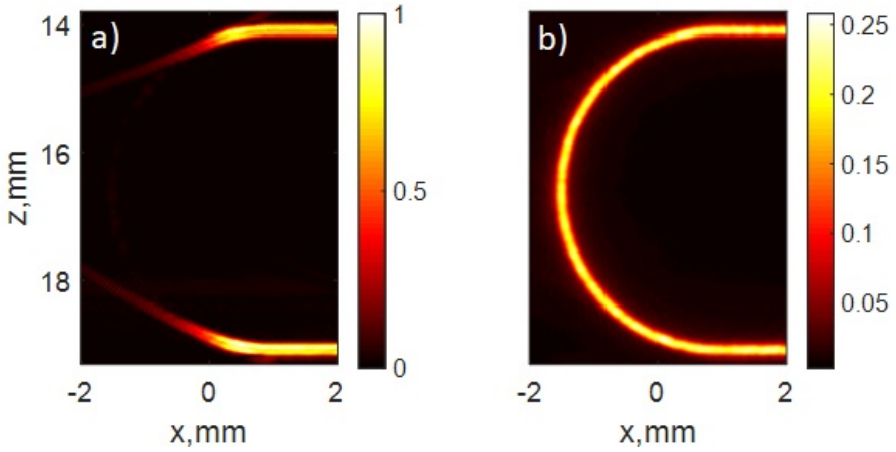

Fig. 7.6 Simulation results obtained for the C-shaped capillary (see Fig.7.2a) and the volume fraction of sources $\eta = 50\%$. (a) Mean envelope PA image leads to a deficient reconstruction, the vertical segment disappears due to the limited-view problem. (b) Fluctuation-based reconstruction recovers the entire object.

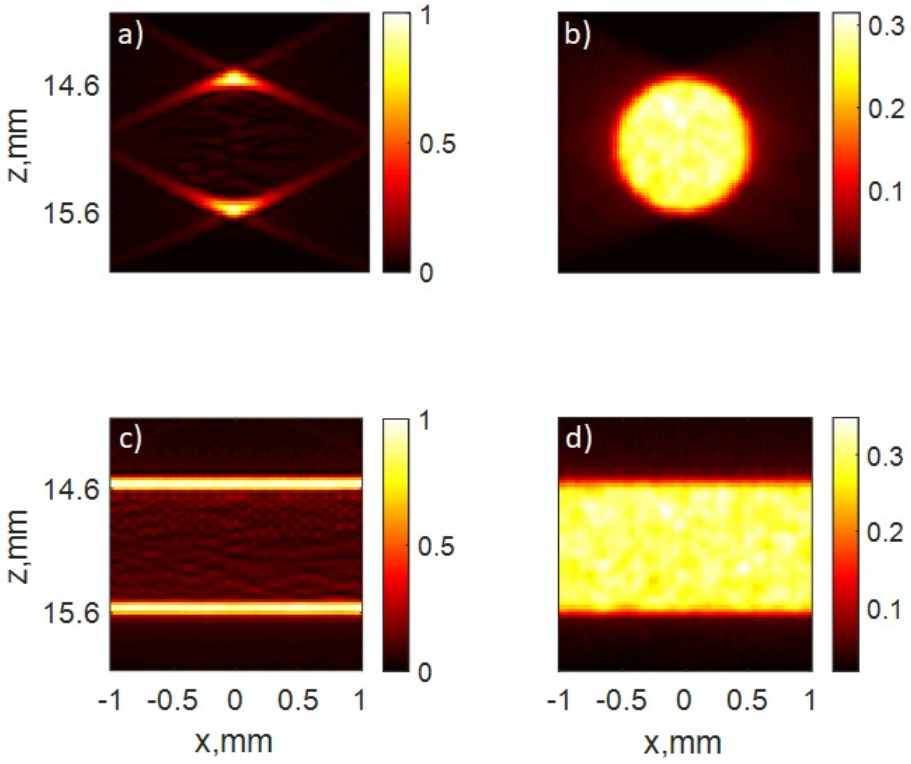

Fig. 7.7 Simulation results obtained for the glass tube oriented perpendicularly (a,b) and parallel (c,d) to the imaging plane (see Fig.7.2b,c) and the volume fraction of sources $\eta = 50\%$. (a,c) Mean envelope PA image leads to a prominent buildup of the sample boundaries, the central part disappears due to the limited-bandwidth problem. (b,d) Fluctuation-based reconstruction recovers the entire object.

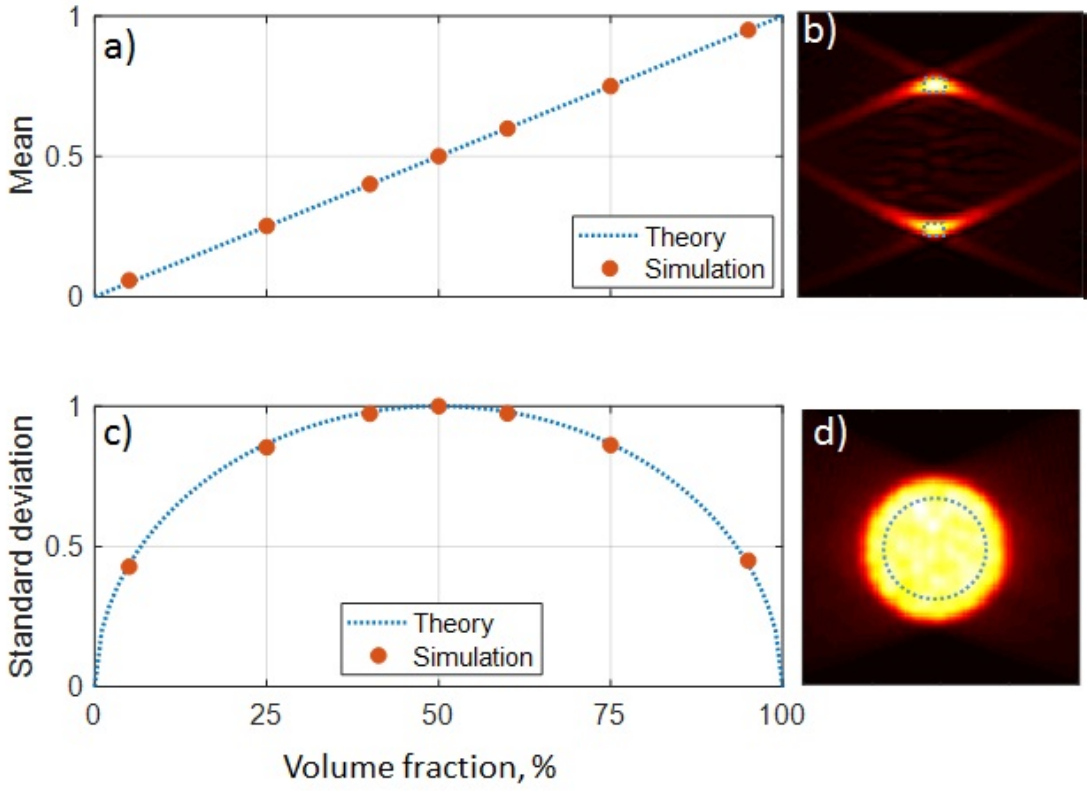

Fig. 7.8 Simulation results for different volume fraction η, the absorber diameter is D_{rbc} = 10 μm. (a) The mean signal from sample boundaries is proportional to the concentration of sources. (b) Typical mean image, dotted rectangles: regions used to compute the mean value in (a). (c) The standard deviation calculated for the central part of the object has a domed shape and reaches its maximum at η = 50% corresponding to the RBCs volume fraction in human blood. (d) Typical standard deviation image, dotted circle: region used to compute the standard deviation value in (c).

This being said, the maximum at $\eta = 50\%$ to a certain extent dictates the SNR required for reconstruction based on blood flow fluctuations. As the noise variance is to be subtracted from the reconstruction image, the variance corresponding to RBCs fluctuations should be greater than the error in estimation of noise variance. In addition, the number M of acquired PA images should be high enough to provide a robust estimate of signal variance for all points of the imaged object. As the error in variance estimation is proportional to $1/M$, the reconstruction quality is only limited by the experiment duration, provided that the sample and noise remain stationary during the total acquisition time.

7.3.2.3 Influence of the absorber dimension (fixed average absorption)

To study the influence of the number of absorbers N_a per acoustic PSF on PA reconstruction, we computed the mean and the variance PA images for different N_a and fixed

volume fraction of absorbers η corresponding to the RBCs volume fraction in human blood $\eta = \eta_{RBC} = 50\%$.

The simulation results are shown in Fig. 7.9. It can be noticed that the standard deviation approaches the $A/\sqrt{N_a}$ ($A = const$) law when the number of absorbers becomes large. The observed deviation from the theoretical $1/\sqrt{N_a}$ curve for small N_a is probably related to transition to another regime where the bandwidth-limited effects become significant due to the PSF getting smaller than an individual absorber.

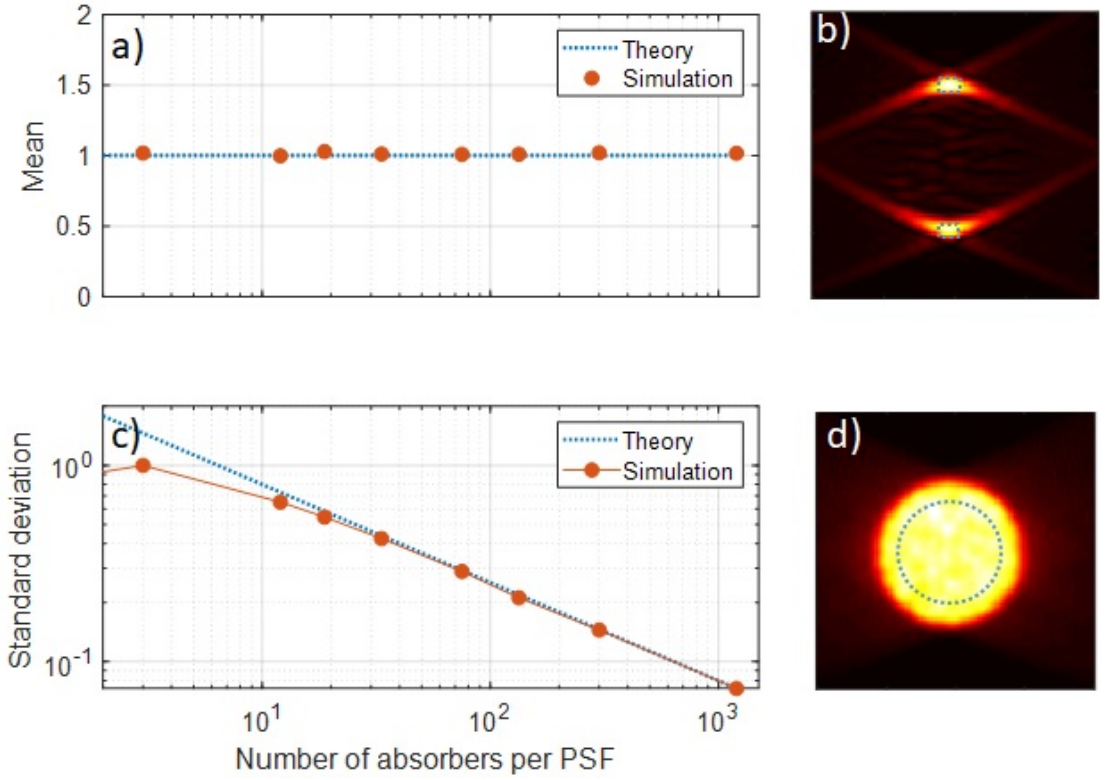

Fig. 7.9 Simulation results for different number N_a of absorbers per PSF, the absorbers volume fraction is η = 50%. (a) The mean signal from sample boundaries is independent of the number of absorbers. (b) Typical mean image, dotted rectangles: regions used to compute the mean value in (a). (c) The standard deviation approaches the fitting $A/\sqrt{N_a}$ ($A = const$) curve when the number of absorbers becomes large. (d) Typical standard deviation image, dotted circle: region used to compute the standard deviation value in (c).

The $A/\sqrt{N_a}$ law explains why using RBCs fluctuations may outperform the approach based on optical speckle fluctuations. Indeed, the number of 10-μm RBCs inside the $\Delta X \times \Delta Y \times \Delta Z$ = 154 $\mu m \times$ 1 mm $\times$ 118 μm volume of the PSF is around $N_{RBC} \sim 10^4$ whereas the number of optical speckles (speckle size is $\lambda_{laser}/2 \sim 0.3$ μm at ~1 mm depth in biological tissues under near infrared [Ntziachristos, 2010]) is around $N_{sp} \sim 10^8$. So, the fluctuation signal from optical speckles is by several orders of magnitude weaker than the fluctuation signal from RBCs. As a result, it should

be much more difficult to distinguish the weak fluctuation signal over the strong background when using optical speckle illuminations.

7.4 Conclusion

We demonstrated that PA visibility artifacts caused by limited view and limited bandwidth of the US probe can be suppressed by using fluctuations of moving RBCs. In particular, visibility artifacts can be eliminated on the variance PA image.

In numerical simulations, we demonstrated that the RBC volume fraction in human blood turns out to be close to the value optimizing the amplitude of the fluctuation signal. Moreover, we established that the fluctuation amplitude decreases with the number of fluctuating photoacoustic sources N_a inside the acoustic PSF as $1/\sqrt{N_a}$ which explains why using optical speckle fluctuations [Gateau et al., 2013] to overcome visibility problems is impractical in deep-tissue imaging.

The temporal resolution of the proposed technique is limited by the fluctuation statistics as calculating statistical properties requires a certain number of PA images. However, based on blood fluctuations that are naturally present in living tissues, our approach does not require contrast agents. In addition, the implementation of the proposed technique is straightforward as it does not need any additional equipment. This makes the proposed method attractive for biomedical deep-tissue imaging.

CHAPTER 8

Conclusion

8.1 Main results

In chapters 3-5 of this PhD study we proposed several methods to overcome the acoustic diffraction barrier in photoacoustic (PA) imaging. For experimental demonstration of each method, we performed cross-sectional imaging of five parallel microchannels. Being indistinguishable on the standard reconstruction image, the microchannels were well reconstructed by most of the proposed techniques. In chapter 7 we proposed a new method to overcome visibility problems in PA imaging. The main results of each chapter can be summarized as follows.

In the third chapter, localization-based PA imaging was proposed. In the experiment, microchannels separated by 75 μm (conventional resolution limit being around 154 μm) were resolved by acquiring a series of PA images for a diluted suspension of microbeads passing through the channels. Using numerical simulations, we demonstrated that when the signal-to-noise ratio (SNR) is low, a single microbead is localized more precisely on the beamforming (BF) image that on the raw radio-frequency (RF) data. When the SNR is high, localization in the RF- and in the BF-space provides equivalent results. By adding artificial noise to the experimental data, we showed that the matched filter approach in the BF-space can improve localization results. The advantages and disadvantages of PA localization-based imaging are similar to those of ultrasound (US) localization. Regarding the advantages, the method can in principle provide an infinite resolution and is based on a relatively simple signal processing. As for the disadvantages, the method provides a very low temporal resolution and requires diluted contrast agents to perform clinical imaging.

In the fourth chapter, fluctuation-based imaging (photoacoustic SOFI) was proposed. In the proof-of-principle experiment, microchannels separated by 180 μm (conventional resolution limit being around 200 μm) were resolved by exploiting fluctuations of a flow of human blood passing through the channels. We showed that as in optics [Dertinger et al., 2009], the n-th order cumulant calculated over the initial pixel time series provides a $\sqrt{n}$ resolution improvement. We also developed a complex cumulant framework that permits correcting PSF-related artifacts on the cumulant im-

age. A major advantage of the proposed technique is that it can potentially be used for contrast-free imaging of microvasculature where blood flow fluctuations are a natural source of PA signal fluctuations. However, we observed that separating relevant fluctuations from noise can be challenging. One other limitation is that objects associated with stronger PA signals mask objects associated with weaker PA signals when high order cumulants are computed. Finally, as PA super-localization, fluctuation-based PA imaging has a low temporal resolution. At low blood velocities, the temporal resolution is limited by the requirement for uncorrelated PA images. At high blood velocities, the temporal resolution is limited by the imaging rate. In addition, the number of required PA acquisitions increases with the cumulant order n.

In the fifth chapter, we proposed to use model-based reconstruction to achieve super-resolution in single-shot PA imaging. In the proof-of-principle experiment, microchannels separated by 125 μm (conventional resolution limit being around 155 μm) were resolved in sparsity-based reconstruction. Other model-based reconstruction techniques (Moore-Penrose pseudoinverse, Tikhonov regularization, positivity-based reconstruction) did not provide a super-resolved image of the sample. In this experiment, we also demonstrated that model-based reconstruction applied to RF and BF data generates equivalent results. In another experiment we sought the minimal separation between two point sources that can be resolved in sparsity-based reconstruction. Experimentally, we managed to resolve two sources separated by 80 μm (conventional resolution limit being around 398 μm) which was the smallest distance available on the sample. In additional noise-free numerical simulations we determined that sparsity-based reconstruction can resolve two point sources separated down to 24 μm (conventional resolution limit being around 398 μm). This resolution limit may depend on the PSF variability in the imaging zone, reconstruction algorithm and available numerical precision. To understand better the mechanism of sparsity-based reconstruction, we performed a theoretical analysis. Based on this analysis, we admitted that the regularization parameter, which is crucial to provide the right solution in sparsity-based reconstruction, can hardly be predicted without using additional (not related to sparsity-based reconstruction) information about the imaged object. Moreover, it was demonstrated that it is hard to predict whether sparsity-based reconstruction will provide the right object at any value of the regularization parameter. We showed, however, that super-resolution can also be obtained in model-based reconstruction by using the non-negativity constraint only (without the regularization term). This approach does not need the regularization parameter but it is more sensitive to noise and its reliability is also questionable.

In the sixth chapter, we applied sparsity-based reconstruction in sparse-array imaging. In two proof-of-principle experiments, we performed single-shot PA and US imaging of the five microchannels (separated by 125 μm, conventional resolution limit being

around 155 μm) with a linear transducer array. We demonstrated that the reconstruction quality in super-resolution imaging does not degrade significantly while using much less transducer elements when used conventionally (8 elements against 128). In numerical simulations, we showed that for any SNR there is the minimal number of transducer elements that is required to provide the desired reconstruction quality. This number decreases with the growth of the SNR. At a very high SNR only two elements can be sufficient for reconstruction.

In the seventh chapter, we demonstrated that PA signal fluctuations caused by a blood flow can be successfully used in PA imaging to eliminate visibility artifacts due to limited-view and limited-bandwidth problems. In particular, we demonstrated that such artifacts disappear on the variance PA image. The advantages and disadvantages of the method are the same as for fluctuation-based super-resolution imaging.

In the frames of this PhD study two papers came out [Vilov et al., 2017; Chaigne et al., 2017]. Meanwhile, another group explored PA super-localization and their results were published [Dean-Ben and Razansky, 2018] at the same time as ours. In that work of Dean-Ben et al. [Dean-Ben and Razansky, 2018] localization-based imaging was performed in three dimensions, whereas in our study we demonstrated a more significant resolution improvement. In addition, when we had obtained the main results of chapter 5, Egolf et al. [Egolf et al., 2018] published their results on sparsity-based reconstruction in super-resolution PA imaging. However, their study was limited to a single experimental demonstration, without comparing sparsity-based reconstruction with other model-based techniques and without any discussion on the regularization parameter and the non-negativity constraint.

8.2 Discussion and perspectives

Each of the proposed PA super-resolution methods has advantages and drawbacks and the choice of a particular method will be conditioned by the needs and limitations of a particular application. Thus, for example, from the point of view of the possible resolution limit, localization-based imaging is probably the best. However, among all the studied methods, super-localization provides the worst temporal resolution. The temporal resolution of fluctuation-based imaging is only slightly better, although numerical implementation of this method is probably the easiest. So, among all the studied methods, model-based reconstruction is the only method appropriate for dynamic single-shot imaging. In addition, model-based reconstruction is the method of choice when super-resolution should be obtained in sparse-array imaging. However, implementation of model-based reconstruction is complex and the corresponding reconstruction might be unreliable.

Some of the considered methods might be combined to satisfy the needs of a partic-

ular application. Thus, for example, inspired by the SUSHI approach [Bar-Zion et al., 2018], we combined fluctuation-based imaging and sparsity-based reconstruction (see chapter 5). In numerical simulations, we observed that this permits obtaining resolution $\sqrt{2}$ times better than in classical sparsity-based reconstruction but with the temporal resolution of the fluctuation-based approach. One other idea is to perform sparsity-based reconstruction as a part of super-localization, as proposed in [Shu et al., 2018]. If the limitations of the model-based approach could be overcome this would improve temporal resolution of super-localization by allowing higher concentrations of contrast agents.

So, further studies are needed to handle the limitations of each of the proposed methods. For example, it is important to find a reliable method for separating relevant fluctuations from noise in fluctuation-based imaging. To this end, we employed SVD filtering, but it was based on the choice of relevant singular vectors which was made with the knowledge of the imaged object. As concerns sparsity-based reconstruction, the main limitation is the choice of the regularization parameter that reconstruction crucially depends on. In this study, the regularization parameter was also determined with the knowledge of the imaged object. A possible solution would be to use the deep learning framework trained with pairs consisting of input PA data and corresponding regularization parameters. Some combinations of the deep learning and sparsity-based techniques have already been proposed [van Sloun et al., 2018].

Despite the present limitations, most of the methods proposed in this PhD study are based on basic signal processing and do not require extra imaging equipment. They can be, therefore, straightforwardly implemented in commercial and scientific PA imaging systems. In this regard, it should be emphasized that some of our results have already formed the basis for an *in vivo* study in the field. In particular, PA localization based on biocompatible dyed droplets was employed to obtain 3D super-resolved images of the cortical layer of the mouse brain [Zhang et al., 2019].

Finally, I would like to note that in the frames of my PhD study I designed two multielement probes for 3D PA imaging.

The first probe, manufactured by Vermon S.A. (Tours, France), is a 256-element probe for super-resolution PA imaging with the center frequency of 25 MHz. The 0.25 mm $\times$ 0.5 mm rectangular-shaped elements of the probe are regularly distributed on a 20-mm diameter ring providing the focal distance of about 14 mm. In the center of the probe there is a 13-mm diameter hole to insert an optical fiber guiding laser light. The probe permits imaging in the zone of about $\Delta X \times \Delta Y \times \Delta Z \approx 2.5$ mm $\times$ 2.5 mm $\times$ 2.5 mm.

The second probe, manufactured by Imasonic SAS (Voray-sur-l'Ognon, France), is a 256-element universal probe with the center frequency of 8 MHz. The 2-mm diameter

round-shaped elements of the probe form a random pattern covering a semi-spherical aperture with a 35 mm radius. In the center of the probe there is a 8-mm diameter hole to insert an optical fiber guiding laser light. The probe permits imaging in the zone of about $\Delta X \times \Delta Y \times \Delta Z \approx 6$ mm $\times$ 6 mm $\times$ 10 mm.

Due to some technical difficulties, the probes arrived in our laboratory much later than expected. As a result, I did not manage to perform experiments with them due to the time constraint. However, with these probes our research group is currently investigating the application of the proposed methods for 3D super-resolution imaging. This constitutes a part of the PhD study of Guillaume Godefroy. In the frames of his study, *in vivo* experiments are also planned.

REFERENCES

(2000). Norme européenne, norme française nf en 60825-1.

Bar-Zion, A., Solomon, O., Tremblay-Darveau, C., Adam, D., and Eldar, Y. C. (2018). Sushi: Sparsity-based ultrasound super-resolution hemodynamic imaging. *IEEE Transactions on Ultrasonics, Ferroelectrics, and Frequency Control*, 65(12):2365–2380.

Baranger, J., Arnal, B., Perren, F., Baud, O., Tanter, M., and Demené, C. (2018). Adaptive spatiotemporal svd clutter filtering for ultrafast doppler imaging using similarity of spatial singular vectors. *IEEE transactions on medical imaging*, 37(7):1574–1586.

Beard, P. (2011). Biomedical photoacoustic imaging. *Interface focus*, 1(4):602–631.

Beck, A. and Teboulle, M. (2009). A fast iterative shrinkage-thresholding algorithm for linear inverse problems. *SIAM journal on imaging sciences*, 2(1):183–202.

Betzig, E. (1995). Proposed method for molecular optical imaging. *Optics letters*, 20(3):237–239.

Betzig, E., Patterson, G. H., Sougrat, R., Lindwasser, O. W., Olenych, S., Bonifacino, J. S., Davidson, M. W., Lippincott-Schwartz, J., and Hess, H. F. (2006). Imaging intracellular fluorescent proteins at nanometer resolution. *Science*, 313(5793):1642–1645.

Buehler, A., Rosenthal, A., Jetzfellner, T., Dima, A., Razansky, D., and Ntziachristos, V. (2011). Model-based optoacoustic inversions with incomplete projection data. *Medical physics*, 38(3):1694–1704.

Calasso, I. G., Craig, W., and Diebold, G. J. (2001). Photoacoustic point source. *Physical Review Letters*, 86(16):3550.

Chaigne, T., Arnal, B., Vilov, S., Bossy, E., and Katz, O. (2017). Super-resolution photoacoustic imaging via flow-induced absorption fluctuations. *Optica*, 4(11):1397–1404.

Chaigne, T., Gateau, J., Allain, M., Katz, O., Gigan, S., Sentenac, A., and Bossy, E. (2016). Super-resolution photoacoustic fluctuation imaging with multiple speckle illumination. *Optica*, 3(1):54–57.

Cheston, T. C. and Frank, J. (1990). Phased array radar antennas. In *Radar Handbook*, pages 7–1. McGraw-Hill New York, NY, USA.

Christensen-Jeffries, K., Browning, R. J., Tang, M.-X., Dunsby, C., and Eckersley, R. J. (2015). In vivo acoustic super-resolution and super-resolved velocity mapping using microbubbles. *IEEE transactions on medical imaging*, 34(2):433–440.

Cohen, R. and Eldar, Y. C. (2018). Sparse convolutional beamforming for ultrasound imaging. *IEEE transactions on ultrasonics, ferroelectrics, and frequency control*, 65(12):2390–2406.

Couture, O., Hingot, V., Heiles, B., Muleki-Seya, P., and Tanter, M. (2018). Ultrasound localization microscopy and super-resolution: A state of the art. *IEEE transactions on ultrasonics, ferroelectrics, and frequency control*, 65(8):1304–1320.

Cox, B. and Beard, P. (2009). Photoacoustic tomography with a single detector in a reverberant cavity. *The Journal of the Acoustical Society of America*, 125(3):1426–1436.

Cox, B. T., Arridge, S. R., and Beard, P. C. (2007). Photoacoustic tomography with a limited-aperture planar sensor and a reverberant cavity. *Inverse Problems*, 23(6):S95.

Dean-Ben, X. L., Buehler, A., Ntziachristos, V., and Razansky, D. (2012). Accurate model-based reconstruction algorithm for three-dimensional optoacoustic tomography. *IEEE Transactions on Medical Imaging*, 31(10):1922–1928.

Deán-Ben, X. L., Ding, L., and Razansky, D. (2017). Dynamic particle enhancement in limited-view optoacoustic tomography. *Opt. Lett.*, 42(4):827–830.

Dean-Ben, X. L. and Razansky, D. (2018). Localization optoacoustic tomography. *Light: Science & Applications*, 7(4):18004.

Demené, C., Deffieux, T., Pernot, M., Osmanski, B.-F., Biran, V., Gennisson, J.-L., Sieu, L.-A., Bergel, A., Franqui, S., and Correas, J.-M. (2015). Spatiotemporal clutter filtering of ultrafast ultrasound data highly increases doppler and fultrasound sensitivity. *IEEE transactions on medical imaging*, 34(11):2271–2285.

Dertinger, T., Colyer, R., Iyer, G., Weiss, S., and Enderlein, J. (2009). Fast, background-free, 3d super-resolution optical fluctuation imaging (SOFI). *Proceedings of the National Academy of Sciences*, 106(52):22287–22292.

Desailly, Y., Couture, O., Fink, M., and Tanter, M. (2013). Sono-activated ultrasound localization microscopy. *Applied Physics Letters*, 103(17):174107.

Diebold, G. and Sun, T. (1994). Properties of photoacoustic waves in one, two, and three dimensions. *Acta Acustica united with Acustica*, 80(4):339–351.

Egolf, D. M., Chee, R. K., and Zemp, R. J. (2018). Sparsity-based reconstruction for super-resolved limited-view photoacoustic computed tomography deep in a scattering medium. *Optics letters*, 43(10):2221–2224.

Eldar, Y. C. and Kutyniok, G. (2012). *Compressed sensing: theory and applications*. Cambridge university press.

Ellwood, R., Zhang, E., Beard, P., and Cox, B. (2014). Photoacoustic imaging using acoustic reflectors to enhance planar arrays. *Journal of Biomedical optics*, 19(12):126012.

Ephrat, P., Keenlislide, L., Seabrook, A., Prato, F. S., and Carson, J. J. (2008). Three-dimensional photoacoustic imaging by sparse-array detection and iterative image reconstruction. *Journal of Biomedical Optics*, 13(5):054052.

Eriksson, J., Ollila, E., and Koivunen, V. (2010). Essential statistics and tools for complex random variables. *IEEE Transactions on Signal Processing*, 58(10).

Errico, C., Pierre, J., Pezet, S., Desailly, Y., Lenkei, Z., Couture, O., and Tanter, M. (2015). Ultrafast ultrasound localization microscopy for deep super-resolution vascular imaging. *Nature*, 527(7579):499–502.

Fenster, A., Downey, D. B., and Cardinal, H. N. (2001). Three-dimensional ultrasound imaging. *Physics in Medicine and Biology*, 46(5):R67–R99.

Gateau, J., Chaigne, T., Katz, O., Gigan, S., and Bossy, E. (2013). Improving visibility in photoacoustic imaging using dynamic speckle illumination. *Optics letters*, 38(23):5188–5191.

Goodman, J. W. (2007). *Speckle phenomena in optics: theory and applications*. Roberts and Company Publishers.

Guo, Z., Li, L., and Wang, L. V. (2009). On the speckle-free nature of photoacoustic tomography. *Medical physics*, 36(9Part1):4084–4088.

Han, Y., Ding, L., Ben, X. L. D., Razansky, D., Prakash, J., and Ntziachristos, V. (2017). Three-dimensional optoacoustic reconstruction using fast sparse representation. *Optics letters*, 42(5):979–982.

Hansen, P. C. (1999). The l-curve and its use in the numerical treatment of inverse problems.

Harput, S., Christensen-Jeffries, K., Ramalli, A., Brown, J., Zhu, J., Zhang, G., Leow, C. H., Toulemonde, M., Boni, E., Tortoli, P., et al. (2019). 3-d super-resolution ultrasound (sr-us) imaging with a 2-d sparse array. *arXiv preprint arXiv:1902.01608*.

Hell, S. W. and Wichmann, J. (1994). Breaking the diffraction resolution limit by stimulated emission: stimulated-emission-depletion fluorescence microscopy. *Optics letters*, 19(11):780–782.

Helmchen, F. and Denk, W. (2005). Deep tissue two-photon microscopy. *Nature methods*, 2(12):932.

Hess, S. T., Girirajan, T. P., and Mason, M. D. (2006). Ultra-high resolution imaging by fluorescence photoactivation localization microscopy. *Biophysical journal*, 91(11):4258–4272.

Hingot, V., Errico, C., Heiles, B., Rahal, L., Tanter, M., and Couture, O. (2019). Microvascular flow dictates the compromise between spatial resolution and acquisition time in ultrasound localization microscopy. *Scientific reports*, 9(1):2456.

Hojman, E., Chaigne, T., Solomon, O., Gigan, S., Bossy, E., Eldar, Y. C., and Katz, O. (2017). Photoacoustic imaging beyond the acoustic diffraction-limit with dynamic speckle illumination and sparse joint support recovery. *Optics express*, 25(5):4875–4886.

Hoshi, Y. and Yamada, Y. (2016). Overview of diffuse optical tomography and its clinical applications. *Journal of biomedical optics*, 21(9):091312.

Huang, B., Xia, J., Maslov, K. I., and Wang, L. V. (2013). Improving limited-view photoacoustic tomography with an acoustic reflector. *Journal of biomedical optics*, 18(11):110505.

Huang, D., Swanson, E. A., Lin, C. P., Schuman, J. S., Stinson, W. G., Chang, W., Hee, M. R., Flotte, T., Gregory, K., Puliafito, C. A., et al. (1991). Optical coherence tomography. *science*, 254(5035):1178–1181.

Iskander-Rizk, S., Kruizinga, P., Springeling, G., Vos, H. J., van der Steen, A. F., and van Soest, G. (2017). Photoacoustic imaging of sub-diffraction objects with spectral contrast. *Optics letters*, 42(2):191–194.

Kruger, R. A., Kiser Jr, W. L., Reinecke, D. R., and Kruger, G. A. (2003). Thermoacoustic computed tomography using a conventional linear transducer array. *Medical physics*, 30(5):856–860.

Li, G., Xia, J., Wang, K., Maslov, K., Anastasio, M. A., and Wang, L. V. (2015). Tripling the detection view of high-frequency linear-array-based photoacoustic computed tomography by using two planar acoustic reflectors. *Quantitative imaging in medicine and surgery*, 5(1):57.

Lichtman, J. W. and Conchello, J.-A. (2005). Fluorescence microscopy. *Nature methods*, 2(12):910.

Liu, X., Peng, D., Guo, W., Ma, X., Yang, X., and Tian, J. (2012). Compressed sensing photoacoustic imaging based on fast alternating direction algorithm. *Journal of Biomedical Imaging*, 2012:12.

Luke, G. P., Hannah, A. S., and Emelianov, S. Y. (2016). Super-resolution ultrasound imaging in vivo with transient laser-activated nanodroplets. *Nano letters*, 16(4):2556–2559.

Mace, E., Montaldo, G., Osmanski, B.-F., Cohen, I., Fink, M., and Tanter, M. (2013). Functional ultrasound imaging of the brain: theory and basic principles. *IEEE transactions on ultrasonics, ferroelectrics, and frequency control*, 60(3):492–506.

Meng, J., Wang, L. V., Ying, L., Liang, D., and Song, L. (2012). Compressed-sensing photoacoustic computed tomography in vivo with partially known support. *Optics Express*, 20(15):16510–16523.

Morin, R., Basarab, A., and Kouamé, D. (2012). Alternating direction method of multipliers framework for super-resolution in ultrasound imaging. In *2012 9th IEEE International Symposium on Biomedical Imaging (ISBI)*, pages 1595–1598. IEEE.

Murray, T. W., Haltmeier, M., Berer, T., Leiss-Holzinger, E., and Burgholzer, P. (2017). Super-resolution photoacoustic microscopy using blind structured illumination. *Optica*, 4(1):17–22.

Ntziachristos, V. (2010). Going deeper than microscopy: the optical imaging frontier in biology. *Nature methods*, 7(8):603.

OReilly, M. A. and Hynynen, K. (2013). A super-resolution ultrasound method for brain vascular mapping. *Medical physics*, 40(11).

Pawley, J. (2010). *Handbook of biological confocal microscopy*. Springer Science & Business Media.

Provost, J. and Lesage, F. (2008). The application of compressed sensing for photoacoustic tomography. *IEEE transactions on medical imaging*, 28(4):585–594.

Rahman, M., Arshad, M., Manaf, A., and Yaacob, M. (2012). An investigation on the behaviour of pdms as a membrane material for underwater acoustic sensing.

Roumeliotis, M. B., Kosik, I., and Carson, J. J. (2012). 3d photoacoustic imaging using a staring-sparse array with 60 transducers. In *Photons Plus Ultrasound: Imaging and Sensing 2012*, volume 8223, page 82233F. International Society for Optics and Photonics.

Roumeliotis, M. B., Stodilka, R. Z., Anastasio, M. A., Ng, E., and Carson, J. J. (2011). Singular value decomposition analysis of a photoacoustic imaging system and 3d imaging at 0.7 fps. *Optics express*, 19(14):13405–13417.

Roux, E., Badescu, E., Petrusca, L., Varray, F., Ramalli, A., Cachard, C., Robini, M., Liebgott, H., and Tortoli, P. (2017a). Validation of optimal 2d sparse arrays in focused mode: Phantom experiments. In *2017 IEEE International Ultrasonics Symposium (IUS)*, pages 1–4. IEEE.

Roux, E., Varray, F., Petrusca, L., Mattesini, P., Cachard, C., Tortoli, P., and Liebgott, H. (2017b). 3d diverging waves with 2d sparse arrays: A feasibility study. In *2017 IEEE International Ultrasonics Symposium (IUS)*, pages 1–4. IEEE.

Rust, M. J., Bates, M., and Zhuang, X. (2006). Sub-diffraction-limit imaging by stochastic optical reconstruction microscopy (storm). *Nature methods*, 3(10):793.

Sehgal, C. M. and Greenleaf, J. F. (1984). Scattering of ultrasound by tissues. *Ultrasonic imaging*, 6(1):60–80.

Shu, W., Ai, M., Salcudean, T., Rohling, R., Abolmaesumi, P., and Tang, S. (2016). Broadening the detection view of 2d photoacoustic tomography using two linear array transducers. *Optics express*, 24(12):12755–12768.

Shu, Y., Han, C., Lv, M., and Liu, X. (2018). Fast super-resolution ultrasound imaging with compressed sensing reconstruction method and single plane wave transmission. *IEEE Access*, 6:39298–39306.

Siepmann, M., Schmitz, G., Bzyl, J., Palmowski, M., and Kiessling, F. (2011). Imaging tumor vascularity by tracing single microbubbles. In *2011 IEEE International Ultrasonics Symposium*, pages 1906–1909. IEEE.

Smith, S. W., Pavy, H. G., and von Ramm, O. T. (1991). High-speed ultrasound volumetric imaging system. i. transducer design and beam steering. *IEEE transactions on ultrasonics, ferroelectrics, and frequency control*, 38(2):100–108.

Tang, S. K. and Whitesides, G. M. (2010). Basic microfluidic and soft lithographic techniques. *Optofluidics: Fundamentals, Devices and Applications*, pages 7–32.

Turnbull, D. H. and Foster, F. S. (1991). Beam steering with pulsed two-dimensional transducer arrays. *IEEE transactions on ultrasonics, ferroelectrics, and frequency control*, 38(4):320–333.

van Sloun, R. J., Solomon, O., Bruce, M., Khaing, Z. Z., Wijkstra, H., Eldar, Y. C., and Mischi, M. (2018). Super-resolution ultrasound localization microscopy through deep learning. *arXiv preprint arXiv:1804.07661*.

Viessmann, O., Eckersley, R., Christensen-Jeffries, K., Tang, M., and Dunsby, C. (2013). Acoustic super-resolution with ultrasound and microbubbles. *Physics in medicine and biology*, 58(18):6447.

Vilov, S., Arnal, B., and Bossy, E. (2017). Overcoming the acoustic diffraction limit in photoacoustic imaging by localization of flowing absorbers. *arXiv preprint arXiv:1707.07358*.

Vu, T. (2016). Fista implementation in matlab. `https://github.com/tiepvupsu/FISTA`.

Wagner, R. F. (1983). Statistics of speckle in ultrasound b-scans. *IEEE Trans. Sonics & Ultrason.*, 30(3):156–163.

Wang, K., Su, R., Oraevsky, A. A., and Anastasio, M. A. (2012). Investigation of iterative image reconstruction in three-dimensional optoacoustic tomography. *Physics in Medicine & Biology*, 57(17):5399.

Wang, L., Li, G., Xia, J., and Wang, L. V. (2015). Ultrasonic-heating-encoded photoacoustic tomography with virtually augmented detection view. *Optica*, 2(4):307–312.

Wang, L. V. and Hu, S. (2012). Photoacoustic tomography: in vivo imaging from organelles to organs. *science*, 335(6075):1458–1462.

Wang, L. V. and Wu, H.-i. (2012). *Biomedical optics: principles and imaging*. John Wiley & Sons.

Xu, M. and Wang, L. V. (2005). Universal back-projection algorithm for photoacoustic computed tomography. *Physical Review E*, 71(1):016706.

Yang, D., Xing, D., Yang, S., and Xiang, L. (2007). Fast full-view photoacoustic imaging by combined scanning with a linear transducer array. *Optics express*, 15(23):15566–15575.

Yao, J. and Wang, L. V. (2013). Photoacoustic microscopy. *Laser & photonics reviews*, 7(5):758–778.

Zhang, P., Li, L., Lin, L., Shi, J., and Wang, L. V. (2019). In vivo superresolution photoacoustic computed tomography by localization of single dyed droplets. *Light: Science & Applications*, 8(1):36.

Zhao, N., Wei, Q., Basarab, A., Kouamé, D., and Tourneret, J.-Y. (2016). Single image super-resolution of medical ultrasound images using a fast algorithm. In *2016 IEEE 13th International Symposium on Biomedical Imaging (ISBI)*, pages 473–476. IEEE.

LIST OF PUBLICATIONS

1. Chaigne T, Arnal B, Vilov S, Bossy E, Katz O. Super-resolution photoacoustic imaging via flow-induced absorption fluctuations. Optica. 2017 Nov 20;4(11):1397-404.

2. Vilov S, Arnal B, Bossy E. Overcoming the acoustic diffraction limit in photoacoustic imaging by the localization of flowing absorbers. Optics letters. 2017 Nov 1;42(21):4379-82.

Appendices

Appendix A

Delay-and-sum beamforming

Here, we describe in detail the beamforming algorithm that we used to demonstrate the results of standard (diffraction-limited) photoacoustic (PA) reconstruction in this PhD study.

Fig. A.1 shows a typical radio-frequency (RF) frame that is available at the output of the acquisition machine as a result of a PA acquisition with a multielement array. Each cell of this frame contains the signal $S(t_i, k)$ which is equal to the quantized value of voltage on transducer element k registered at time t_i. The interval between successive time values t_i and t_{i+1} is equal to $\Delta t_s = 1/f_s$, where f_s is the sampling frequency of the acquisition machine.

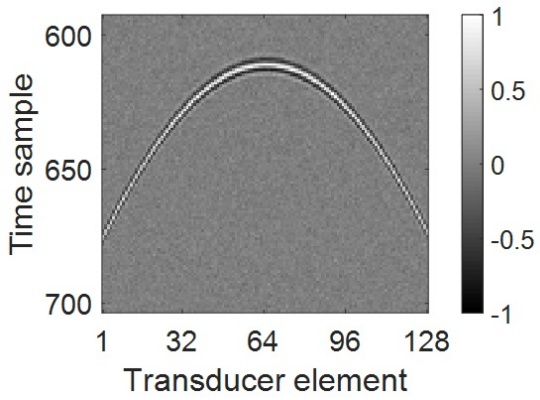

Fig. A.1 PA data in the form of an RF frame available at the output of the acquisition machine as a result of a PA acquisition with a multielement array consisting of $N_{el} = 128$ transducer elements.

In delay-and-sum beamforming each point of the reconstruction image $A(x, y, z)$ is obtained with the following equation:

$$A(x, y, z) = \sum_{k=1}^{N_{el}} S(t(k, x, y, z), k), \tag{A.1}$$

where N_{el} is the total number of transducer elements, $S(t(k, x, y, z), k)$ is the signal on element k at the time moment $t(k, x, y, z)$. The time moment $t(k, x, y, z)$ corresponds

to the arrival of the signal from the source placed at $\{x, y, z\}$ on element k.

Under the assumption that PA waves propagate in a homogeneous isotropic medium the arrival time $t(k, x, y, z)$ is given by

$$t(k, x, y, z) = \frac{1}{v_s}\sqrt{(x_k - x)^2 + (y_k - y)^2 + (z_k - z)^2}, \tag{A.2}$$

where v_s is the speed of sound in the medium, x_k, y_k and z_k are the coordinates of transducer element k.

From now on we will consider that RF data is obtained with a bandwidth-limited transducer with the central frequency f_c and the spectrum full width at half maximum (FWHM) Δf. In addition, we assume that $\Delta f \leqslant 2f_c$, which is true for the probes L7-4 and L22-8, used in this PhD study (see section 2.5).

As the time is discrete in the RF frame, $S(t(k, x, y, z), k)$ can not be obtained directly by taking a specific cell of the frame. However, its approximate value can be derived using the shift theorem:

$$S(t(k, x, y, z), k) \approx Re(S'(t_n, k) \cdot e^{2\pi j f_c (t(k,x,y,z) - t_n)}), \tag{A.3}$$

where $j = \sqrt{-1}$, $S'(t, k) = S(t, k) + jH(S(t, k))$ is the analytical signal with the real part corresponding to column k of the RF frame and the imaginary part corresponding to the Hilbert transform of this column. The "nearest" time sample t_n is chosen such that $t_n \leq t(k, x, y, z) < t_{n+1}$. In general, the narrower the transducer bandwidth Δf, the closer approximation (A.3) to the exact value of $S(t(k, x, y, z), k)$.

For a linear transducer array with the imaging plane XZ it is convenient to assume $y_k = 0$, $z_k = 0$ for all $k = 1..N_{el}$. It should also be noted that in imaging with a linear transducer array all out-of-plane sources lying withing the elevational focus ΔY will be projected on the reconstruction image XZ.

Fig. A.2 shows the point spread function (PSF) obtained via beamforming reconstruction for a single point source in the imaging plane XZ of a linear transducer array. This PSF is bipolar due to oscillations related to the finite transducer bandwidth.

As the axial oscillations of the PSF shown in Fig. A.2 are not related to the imaged object, they should be removed.

Let us consider a signal on one of the probe elements (i.e. one of the columns of the RF frame shown in Fig. A.1). Being bandwidth-limited, this signal can be represented as the product of the slow varying envelope $u(t)$ with the fast varying content $cos(2\pi f_c t)$:

$$S(t) = u(t)cos(2\pi f_c t). \tag{A.4}$$

According to the Bedrosian theorem, as $u(t)$ has no frequency content above the carrier

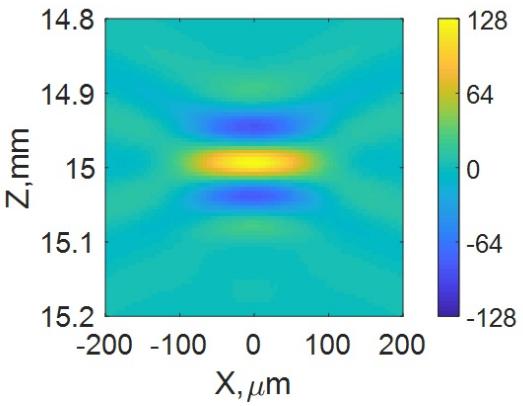

Fig. A.2 Bipolar PSF obtained by beamforming RF data that corresponds to a single source in the imaging plane XZ.

frequency f_c (since $\Delta f \leqslant 2f_c$), Hilbert transform of (A.4) is given by

$$H(S(t)) = u(t)sin(2\pi f_c t). \tag{A.5}$$

The oscillations at carrier frequency f_c can be eliminated by taking the envelope of the complex analytical signal $S'(t) = S(t) + jH(S(t))$:

$$|S'(t)| = \sqrt{[S(t)]^2 + [H(S(t))]^2} = u(t). \tag{A.6}$$

Thus, to remove the axial PSF oscillations, the envelope image should be formed. To do it, two RF frames should be independently beamformed. The first RF frame will be provided directly by the acquisition machine, while the second frame is obtained by applying columnwise Hilbert transform to the first one. Then, the envelope image is computed as the absolute value of the ”analytical image” formed by the first (real part) and the second (imaginary part) beamformed images. The operation is illustrated in Fig. A.3.

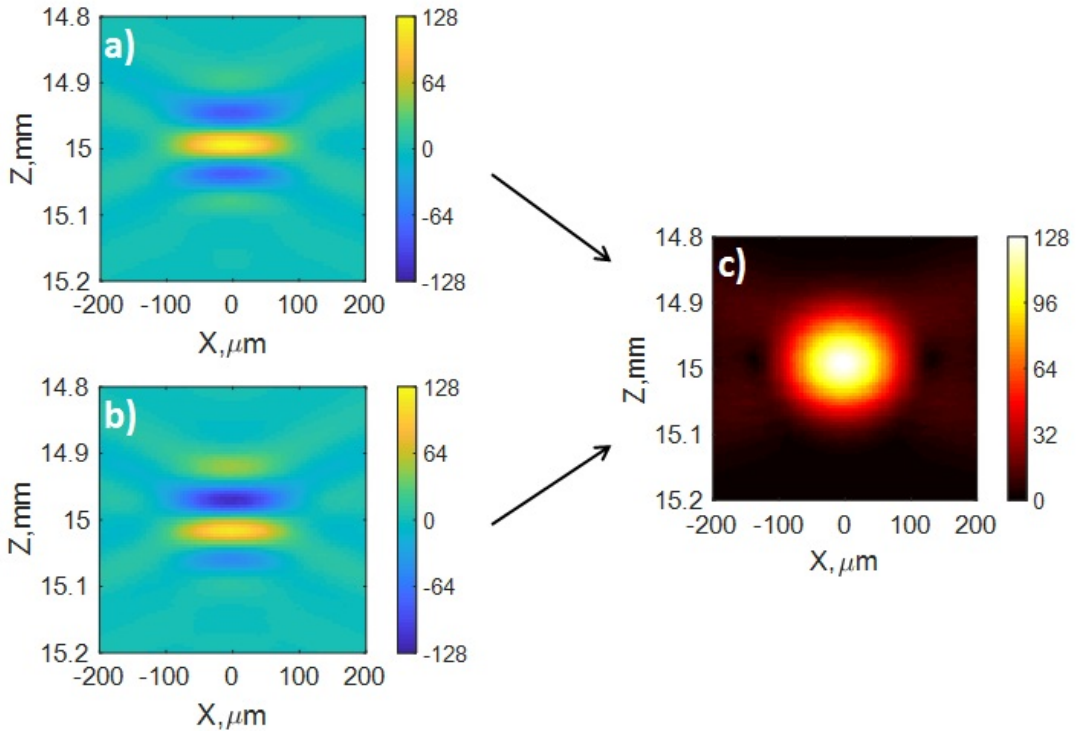

Fig. A.3 (a) Bipolar PSF, same as in Fig. A.2. (b) PSF resulting from beamforming of the RF frame obtained by applying columnwise Hilbert transform to the RF frame. (c) Envelope PSF image computed as the absolute value of the ”analytical image” formed by the beamformed images shown in (a) and (b).

Appendix B

Remarks on the numerical norm-based reconstruction

As mentioned in Chapters 5-7, to perform iterative minimization (for L1-based and positivity-based reconstruction), the FISTA algorithm [Beck and Teboulle, 2009; Vu, 2016] was used. Here, we list some technical modifications that were applied to improve the performance of the initial FISTA code [Vu, 2016].

1) Transformation of the matrix $\boldsymbol{A}_{RF}$.

In reconstruction based on radio frequency (RF) data, the matrix $\boldsymbol{A}_{RF}$ needs to be passed to the FISTA algorithm. Each column of this matrix contains the vector form of the system's response at a particular point of the reconstruction zone or the RF point spread function (RF PSF). This vector is a rearranged RF data frame, whose dimensions are $M = M_t \times M_e$, where M_t is the number of time samples and M_e is the number of transducer elements. For a typical RF frame, shown in Fig. B.1a, the number M reaches 12800. A typical reconstruction zone consists of several hundred points. As the number of reconstruction points is equal to the number of columns of the matrix $\boldsymbol{A}_{RF}$ and the size M of the RF frame is equal to the number of rows, a typical matrix $\boldsymbol{A}_{RF}$ will contain several million elements. To reduce the size of the matrix $\boldsymbol{A}_{RF}$ and the eventual computational time, we apply fixed time delays to each column of the RF frame. These time delays are computed to flatten the curve corresponding to the photoacoustic (PA) signal. Thus, the new RF frame will contain much fewer elements. As all columns of the matrix $\boldsymbol{A}_{RF}$ must have the same length, all the transformed RF frames must have the same size. It should also be emphasized, that the same time delays are applied to all RF frames. So, the size of each RF frame should be chosen so that a PA signal originating from any point of the imaging zone will be confined within the RF frame. Finally, to preserve the relation between the measurement vector R and the propagation matrix $\boldsymbol{A}_{RF}$ the same transformation should be applied to the imaging RF data.

For the frame shown in Fig. B.1 the proposed transformation results in the frame shown in Fig. B.1b. As can be seen, the applied transformation almost halved the initial number of entries ($M = 12800$ for the initial RF frame, $M = 5180$ for the final RF frame).

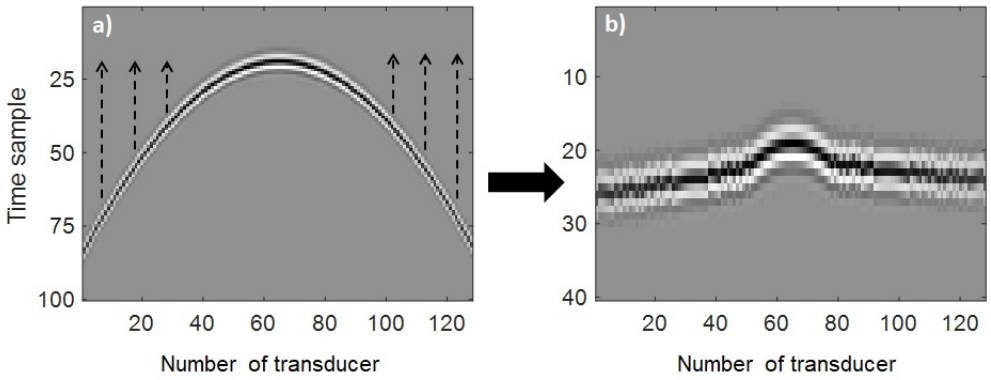

Fig. B.1 RF frame size reduction. (a) initial RF frame, comprising $M = 12800$ elements, (b) RF frame after transformation, comprising $M = 5180$ elements.

2) Derivation of the matrix $\boldsymbol{A}_{BF}$.

The matrix $\boldsymbol{A}_{BF}$ is derived from the matrix $\boldsymbol{A}_{RF}$ by unwrapping each column onto the RF space, beamforming and then rearranging the obtained beamforming point spread functions (BF PSFs) into the columns of the matrix $\boldsymbol{A}_{BF}$. However, the beamforming operation spreads out the signal confined in the limited RF space onto the *unlimited* beamforming space. In order to avoid a large part of the signal being lost, the beamforming zone must be chosen larger than the reconstruction zone. To preserve most of the relevant signal in the beamforming operation, we left margins of about 1/2 of the full width at half maximum (FWHM) of the BF PSF between the border of the reconstruction zone and the border of the beamforming zone (see Fig. B.2).

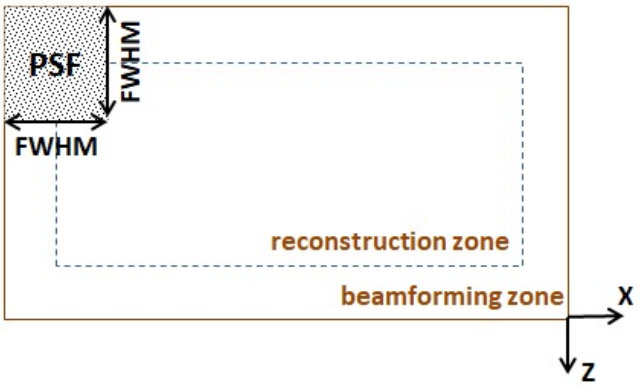

Fig. B.2 Choice of the beamformig zone: the beamforming zone should be chosen larger than the reconstruction zone. We propose to leave margins of about 1/2 of the full width at half maximum (FWHM) of the beamforming PSF in order to properly take into account the points at the border of the reconstruction zone .

3) Elimination of irrelevant points.

As in most cases we performed reconstruction of sparse objects, many points on the

reconstruction grid were filled with zeros already after first few iterations of the algorithm. Thus, it was unnecessary to keep information about all these points during the entire reconstruction process. So, to speed up the calculations, every 1000 iterations of the algorithm the pixels $T(i)$ below 0.1% of the mean signal level $mean(|T|) = 1/N \sum_{i=1}^{N} |T(i)|$ were detected: $T(i) < 10^{-3} \times mean(|T|)$. Then, the corresponding columns were extracted from the propagation matrix A and the minimization algorithm was relaunched with the reduced propagation matrix. The removed pixels were permanently filled with zeros in the final reconstruction image.

4) Choice of the stopping criterion.

The stopping criterion was chosen based on the object sparsity K (number of reconstructed point sources)that was estimated for the object T as $K \approx ||T||_1/mean(T)$. The minimization algorithm was forced to stop when the estimation of K changed by less than 0.01% in the last 1000 iterations.

Appendix C

Singular value decomposition filtering

Here, we describe the singular value decomposition (SVD) filtering that we used to separate relevant fluctuations from noise in imaging based on fluctuations of photoacoustic (PA) signals. In such imaging, reconstruction is done by calculating a certain statistical property related to relevant fluctuations. This can be simple variance (see Chapter 7) or high order cumulants (see Chapter 4). As PA data always contains some noise, statistical quantities of this noise may be as strong as those of relevant PA signals. So, separating signal fluctuations from noise fluctuations is important before performing fluctuation-based reconstruction.

The idea of SVD filtering is to separate fluctuations with different spatiotemporal behaviour. In ultrasound (US) imaging, it was first proposed to use this technique to discriminate tissue and blood motion [Demené et al., 2015]. Realization of SVD filtering in photoacoustics is close to SVD filtering in US and we will base our explanation on the analysis from [Demené et al., 2015]. SVD filtering can be applied to raw radio-frequency (RF) or beamformed (BF) data. In our experiments, we always applied SVD to BF data.

Let us consider the initial set composed by N_t two-dimensional BF images, each consisting of $N_z \times N_x$ pixels. This set can be rearranged to form a two-dimensional matrix $\boldsymbol{S}^{N_s \times N_t}$, where $N_s = N_z \times N_x$. The SVD of the matrix $\boldsymbol{S}$ can be expressed as

$$\boldsymbol{S} = \boldsymbol{U}\boldsymbol{\Sigma}\boldsymbol{V}^*, \tag{C.1}$$

where $\boldsymbol{V}^{N_t \times N_t}$ and $\boldsymbol{U}^{N_s \times N_s}$ are unitary matrices, * designates conjugate transpose. The matrix Σ is diagonal, its diagonal values σ_i are called the singular values of the matrix $\boldsymbol{A}$ and are conventionally arranged in the descending order: $\sigma_1 > \sigma_2 > ... > \sigma_{N_l}$, where $N_l = min(N_s, N_t)$. So, the matrix $\boldsymbol{S}$ can also be expressed as [Demené et al., 2015]:

$$\boldsymbol{S} = \sum_i \sigma_i \boldsymbol{A}_i, \tag{C.2}$$

where the matrix $\boldsymbol{A}_i$ is the outer product $\boldsymbol{U}_i \oplus \boldsymbol{V}_i$ with $\boldsymbol{U}_i$ and $\boldsymbol{V}_i$ being the i^{th} columns of the corresponding SVD (C.1).

One can notice that SVD decomposes the initial matrix $\boldsymbol{S}$ in a sum of separable images, characterized by the vector $\boldsymbol{U}_i$, that are modulated in time by the temporal signal $\boldsymbol{V}_i$. The singular values σ_i indicate the weight of each pattern $\boldsymbol{U}_i$ in the set of PA images: large singular values are associated with static or quasi-static features, such as tissue motion, whereas low singular values are associated with unstable features, such as noise fluctuations which vary from one image to another. SVD filtering generates a new series of images $\boldsymbol{S}'$ by selecting relevant singular vectors $i = a..b$, i.e. those that are associated with PA signal fluctuations:

$$\boldsymbol{S}' = \sum_{i=a}^{b} \sigma_i \boldsymbol{A}_i, \tag{C.3}$$

where the matrix $\boldsymbol{A}_i$ corresponds to SVD (C.1).

A major difficulty of SVD filtering is to choose the set of singular values $i = a..b$ that corresponds to the imaged structure. In this regard, different methods were proposed and compared in [Baranger et al., 2018]. The simplest approach consists in selecting relevant singular vectors based on a visual inspection of the objects reconstructed with different sets of singular vectors. A better choice could be made by computing the so-called spatial similarity matrix which is based on correlation between magnitudes of spatial vectors $|\boldsymbol{U}_i|$.In this matrix, regions with high correlation between neighbouring vectors will correspond to fluctuations of the same spatial distribution. By detecting the region corresponding to relevant fluctuations, right singular values are selected. For the details, the reader is referred to [Baranger et al., 2018]. We used the spatial similarity matrix to choose the optimal set of singular values in the actual study.